Deformability in Soft Matter and Biological Physics

Ioannis Hadjifrangiskou
Balliol College
University of Oxford

This dissertation is submitted for the degree of
Doctor of Philosophy in Theoretical Physics

Trinity Term 2025

Acknowledgements

First, I would like to thank my supervisor, Prof. Julia M. Yeomans, for providing me with guidance and support throughout my DPhil. It is not an exaggeration to say that you have taught me everything I know about mathematical modelling. Thank you for giving me the freedom to explore and develop my research interests. Finally, thank you for unrelentingly teaching me to always keep in mind the bigger picture. Thanks to you I have learned to try and understand things beyond what equations show, and to always try and find the story.

I would also like to thank all the people in the Physics Department who have shared this journey with me. This includes the Yeomans group and my office mates over the years, in particular Liam Ruske, Saraswat Bhattacharyya, Jan Rozman, Gianmarco Spera, Diogo Pinto, Rahil Valani, Francesco Mori, James Graham, Mehrana Nejad, Samantha Lish, Muriel van der Laan, Sam von der Dunk, Guanming Zhang, and many more. I really enjoyed our lunch breaks, board games, and dinner outings! Special thanks to Prof. Sumesh Thampi for his tremendous help along the way, and Diogo and Gianmarco for our - almost - daily coffee outings!

Finally, I would like to thank my family for all the love and support they have given me throughout my academic career but also my life more broadly. In particular, I would like to thank my grandmother, Katerina Hadjifrangiskou, my aunt Eleni Mina, my father Pantelis Hadjifrangiskou and my mother Anna Christou for always being there for me, and for the sacrifices they made to enable and encourage me throughout my journey.

Publications

Authored publications contributing to this thesis

- Hadjifrangiskou, I., Ruske, L. J. & Yeomans, J. M. Active nematics with deformable particles. *Soft Matter* **19,** 6664–6670 (2023)
- Hadjifrangiskou, I., Thampi, S. P. & Valani, R. N. Nematic order from phase synchronization of shape oscillations. *Phys. Rev. Lett.* **135,** 068101 (Sept. 2025)
- Hadjifrangiskou, I., Thampi, S. P. & Yeomans, J. M. Channel Flows of Deformable Nematics. *Phys. Rev. Lett.* **135,** 118202 (11 Sept. 2025)

Contents

Appendices

1

Introduction

The ability of soft particles to modulate their shape has been a field of considerable interest recently, creating a link between soft matter and biological physics [4]. Both simulations and experiments have shown that large shape variations are ubiquitous in artificial soft matter systems such as colloids and vesicles [5–7] and biological matter such as Madin-Darby canine kidney (MDCK) cells [8, 9], embryonic tissue [10–14] and cells in vasculature [15, 16]. The main objective of this thesis is to create a minimal framework where deformability is introduced in a phenomenological way into the current mathematical models that are used to study the collective dynamics of systems that show large shape variations. We will study the coupling of the shape variations of particles to their motion and orientational dynamics and explore how it affects the observed dynamics both qualitatively and quantitively, creating an experimentally verifiable framework for the study of systems of deformable particles.

We will consider two main classes of systems: (i) passive, driven systems where there is an external injection of energy such as applying an external shear or pressure gradients, leading to forcing that drives particle motion and deformations and (ii) active matter systems, which use chemical energy from their surroundings to generate forces at a local level. In the latter case, such as in cell monolayers, individual cells are able to move by pushing or pulling on their surroundings or by changing their shape [17, 18]. Indeed, numerous theoretical frameworks have been proposed to investigate the mechanical behavior of cell layers, spanning a wide range of complexity and resolution [19].

Among these, the continuum theory of active nematics has emerged as a particularly influential approach [20], attracting significant attention as a promising theoretical model for collective dynamics. Active nematic theory describes systems of rigid, anisotropic particles which apply local forces on their environment [20, 21] in a coarse-grained, continuum limit. Active nematic theories have been successful in modelling several qualitative phenomena such as active turbulence in biological systems [22], spontaneous cellular flow in confined spaces [23], and the role of topological defects in growing bacterial biofilms [24] and regenerative hydra [25]. We will introduce the theory of what we will refer to as rigid active nematics in Chapter 2.

In this thesis, we firstly extend the hydrodynamic theory of traditional nematics by incorporating deformability of the constituent particles using a minimal model. We consider passive, driven systems (Chapter 3) as well as active systems (Chapter 4). Secondly, we show how particle deformability provides a different, and rarely explored avenue of nematic order in *dilute* systems, far from the continuum limit. We show that oscillatory external driving, due to activity or otherwise, may create global nematic order in a system of deformable nematic particles depending on the parameters of the external driving.

This thesis is structured as follows: In Chapter 2, we introduce the continuum equations of nemato-hydrodynamics. These equations describe the dynamics of the orientation field, the degree of nematic order and the flow field, and how changes in the orientation field and flow field are coupled to each other. We then extend this by considering how activity may be incorporated into the continuum equations. Active nemato-hydrodynamics will serve as our model for biological tissue and provide the theoretical framework underpinning the results outlined in the rest of the thesis. The details about how these equations are solved numerically are presented in Appendix A.

In Chapter 3, we highlight the need for a model of deformable nematics. We then develop a model where particle shape is approximated as elliptical, and characterised by a single scalar, the aspect ratio. We derive the resulting time evolution equation for the aspect ratio and couple it to both the orientation and flow dynamics. Finally, we apply the extended model in simple channel flows. We find that the coupling of the shape to orientation creates novel dynamics that cannot be captured by continuum models of rigid particles.

In Chapter 4, we look at an active nemato-hydrodynamic model of deformable nematics in a bulk system. While elongated, rigid active nematics in bulk develop active turbulent flows due to a coupling of active forcing and flow-aligning effects [26, 27], we find that in our model, a finite activity is required to maintain the elongation of particles, and serves as a prerequisite to the creation of nematic order due to flow-aligning effects. Furthermore, both qualitative and quantitative differences are seen between the active turbulent states of rigid and deformable active nematics. The latter shows a co-existence of regions of elongated particles which create chaotic flows, with regions of quiescent, circular particles. Measurable quantities, such as the average elongation of particles across the system and the correlation lengths are also studied.

In Chapter 5, we turn our attention to dilute systems of nematic particles in a channel under external driving. We begin by providing a brief mathematical introduction into the literature of phase synchronisation. We then show through both analytics and numerical simulations that an oscillatory perturbation to the driving will induce global nematic order in the case of deformable particles, but will *not* do so for rigid particles. We find that this is linked to the non-linear coupling between shape and orientational dynamics and study the consequences from a dynamical systems perspective.

2

Hydrodynamic theory of passive and active nematics

In this chapter, we present the theoretical foundations for describing nematic liquid crystals, with a focus on applications to soft and biological matter. We begin by introducing the nematic orientation order parameter and constructing the associated static free energy. This framework is then extended to active nemato-hydrodynamics - a continuum model that captures the emergent, large-scale dynamics of confluent cell layers. The resulting equations govern both the evolution of the orientational order parameter and the flow field, along with their mutual coupling. These equations form the core of our modelling approach for active systems such as biological tissues and will serve as the starting point for the extensions developed in subsequent chapters.

2.1 Introduction

Living systems are inherently active as they use chemical energy from their surroundings to do work. Examples include molecular motors such as kinesin or myosin which hydrolyse ATP (adenosine triphosphate) to drive conformational changes in the motor proteins [19] and living bacteria such as E. coli which metabolise nutrients to power the rotation of their flagella [28]. Non-living systems may also be active. A common example is synthetic Janus particles, colloids which have a catalytic (*e.g.* platinum) coating in a hydrogen peroxide solution which decomposes the fuel, driving ionic gradients and resulting in directed motion [29]. Motile cells in confluent layers convert chemical energy into mechanical forces that act upon their surroundings, such as the substrate and neighbouring cells [30]. These layers can exhibit a wide array of collective behaviours, including glassy dynamics [8, 31], flocking-like coherence [32], and turbulence-like chaos [20, 33, 34].

It is becoming increasingly clear that many features seen in cell layers and tissues can be understood using continuum approaches that describe length scales spanning several cells. These approaches are based on a coarse grained description of the constituent particles. While tissues are composed of discrete cells, their collective behaviour may be described by coarse grained fields [35]. Additionally, cell-cell junctions, adhesion, and other biological mechaninisms contribute to the overall stress in the system. As such, particle shape and flow evolution depends on force balance. Examples include biofilm initiation, topological defects in cell monolayers and epithelial expansion [36–44]. Among these, the continuum theory of active nematics, which describes hydrodynamic interactions between active anisotropic particles has been successful in predicting many qualitative features such as short-range orientational order, active turbulence and motile topological defects [45–48] as well as quantitative features such as the lengthscale associated with vortex sizes, defect spacing [49] and flow correlations [50].

These systems are described by a tensorial order parameter which captures the magnitude and direction of alignment of the active particles and a velocity field for collective motion. Activity is incorporated in the continuum equations through active stresses that emerge from the microscopic level. Together, these constitute the ingredients of the theory of active nematics [20, 26], which forms a well-established model to study large-scale, collective behaviours. Such a continuum approach offers computational tractability and deep analytical insight into the underlying physics.

This chapter proceeds as follows: In Sec. 2.2, we discuss the orientation field and the construction of the $\mathbf{Q}$ tensor, along with the Landau-de Gennes free energy and the topological defects that result from it. Following this, in Sec. 2.3 we discuss the velocity field and the governing conservation laws. In Sec. 2.4, we couple these fields via the equations of nemato-hydrodynamics. Sec. 2.5 introduces activity into the model and explores its consequences, such as instabilities and turbulence. Sec. 2.6 outlines numerical techniques used to solve the model equations. Finally, in Sec. 2.7 we provide a summary of the chapter.

In three dimensions, conventional thermotropic nematics display true long-range orientational order, meaning that the orientational correlation function approaches a non-zero constant at large separations

2.2 The orientational order parameter

Nematic liquid crystals, composed of elongated particles with head-tail symmetry, display liquid-like positional disorder but exhibit long-range orientational order at high concentrations or low temperatures in three dimensions. This means that the orientational correlation function approaches a non-zero constant at large separations. This happens due to thermodynamic interactions that cause the materials to align along their axes of elongation [51, 52]. However, in two dimensions, the Mermin-Wagner theorem forbids true long-range order [53] and nematic phases in 2D have been found to exhibit only quasi–long-range order, where orientational correlations decay algebraically rather than saturating [54]. To describe such systems in the continuum, we adopt the Q-tensor formalism, which is a coarse-grained description of the orientational order parameter of nematic liquid crystals.

2.2.1 The Q tensor

The director field $\mathbf{n}(\mathbf{r})$, describes the average direction of the long axes of particles in a small volume element about the point $\mathbf{r}$. Given nematic symmetry ($\mathbf{n} \to -\mathbf{n}$), the director field is headless, as shown in Fig. 2.1.

To quantify alignment in 2D, we examine the orientation distribution, $f(\theta)$, where θ is the angle between the particle orientation and the director. That is, the probability distribution of finding a particle with an orientation in the interval $[\theta, \theta + d\theta]$ is given by $f(\theta)d\theta$. To calculate this, we will sum along all

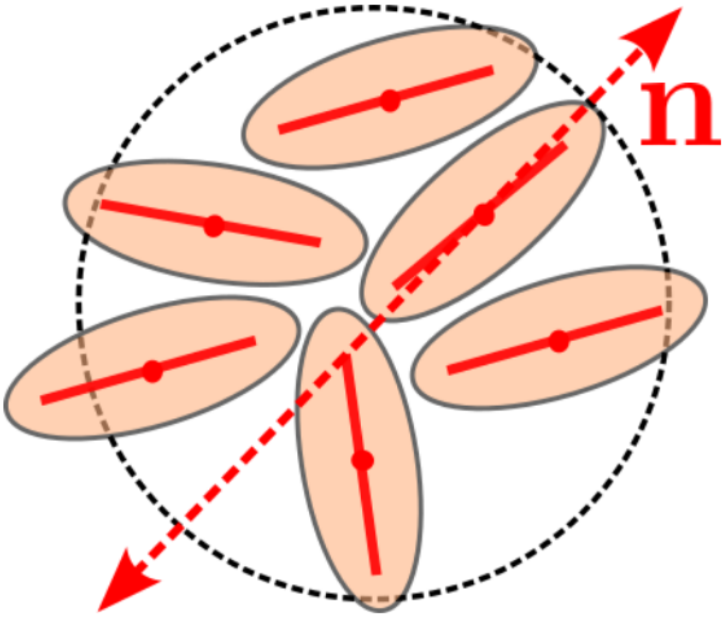

Figure 2.1: Director field **n**, calculated as the average direction of the long axes of constituent head-tail symmetric particles. The operation $\mathbf{n} \to -\mathbf{n}$ keeps the system unchanged.

possible directions, so we may assume, without loss of generality, that $\mathbf{n} = \hat{x}$ so that θ is the usual polar angle.

For N particles with orientations θ_k, the nematic order magnitude, S is given by

$$S = \langle \cos 2\theta_k \rangle = \frac{1}{N} \sum_{k=1}^{N} \cos 2\theta_k. \tag{2.1}$$

In the continuum limit, this becomes

$$S = \int_0^{2\pi} f(\theta) \cos 2\theta d\theta \,. \tag{2.2}$$

For a distribution with head-tail symmetry, which implies $f(\theta) = f(\theta + \pi)$, this expression is equivalent to the first non-trivial term in the Fourier decomposition of $f(\theta)$:

$$f(\theta) = \frac{1}{2\pi} \left[1 + \sum_{m=1}^{\infty} \left(a_m \cos m\theta + b_m \sin m\theta \right) \right]. \tag{2.3}$$

Imposing the nematic symmetry constraint on the Fourier series, and noting that $\cos m(\theta + \pi) = (-1)^m \cos m\theta$ and similarly for $\sin m(\theta + \pi)$, we see that all a_m, b_m for odd m must vanish. In particular, this implies that the first mode ($m = 1$), which corresponds to polar order, must be zero. We then note that S is the first non-trivial term in the multipole expansion of $f(\theta)$. For perfect alignment, $f(\theta) = \delta(\theta) \Rightarrow S = 1$; for random, uniform alignment, $f(\theta) = 1/2\pi \Rightarrow S = 0$. This calculation is specific to two dimensions, however the order parameter may be defined in a similar fashion for three-dimensional, uniaxial nematics where the orientational distribution function depends only on the polar angle.

Typically the concentration of the nematogens can control whether nematic alignment is preferable [51]. At low concentrations, an isotropic configuration with no nematic alignment is preferred primarily due to entropic reasons ($S = 0$). However, at higher concentrations, the thermodynamically preferable configuration has orientational alignment, but particles are free to move about in space ($S \neq 0$) [52]. It is also possible to transition from the nematic configuration ($S \neq 0$) to the isotropic configuration ($S = 0$) by increasing the temperature past a critical temperature, called the nematic-isotropic transition temperature T_N.

The nematic tensor $\mathbf{Q}$ for a uniaxial nematic, in d dimensions is then defined as [51]

$$\mathbf{Q} = \frac{d}{d-1} S \left(\mathbf{n} \otimes \mathbf{n} - \frac{\mathbb{I}}{d} \right). \tag{2.4}$$

This quantity contains all the information about the nematic order. The Kronecker product $\mathbf{n} \otimes \mathbf{n}$ ensures head-tail symmetry, S captures the magnitude of nematic order, and the term proportional to the identity is subtracted to keep $\mathbf{Q}$ traceless. The latter is to ensure that the tensor only encodes anisotropic directional ordering [51, 55]. The choice of the dimension-dependent normalisation is so that S is exactly the eigenvalue associated with the director field and is not to be confused in the literature where it is sometimes omitted. It will be convenient to write our equations in terms of $\mathbf{Q}$ instead of $\mathbf{n}$, since $\mathbf{Q}$ explicitly preserves nematic symmetry since it is even in the powers of $\mathbf{n}$.

In this thesis, we will only deal with two-dimensional systems ($d = 2$), however, at times, the equations and simulation protocols used will be in $d = 3$ as that is how the numerical code that is being used has been structured. The systems considered will be such that one of the three dimensions is constrained, resulting in a $2D$ representation.

2.2.2 Landau de-Gennes free energy

The ground state of the system is modelled by a free energy functional with two terms - a bulk term that describes local nematic ordering, and an elastic term to ensure long-range order in the orientational field. We write these contributions in terms of $\mathbf{Q}$ in the following subsections.

Bulk free energy

The free energy density in the order parameter $\mathbf{Q}$ can be expanded as [51]

$$f_{bulk} = \frac{\mathcal{A}}{2}\,\mathrm{Tr}(\mathbf{Q}^2) + \frac{\mathcal{B}}{3}\,\mathrm{Tr}(\mathbf{Q}^3) + \frac{\mathcal{C}}{4}\,\mathrm{Tr}(\mathbf{Q}^2)^2 \ + \dots\ , \tag{2.5}$$

where $\mathcal{A}, \mathcal{B}$ and $\mathcal{C}$ are arbitrary coefficients which define the energy landscape in $\mathbf{Q}$ space. In 2D systems, the cubic term $\propto \mathrm{Tr}(\mathbf{Q}^3)$ vanishes [56] since the eigenvalues of $\mathbf{Q}$ are equal and opposite. This can be seen directly by noting that the $\mathrm{Tr}(\mathbf{Q}^3) = \lambda_1^3 + \lambda_2^3$, where λ_1, λ_2 are the eigenvalues of $\mathbf{Q}$, which obey $\lambda_2 = -\lambda_1$ since $\mathbf{Q}$ is traceless.

Hence, in 2D, the nematic-isotropic transition depends on the ratio $\mathcal{A}/\mathcal{C}$. In particular, we require that $\mathcal{A} < 0$ and $\mathcal{C} > 0$ for a non-zero equilibrium value of S. Physically, we understand this as negative $\mathcal{A}$ promotes order $S > 0$ and positive $\mathcal{C}$ keeps the value of the order in check. If both coefficients are positive, only disorder ($S = 0$) is promoted. It is then common for $\mathcal{A}$ to explicitly depend on temperature, *e.g.* $\mathcal{A} \propto (T - T_N)$, so that it switches sign as the temperature crosses the nematic-isotropic transition temperature, T_N. Lastly, we note that in 2D, the transition is of second order, as the stable equilibrium point for S varies continuously from 0 to a positive finite number as the transition temperature is crossed from above. In 3D, the cubic term in the free energy introduces extra complexity, allowing the transition to be first order.

In the case we consider in this thesis, the nematic bulk free energy may be simplified further, and can be re-written as

$$f_{bulk} = A_Q \left(S_{eq}^2 - \frac{2\mathrm{Tr}(\mathbf{Q}^2)}{3} \right)^2 . \tag{2.6}$$

When $A_Q > 0$ in Eq. (2.6), this describes a nematic with a magnitude of nematic order S_{eq} inside the bulk, the equilibrium value of S which minimises the free energy. We will use the form given by Eq. (2.6) for the rest of the thesis. It is also worth noting that thermodynamic effects captured by a bulk free energy are not the only way to drive local nematic order. Effects such as fluctuating traction forces [57] and flow-driven effects in active and passive systems [27] have also been showing to be drivers of nematic order.

Elastic free energy

In two dimensions, a nematic field can have two different types of distortions - bend and splay, with elastic constants K_1, and K_2 respectively. This gives the Frank free energy [58]

$$f_{Frank} = \frac{K_1}{2}[\nabla \cdot \mathbf{n}]^2 + \frac{K_2}{2}[\mathbf{n} \times (\nabla \times \mathbf{n})]^2 , \tag{2.7}$$

where $n(x, y, 0) = (\cos\theta, \sin\theta, 0)$ as it is understood that the curl is taken by assuming a third spatial dimension exists, while the system is constrained to lie on the 2D plane. This free energy term penalises distortions in the nematic field.

In this thesis, we will work under the assumption of a single elastic constant $K_1 = K_2$, which has been used to accurately describe many biological systems [20, 24, 59]. For a director field n_i The elastic free energy of a nematic can then be written as

$$f_{elastic} = \frac{K}{2}\partial_i n_j \partial_i n_j , \tag{2.8}$$

where K is the elastic constant in this approximation. Extending this to the $\mathbf{Q}$-tensor formulation of the free energy, by noting that $(\nabla\mathbf{Q})^2) = 2S^2\left(\nabla\mathbf{n}\right)^2$ for constant S, this can be written as

$$f_{elastic} = \frac{K_Q}{2}\partial_k Q_{ij} \partial_k Q_{ij}, \tag{2.9}$$

where K_Q is the elastic constant.

Defects in the director field

The elastic free energy tends to smooth out variations in the director field and typically prevents discontinuities. However, defects may arise at points where orientations differ drastically across domains. These defects are places of singularities or discontinuities in the director field that require large distortions, and hence elastic energy and stresses. They have been and classified in detail using homotopy theory [60, 61]. In this thesis, we focus on their geometry, and their effects on the dynamics of the systems we study. Mathematically, these defects are the solutions of the director field that minimise the Frank free energy shown in Eq. (2.7). Defects are usually referred to by their winding number which is defined as the contour integral of the director field around the defect,

$$m = \frac{1}{2\pi} \oint d\theta \, . \tag{2.10}$$

More intuitively, if we imagine the director as a proper vector field, the winding number gives us the number of times it will wind around a loop encircling the defect in a counter-clockwise sense. After going around this closed contour loop, the single-valuedness of the angle θ requires that we return to the starting angle. Further, due to the nematic symmetry $\mathbf{n} \to -\mathbf{n}$, the director is invariant after rotation by an integer multiple of π i.e. $\theta \to \theta + n\pi$, where n is any integer. Therefore, the winding number is allowed to only acquire half-integer values $m = n/2$. For two dimensional defects, the winding number is a topological invariant and is also commonly referred to as a topological “charge”. Hence, the total topological charge of a closed system is a conserved quantity determined by its geometry alone. Defects may necessarily exist in a system due to the boundary conditions imposed. For example, a parallel anchoring boundary condition for the director field along the edges of a system requires a total of $+1$ topological charge within the system, which in turn enforces the existence of defects to satisfy this topological constraint.

While in principle all defects with winding numbers $m = n/2$ are allowed, the elastic free energy for a defect of winding number m scales as $f_{defect} \propto m^2$ [62]. Thus, defects with charges other than $\pm 1/2$ are energetically unfavourable in general and break apart into two or more $\pm 1/2$ defects, preserving charge conservation. Within sufficiently confined systems, this need not be the case, as there is an additional free energy cost due to the core of the defect that does not scale with winding number. Additionally, differently charged defects may be also be created depending on boundary conditions. However in this thesis we do not concern ourselves with these possibilities. Due to the conservation of topological charge, $\pm 1/2$ defects are created and annihilated in pairs.

The $+1/2$ defect is created when the director rotates *counter-clockwise* by an angle of π when travelling along the contour counter-clockwise. It has a characteristic comet shape, as shown in Fig. 2.2 (a). Conversely, a $-1/2$ defect is observed when the director rotates *clockwise* when travelling along the contour counter-clockwise. It has a characteristic three-fold symmetry, as shown in Fig. 2.2 (b). In this thesis, we will deal exclusively with comet-shaped $+1/2$ and trefoil-shaped $-1/2$ defects in two dimensions.

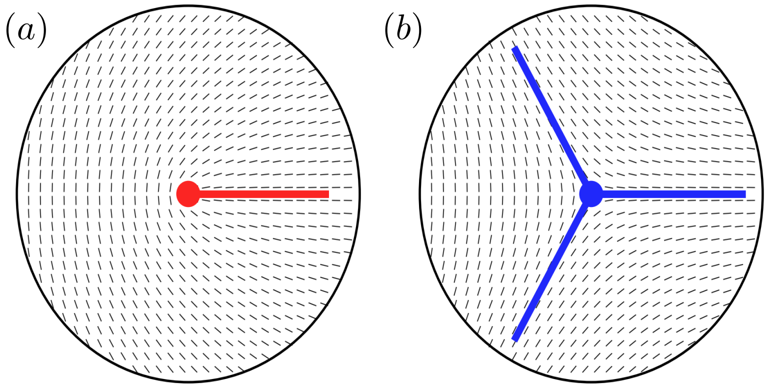

Figure 2.2: Director fields of defects with winding numbers $\pm 1/2$. (a) Director field around a $+1/2$ defect, which has a comet-like structure with a head (marked by the red dot) and a tail (marked by the red line). (b) Director field around a $-1/2$ defect, which has a three-fold symmetry (marked by the blue lines).

2.3 The velocity field

The velocity field $\mathbf{u}(\mathbf{r})$ represents the collective motion of the nematic fluid at position $\mathbf{r}$. We assume that the fluid is incompressible and has uniform density. Under these assumptions, conservation of mass imposes the condition that the velocity field must be divergence-free:

$$\nabla \cdot \mathbf{u} = 0 \, . \tag{2.11}$$

In addition, the system must satisfy local force balance, which leads to the momentum conservation equation:

$$\rho \left(\partial_t + \mathbf{u} \cdot \nabla \right) \mathbf{u} = \nabla \cdot \mathbf{\Pi} \, . \tag{2.12}$$

Here, the left-hand side denotes the material (or convected) derivative, capturing the total time rate of change of momentum for a fluid element advected by the flow. The right-hand side represents the net force per unit volume, expressed as the divergence of the stress tensor $\mathbf{\Pi}$, which accounts for all internal stresses acting on the fluid.

One contribution to the stress tensor comes from viscous dissipation. When adjacent fluid layers slide past one another, they exert drag forces that act to reduce velocity gradients and redistribute momentum. This viscous effect is described by the viscous stress:

$$\mathbf{\Pi}^{visc} = 2\eta \mathbf{E} \, , \tag{2.13}$$

where η is the dynamic shear viscosity, which we have assumed to be a scalar, an isotropic approximation of the full viscous stress tensor which is anisotropic in general and given in terms of the six Leslie coefficients [51]. $\mathbf{E} = \frac{1}{2}[(\nabla \mathbf{u}) + (\nabla \mathbf{u})^T]$ is the strain rate tensor, given by the symmetric part of the velocity gradient tensor. The formulation of the stress tensor $\mathbf{\Pi}$ provided here is not yet complete. In the sections that follow, we introduce additional terms to capture both passive elastic stresses and active contributions that drive the rich dynamics observed in active nematic systems.

Equations (2.11), (2.12) and (2.13) together define the Navier–Stokes equations for a viscous Newtonian fluid. We will approximate the large-scale collective dynamics of our systems by considering a non-Newtonian, viscous fluid.

The relative importance of inertial and viscous effects is captured by the Reynolds number, $\mathrm{Re} \sim UL\rho/\eta$, where U and L are characteristic velocity and length scales, respectively. In all cases considered in this thesis, the typical velocities and system sizes under consideration are sufficiently small that $\mathrm{Re} \ll 1$. This places the systems firmly in a low-Reynolds-number regime, where viscous effects dominate. Consequently, it is standard practice to neglect the non-linear advective terms in Eq. (2.12).

2.4 Nemato-hydrodynamics

In this section, we establish the coupling between the velocity field and the nematic order parameter to derive the full dynamical equations governing the evolution of a nematic liquid crystal.

The time evolution of the nematic order parameter $\mathbf{Q}$ is governed by the Beris–Edwards equation [55]:

$$D_t\mathbf{Q} - \mathcal{W} = \Gamma \mathbf{H}\,, \tag{2.14}$$

where $D_t\mathbf{Q}$ is the material derivative representing the advection of $\mathbf{Q}$ with the flow. The RHS of Eq. (2.14) corresponds to the relaxation of $\mathbf{Q}$ toward the minimum of the free energy $\mathcal{F} = \int (f_{\mathrm{bulk}} + f_{\mathrm{elastic}})\, dV = \int f\, dV$, where f_{bulk} and $f_{elastic}$ are defined in Eqs. (2.6) and (2.8) respectively. This is governed by the molecular field:

$$\mathbf{H} = -\left(\frac{\delta \mathcal{F}}{\delta \mathbf{Q}} - \frac{\mathbb{I}}{d}\mathrm{Tr}\left(\frac{\delta \mathcal{F}}{\delta \mathbf{Q}}\right)\right)\,, \tag{2.15}$$

where Γ is the rotational diffusivity, determining how strongly the system is driven toward thermodynamic equilibrium and d the dimension of the system.

The term $\mathcal{W}$ captures the rotation and stretching of the director field due to flow-induced strain and vorticity [20, 55, 63]. It is

$$\mathcal{W} = (\xi\mathbf{E} + \mathbf{\Omega})\cdot\Big(\mathbf{Q} + \frac{\mathbb{I}}{d}\Big) + \Big(\mathbf{Q} + \frac{\mathbb{I}}{d}\Big)\cdot(\xi\mathbf{E} - \mathbf{\Omega}) - 2\xi\Big(\mathbf{Q} + \frac{\mathbb{I}}{d}\Big)(\mathbf{Q} : \mathbf{E})\,, \tag{2.16}$$

where $\mathbf{\Omega} = \frac{1}{2}[(\nabla\mathbf{u}) - (\nabla\mathbf{u})^T]$ is the vorticity tensor, given by the anti-symmetric part of the velocity gradient tensor.

The parameter ξ is a phenomenological flow-alignment parameter that controls the extent to which the director aligns with the local strain. Physically, ξ characterises the relative influence of shear-induced alignment versus vorticity-driven rotation (see Fig. 2.3). When $\xi = 0$, the orientation field experiences only rigid-body rotation via $\mathbf{\Omega}$. For larger values of ξ, the contribution of $\mathbf{E}$ increases, enhancing alignment with shear flow—a behavior typical of elongated particles [55]. In biological systems, the effective value of ξ may also reflect the ability of cells to align with flows or minimise internal strain through active processes [64, 65]. Throughout this thesis, we treat ξ as an effective parameter, tuning its value as required to capture relevant behavior.

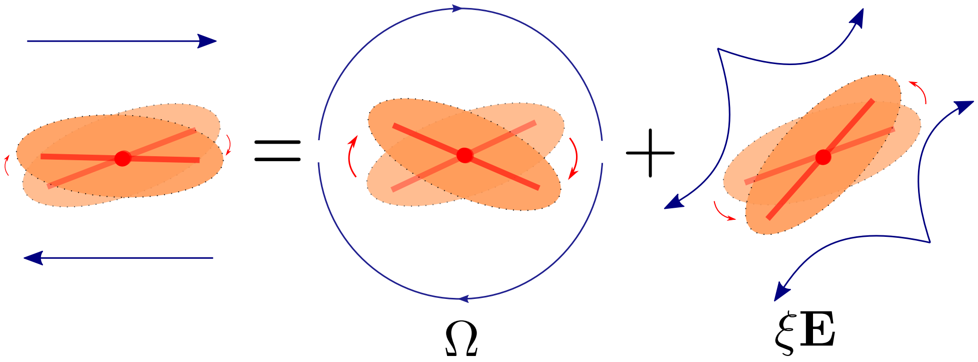

Figure 2.3: The response of the orientation field (orange) to the flow field (blue) has two components: rotation driven by the vorticity tensor $\mathbf{\Omega}$, and alignment with the stretching axis of the shear, described by the strain rate tensor $\mathbf{E}$. The relative importance of these terms is given by the flow-alignment parameter ξ, which is a phenomenological parameter.

To illustrate the effect of the co-rotation term, consider a simplified example in which nematic particles are subjected to a uniform shear flow $u_x(y) = \dot{\gamma}y$, with shear rate $\dot{\gamma}$. Let the bulk free energy be defined by Eq. (2.6), with equilibrium order parameter $0 \leq S_{\mathrm{eq}} \leq 1$, and assume $\dot{\gamma}\xi \gg \Gamma A_Q$. This system always relaxes to a uniform state, allowing us to neglect the elastic energy density f_{elastic}. Setting $S = 2/3$, its steady state value, and letting the director take the form

$\mathbf{n} = (\cos\theta, \sin\theta)$, we arrive at what is commonly known as the Ericksen-Leslie (EL) limit of Eq. (2.14). The angle θ evolves according to:

$$\dot{\theta} = \frac{\dot{\gamma}}{2}(\xi \cos 2\theta - 1). \tag{2.17}$$

The two contributions within the parentheses arise from alignment with the strain rate and rotation by vorticity, respectively. For $\xi < 1$, the system enters a tumbling regime in which θ rotates indefinitely with a non-uniform angular velocity. For $\xi > 1$, the director relaxes to a fixed orientation - the flow-aligned state - described by the Leslie angle $\theta_L = \frac{1}{2}\arccos\left(\frac{1}{\xi}\right)$. Notably, the shear rate $\dot{\gamma}$ scales out of the dynamics, so the final steady state is independent of its value. We will revisit this result in a later chapter.

In cases where distortions in the nematic field are preserved even against the restoring effects of the elastic free energy, they induce additional stresses in the fluid, leading to feedback on the flow. The associated stress contribution adds another term to the total stress tensor in Eq. (2.12) [21]:

$$\begin{aligned} \mathbf{\Pi}^{el} &= 2\xi\Big(\mathbf{Q} + \mathbb{I}/d\Big)(\mathbf{Q} : \mathbf{H}) - \xi\mathbf{H} \cdot \Big(\mathbf{Q} + \mathbb{I}/d\Big) - \xi\Big(\mathbf{Q} + \mathbb{I}/d\Big) \cdot \mathbf{H} \\ &\quad - \Big(\nabla\mathbf{Q}\Big) \cdot \frac{\partial f}{\partial \nabla\mathbf{Q}} + \mathbf{Q} \cdot \mathbf{H} - \mathbf{H} \cdot \mathbf{Q}\,. \end{aligned} \tag{2.18}$$

This expression may be understood physically as follows: A spatially varying Q-tensor increases the elastic free energy, and the functional derivative of this free energy with respect to orientation gradients gives rise to an elastic stress that tends to relax the distortion. When momentum is allowed to evolve, this stress may generate flows that, in turn, influence the evolution of the nematic configuration, completing the two-way coupling between flow and orientation nematic systems. In passive systems, these are the Onsager-reciprocal couplings [55] which act to restore equilibrium alignment. However this need not be the case in active systems which exhibit richer behaviour due to the interplay of active and passive stresses.

2.5 Addition of activity

Up to this point, we have described a nematic liquid crystal in terms of the coupled orientation order parameter and flow field. We now extend this framework to account for active forces that nematic systems exert internally. These forces are incorporated through an additional active stress term in the hydrodynamic equations. In this section, we introduce the microscopic origin of active stresses and explore some of their consequences.

Force dipoles

If we consider the constituent particles that make up the nematic as self-propelled, then by Newton's third law, the forces exerted on the fluid by the particles is equal and opposite to the forces exerted by the fluid on the particles. Therefore, the combined system of the constituent particles and the fluid must be force-free and the associated force density must integrate to zero [26].

A minimal model for nematic active forcing is a force dipole: two equal and opposite forces applied along the particle's axis of elongation. We coarse-grain these microscopic forces into an effective active stress. To illustrate this, consider a system of many active nematic particles labelled by the index i of length $2l$, each centered at position $\mathbf{r}^{(i)}$ and oriented along the unit vector $\mathbf{a}^{(i)}$, as shown in Fig. 2.4. Each particle generates a pair of equal and opposite forces of magnitude F_ζ at its ends. The net active force density at position $\mathbf{r}$ is given by [26]:

$$\nabla \cdot \mathbf{\Pi}^{act}(\mathbf{r}) = \mathbf{F}^{act}(\mathbf{r}) = F_\zeta \sum_i \mathbf{a}^{(i)} \left[-\delta(\mathbf{r} - \mathbf{r}^{(i)} + l\mathbf{a}^{(i)}) + \delta(\mathbf{r} - \mathbf{r}^{(i)} - l\mathbf{a}^{(i)}) \right] , \tag{2.19}$$

where $\mathbf{\Pi}^{act}$ is the active stress, and the sum runs over all particles near $\mathbf{r}$.

Assuming the particle size l is much smaller than the coarse-graining length scale ($l \ll |\mathbf{r} - \mathbf{r}^{(i)}|$), we can Taylor expand the delta functions to obtain:

$$\nabla \cdot \mathbf{\Pi}^{act}(\mathbf{r}) = \mathbf{F}^{act}(\mathbf{r}) \approx -F_\zeta \, (2l) \, \nabla \left[\sum_i \mathbf{a}^{(i)} \mathbf{a}^{(i)} \delta(\mathbf{r} - \mathbf{r}^{(i)}) + \dots \right] . \tag{2.20}$$

We then coarse-grain the microscopic dipolar contributions by replacing the discrete sum over particles weighted by delta functions with smooth fields defined on a mesoscopic volume. Specifically, the number density is replaced by its coarse-grained counterpart, $\phi(\mathbf{r})$ and the microscopic dyad $a^{(i)}a^{(i)}$ is replaced by its local orientational average, $\langle a_i a_j \rangle$ which, in a nematic, reduces to the $\mathbf{Q}$ tensor, minus an isotropic contribution which becomes irrelevant. Putting this altogether, we arrive at the following form for the active stress:

$$\mathbf{\Pi}^{act}(\mathbf{r}) = -\zeta\,\phi(\mathbf{r})\,\mathbf{Q}(\mathbf{r})\,. \tag{2.21}$$

In systems with uniform particle density, $\phi(\mathbf{r}) = \text{const.}$, this factor can be absorbed into ζ, yielding a simplified form of the active stress [20]:

$$\mathbf{\Pi}^{act} = -\zeta\mathbf{Q}\,. \tag{2.22}$$

The sign of the activity coefficient ζ determines the nature of the active stress. For $\zeta > 0$, the dipolar forces of the coarse-grained nematogens are such that they push outwards from the long axes, and pull inwards along their short axes, corresponding to extensile (pusher) behaviour. When $\zeta < 0$, the forces pull inward, corresponding to contractile (puller) behaviour. These two types of active forcing generate distinct flow fields, as illustrated in Fig. 2.4. A more detailed derivation of the active stress from microscopic dynamics can be found in Ref. [21]. Here, it is worth noting that the active stress does indeed break equilibrium. One cannot write such a contribution to the stress tensor in terms of an elastic stress. Indeed, a simple, but lengthy calculation of the change in entropy would yield that the active stress, (2.22) would give a finite contribution [21].

The full stress tensor for an active nematic fluid then takes the form:

$$\mathbf{\Pi} = \mathbf{\Pi}^{visc} + \mathbf{\Pi}^{el} + \mathbf{\Pi}^{act}\,, \tag{2.23}$$

where the individual terms are the viscous stress $\mathbf{\Pi}^{visc}$ from Eq. (2.13), the elastic stress $\mathbf{\Pi}^{el}$ from Eq. (2.18), and the active stress $\mathbf{\Pi}^{act}$ from Eq. (2.22).

In the next section, we explore the physical consequences of this active stress term on the behavior of nematic systems.

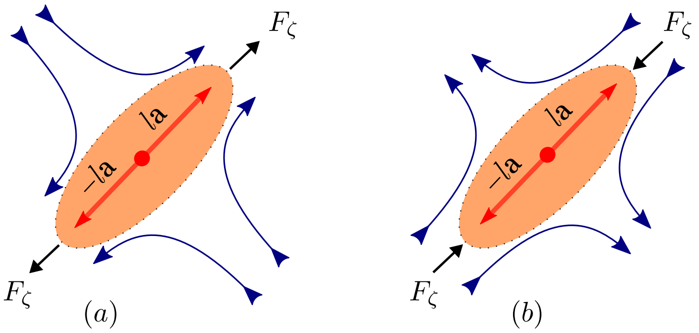

(a) (b)

Figure 2.4: Cells exert active forces on their environment. For active nematic force dipoles, these can be categorised as **(a)** extensile (pusher, $\zeta > 0$) or **(b)** contractile (puller, $\zeta < 0$) forces (shown in black). The blue arrows indicate the flow fields generated by these active stresses.

2.5.1 Active turbulence

The equations of active nemato-hydrodynamics couple the nematic tensor and flow field. Gradients in the orientation give rise to active forces, setting up gradients in the flow field. These, in turn, rotate the director field, changing the active forces in the system. In this subsection, we look at how active dipolar forces and this feedback loop can lead to a chaotic flow state known as active turbulence.

Hydrodynamic instabilities

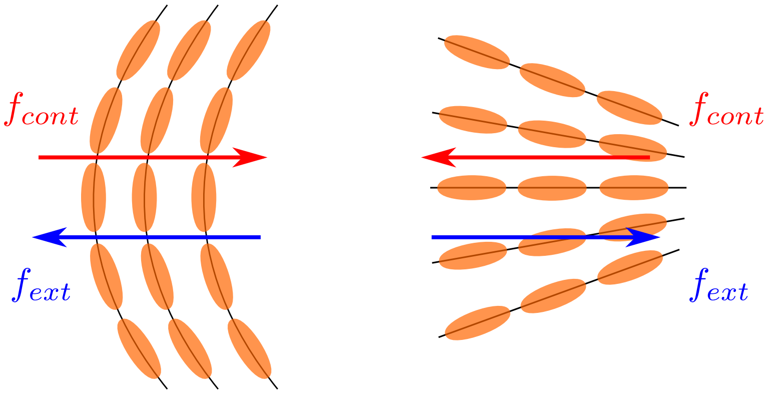

(a) (b)

Figure 2.5: The typical distortions in two-dimensional nematics are (a) bend and (b) splay. Blue/red arrows show the direction of extensile/contractile active forces respectively.

For temperatures below the transition temperature T_N, the lowest energy configuration of a nematic liquid crystal with finite elasticity corresponds to a system of finite order, whose value depends on the form of the free energy and its parameters, with no spatial gradients in the director field. In the absence of activity, this state is stable under perturbations - any small distortion in the nematic field creates elastic restoring forces which drive the system back to the aligned phase.

Introducing activity destabilises the uniform nematic state. For an extensile nematic, bend perturbations in the director field lead to active forces in the fluid which set up flows that increase the perturbation even further [26]. For contractile nematics, the same is true for splay perturbations instead, as shown in Fig. 2.5.

In both cases, these instabilities lead to regions where the bend/splay distortions become more pronounced, forming domain walls with distortions in the director field and large elastic energies. When the distortions become large enough, the nucleation of $\pm 1/2$ defects takes place. The $+1/2$ defects self-propel due to their polar shape [66], moving from tail to head for extensile nematics and head to tail in contractile ones. The $-1/2$ defects, by contrast, are non-motile but produce symmetric swirling flows [66]. The direction of these flows is opposite between extensile and contractile nematics. Topological defects are a field of great interest in active matter [67] and have been shown to be the drivers of important processes in biological systems such as acting as organisation centres during morphogenesis in the marine invertebrate Hydra [68] and cell accumulation/depletion at positive/negative defects respectively during epithelial morphogenesis [69, 70].

Active turbulence

The uniformly aligned nematic configuration becomes unstable in the presence of activity. This leads to the emergence of out-of-equilibrium, dynamical steady states in which both the director and flow fields exhibit spatio-temporal disorder. These states are populated by a fluctuating number of topological defects that continuously form and annihilate across the system. This dynamical regime is what is referred to as active turbulence (see Fig. 2.6) [20, 26, 71]. Despite its chaotic appearance, active turbulence exhibits robust statistical features, which are encoded in the spatial and temporal correlations of the director and velocity fields [33].

The characteristic scale of patterns observed in active turbulence results from a balance between active and elastic stresses. While elastic stresses scale as $\mathbf{\Pi}^{el} \propto K_Q l^{-2}$, the active stress is lengthscale-independent, $\mathbf{\Pi}^{act} \propto |\zeta|$. This competition selects a characteristic vortex size or distortion scale known as the active lengthscale, given by $L_{act} = \sqrt{K_Q/|\zeta|}$. Notably, this same lengthscale governs the typical spacing between bend and splay deformations in the nematic field [33, 72, 73]. In addition to a characteristic lengthscale, active turbulence is associated with a timescale $t_{act} = \eta/|\zeta|$, which decreases as the activity increases.

This framework differs fundamentally from classical turbulence in inertial fluids, where energy cascades across scales. In contrast, active turbulence injects and dissipates energy primarily at the scale of the individual nematogens, with no significant transfer of energy between scales [33].

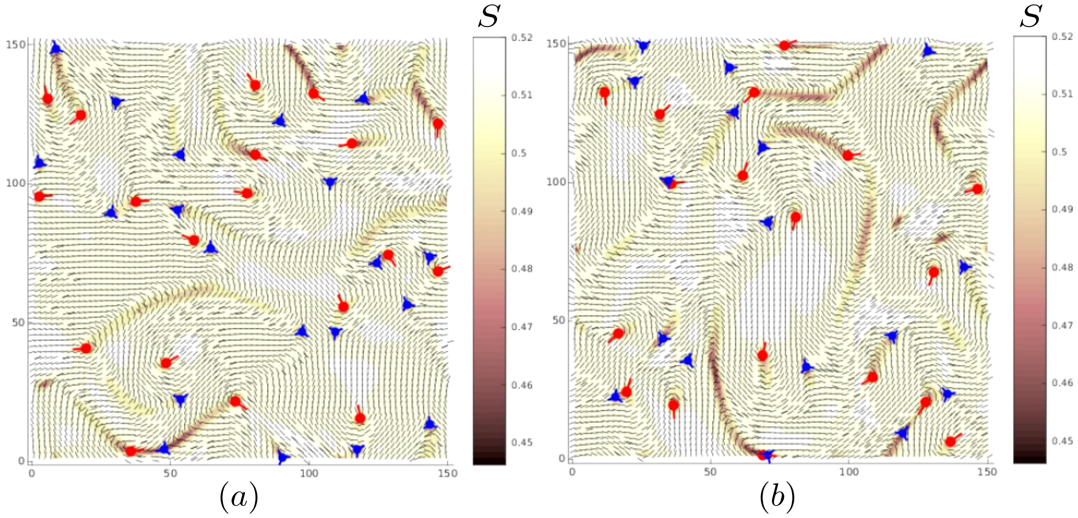

Figure 2.6: Typical snapshots of an active nematic undergoing active turbulence. Panels (a) and (b) show the orientation field with $\pm 1/2$ defects labelled in red/blue respectively at two different points in time. The field lines correspond to the director field $\mathbf{n}$ and the colour bar gives the magnitude of the nematic order parameter, S.

It is worth noting that although bulk active nematics are generically turbulent, confinement can significantly alter the flow behaviour. When the system is confined on a scale comparable to L_{act}, distinct and often more ordered flow patterns can emerge.

2.6 Numerical methods

We model active nematic systems numerically by solving the coupled dynamics of the velocity field $\mathbf{u}$, Eqs. (2.11) and (2.12)) and the orientation field $\mathbf{Q}$, govern by Eq. (2.14) simultaneously. In practice, the $\mathbf{Q}$ tensor is evolved using a finite-difference scheme following Refs. [63, 74]. Derivatives are approximated numerically using a five-point finite difference stencil [75]. For the fluid field, we employ the Lattice-Boltzmann (LB) method [62]. We use a uniform Cartesian grid and use simulation units where the length-scales and time-scales are normalised to unity, which we refer to as LB units. Further details of the hybrid Lattice-Boltzmann method are described in Appendix A In the literature, alternative methods such as finite-element (FEM) schemes [76] and pseudo-spectral solvers [77] have been employed.

The LB solver is employed to update the velocity field according to Eq. (2.12), incorporating a BGK collision operator and additional forcing terms to capture body forces and stresses [62]. For computational efficiency, we simulate an isothermal fluid rather than an exactly incompressible one. While we retain the advective and inertial terms in the momentum equation, density fluctuations in the simulation are small and rapidly dissipated by pressure waves that propagate on a timescale much faster than the physical dynamics [78]. As a result, the system is effectively incompressible, with relative density deviations on the order of 0.01%.

We also note that although inertial contributions are included, the Reynolds number for our simulations is extremely low - $Re \approx 0.003 - 0.004$. This ensures that viscous stresses dominate over inertial effects, as is typical in biological flows and soft matter systems.

2.7 Summary

In this chapter, we introduced the continuum theory of passive and active nematics as a model for describing collective behaviours in dense layers of nematic particles. We described a theoretical framework involving a tensorial order parameter $\mathbf{Q}$, which captures the local orientational order's magnitude and direction, and a flow field **u**, which encodes fluid transport. The dynamics of these fields were analysed individually, and then coupled via the Beris-Edwards formulation of nemato-hydrodynamics.

We then incorporated activity into the model, representing mechanical forces generated by living cells internally as an active stress tensor derived via coarse-graining. This gave rise to hallmark features of active matter, including spontaneous flow, topological defect dynamics, and the onset of active turbulence.

Throughout the remainder of this thesis, we treat these hydrodynamic equations as a baseline model for the systems we will be studying. We will extend this framework to include deformability of constituent particles and explore how such shape changes interact with external driving and active forces to influence system dynamics and collective flows.

3

Deformable Nematics

In this chapter, we introduce a minimal extension to the nemato-hydrodynamic model to incorporate deformability of soft constituent particles in two dimensions. We begin by considering the equations that govern the evolution of the shape of deformable particles. We then couple these equations with those of the orientational order parameter and the flow field to arrive at a full system of coupled partial differential equations that describe a system of deformable nematics. Finally, we use this model to analyse simple channel flows of passive, deformable nematics with external driving, namely Couette and Poiseuille flows. We show that the introduction of shape as a dynamical variable leads to experimentally verifiable, novel dynamics that cannot be captured by the models of rigid liquid crystals.

3.1 Introduction

Deformable particles are attracting considerable interest at the intersection between soft matter and biological physics due to the emergent dynamics linked with their geometry [4]. Both microscopic and macroscopic behaviours of deformable material may be traced back to their ability to change their shape, either through inter-particle interactions, or through flow induced deformations. Shape changes of individual colloids such as drops, vesicles and capsules in shear flow have been considered

[5–7], and recent studies have focused on the development of models to describe the dynamics of motile, deformable particles [79–86]. However, continuum frameworks that incorporate deformability and lead to predictions that are experimentally verifiable are required to further advance this field.

Furthermore, deformability is a characteristic feature of biological matter: MDCK cells [8, 9] and embryonic tissue [10–14] exhibit significant variations in their shape. Cell deformability is increasingly being recognised as an important aspect in cancer metastasis [87–89]. Recently, studies of glioblastoma in mice and humans showed that highly elongated and nematically aligned tumour cells invade the surrounding, healthy and round cells in a stream [90] resulting in a spatial distribution of both tumour and non-tumour cells. Experiments have also demonstrated the distinct role of flow induced shear strain on the viability of cells in vasculature [15, 16]. Therefore, the understanding of the link of shape dynamics to motion and orientational dynamics is a key ingredient to a complete description of real life systems composed of deformable particles.

This chapter is structured as follows: In Sec. 3.2 we develop a minimal model to account for particle shape through the introduction of a new dynamical variable - the aspect ratio of particles. We then couple this back to the nemato-hydrodynamic equations. Following this, in Secs. 3.3 and 3.4, we use analytics and numerical simulations within this continuum model of deformable nematic particles in Couette and Poiseuille flows, respectively, to reveal novel dynamics. Finally, we summarise the results in Sec. 3.5.

3.2 Model of deformable nematics

Shape evolution of particles

We begin by approximating the constituent particles that make up the nematic as ellipses whose shape is parametrised by one scalar variable, their aspect ratio, ω. In doing so, we neglect any information about the area or volume of particles. This is analogous to the stress tensor of deformable polymers, which have been studied under several models, such as the dumbbell and Rouse models [91]. The dynamical equation that governs the evolution response of ω due to a flow field has been derived on based on the theory of Neo-Hookean solids in the past [92–94]. Here, we present an alternate derivation based on physical principles and symmetry arguments that arrives at the same equations, up to a constant of proportionality.

We define the aspect ratio $\omega \geq 1$ as the ratio of the semi-major to semi-minor axes of the elliptical particles. Any strain along the director field will stretch the particle further, thus increasing the length of the long axis, and in turn, ω, whereas strain in the perpendicular direction will increase the length of the short axis, and therefore decrease ω. The simplest form of the time evolution of ω is then given by:

$$\begin{aligned} \frac{d\omega}{dt} &\propto (E_{\parallel} - E_{\perp}), \\ \frac{d\omega}{dt} &= f\left(\omega\right)(E_{\parallel} - E_{\perp}). \end{aligned} \tag{3.1}$$

Where $E_{\parallel}$ and $E_{\perp}$ are the projections of the strain rate tensor, E_{ij}, parallel and perpendicular to the orientation of the long axis, respectively. Physically, these correspond to the decomposition of the strain rate felt by the particles along the two principal axes, which we take to contribute equally to the evolution of their shape for simplicity. f is a function only of the aspect ratio since any dependence on position and time enters through E_{ij}. To determine this unknown function, let us repeat the above argument for the inverse of ω. Clearly,

$$\begin{aligned} \frac{d\left(1/\omega\right)}{dt} &\propto (E_{\perp} - E_{\parallel}), \\ \frac{d\left(1/\omega\right)}{dt} &= f\left(1/\omega\right)(E_{\perp} - E_{\parallel}). \end{aligned} \tag{3.2}$$

The function $f\left(1/\omega\right)$ appears because there is nothing special about defining the aspect ratio as the ratio of the long over short axes, hence the functional form must be the same, but with the argument inverted. Now, we may write down the above once more, using the chain rule:

$$\frac{d\left(1/\omega\right)}{dt} = \frac{1}{\omega^2} f\left(\omega\right)(E_{\perp} - E_{\parallel}). \tag{3.3}$$

Comparing Eq. (3.2) and Eq. (3.3), we arrive at the following functional equation

$$\frac{f(\omega)}{\omega^2} = f\left(1/\omega\right). \tag{3.4}$$

Assuming that the functions $f(\omega)$ and $f\left(1/\omega\right)$ are C^∞ in the interval $[0,\infty)$, we may show that there are two unique solutions to Eq. (3.4) through power series expansions:

$$f(\omega) = \sum_{n=0}^{\infty} a_n \omega^n,$$

$$f\left(1/\omega\right) = \sum_{n=0}^{\infty} a_n \omega^{-n}.$$

Substituting the power series into Eq. (3.4), we arrive at the following:

$$\sum_{n=0}^{\infty} a_n(\omega^n - \omega^{2-n}) = 0. \tag{3.5}$$

We therefore have two solutions to Eq. (3.5). The first requires all $a_n = 0$, implying that $f(\omega) = 0$, which describes rigid particles. The second, which is relevant to this thesis, is where all $a_n = 0$ except for a_1, so that $f(\omega) = a_1\omega$, where a_1 is an unknown constant. We take the value of a_1 to be unity, in agreement with Refs. [92–94]. Finally, after including advection, free energy relaxation and noting that for an incompressible system $E_\perp = -E_\parallel$, we arrive at the following dynamical equation:

$$\left(\partial_t + \mathbf{u}\cdot\nabla\right)\omega = 2\omega E_\parallel - \Gamma_\omega \frac{\delta \mathcal{F}}{\delta \omega}. \tag{3.6}$$

Note that this is an approximation where we take the evolution of ω for a single particle and used it in a continuum limit. The LHS of Eq. (3.6) is simply the partial time derivative, and advection of ω. The first term on the RHS is the flow-driven component we have derived. $E_\parallel$ is recognised as the projection of the strain rate onto the director field, *i.e.* $E_\parallel = n_i E_{ij} n_j$. When this term is positive, the flow will tend to elongate the particles, and vice versa when it is negative. The final term on the RHS is a relaxation towards a free energy minimum. In our extended model of deformable nematics, we include an additional free energy component due to shape deformations:

$$f_\omega = A_\omega \frac{1}{2}(\omega - \omega_0)^2 + A^\star_\omega \frac{1}{4}(\omega - \omega_0)^4\,, \tag{3.7}$$

where ω_0 is the particle aspect ratio at equilibrium, *i.e.* the shape that the constituent particles that make up the nematic inherently prefer to have, and A_ω, $A^\star_\omega$ are elastic deformation parameters which penalise deviations of ω from ω_0. In this thesis, we primarily concern ourselves with inherently circular particles, $\omega_0 = 1$.

Coupling of shape to orientational dynamics

So far, we see from Eq. (3.6) how the director and flow fields affect the evolution of the shape of the nematic particles. We will also couple the shape of the particles back to their orientational dynamics, and consequently the flow field. One way to do this is through thermodynamic effects. Physically, we expect highly anisotropic particles in a confluent layer to align nematically due to excluded volume effects whereas there is no alignment interaction between circular particles. Therefore, in the bulk free energy density, given by Eq. (2.6), we make a choice of $S_{eq} = S_{eq}(\omega) = (\omega - 1)/\omega$. Note that this choice, while purely phenomenological, is consistent in the extreme limits. Namely for $\omega \to 1$, $S_{eq} \to 0$, circular particles cannot nematically align, whereas for $\omega \to \infty$, $S_{eq} \to 1$, infinitely long particles will tend to align perfectly due to strong volume exclusion effects.

We may also couple the shape to the orientational dynamics characterised by Eq. (2.14) through the flow-driven effects. In particular, the value of the flow alignment parameter, ξ, depends on the shape and it is zero for circular particles [95, 96]. In this work, we make a linear approximation, $\xi(\omega) = \xi_0(\omega - 1)$ where ξ_0 sets the flow-alignment scale. Since ξ appears in the elastic stress in Eq. (2.18), we now have explicit coupling between the nematic tensor $\mathbf{Q}$, the flow field $\mathbf{u}$ and the shape of particles, ω. This creates the basis of our extended model of nemato-hydrodynamics of deformable particles. To get a better understanding of the interplay of all the variables in the model, we begin by analysing the dynamics in simple cases.

3.3 Couette flow

3.3.1 Circular particles

Constant nematic order

Consider a system in the Ericksen-Leslie (EL) limit as in Sec. 2.4 which we justify below. Defining the shape variable $r = \omega - 1$ which quantifies the degree of elongation of particles, the resulting dynamical equations for the director field and particle shape are given by:

$$(\partial_t + \mathbf{u}\cdot\nabla)\, n_i = -\lambda n_i + \xi\,(r)\, E_{ij} n_j - \Omega_{ij} n_j - \Gamma \frac{\delta \mathcal{F}}{\delta n_i}, \tag{3.8}$$

$$(\partial_t + \mathbf{u}\cdot\nabla)\, r = 2(r+1)E_{\parallel} - \Gamma_r \frac{\delta \mathcal{F}}{\delta r}, \tag{3.9}$$

where the flow alignment parameter is now explicitly a function of r, $\xi(r) = \xi_0 r$ and we have relabelled parameter subscripts from $\omega \to r$ for clarity. The constant λ is a Lagrange multiplier that guarantees that $\mathbf{n}$ is a unit vector. The free energy, $\mathcal{F} = \int (f_r + f_n)\,\mathrm{d}\mathbf{A}$ now consists of two contributions. The first of these is associated with particle shape deformations given by Eq. (3.7) which we restate here in terms of r, $f_r = \frac{A_r}{2}(r - r_0)^2 + \frac{A_r^\star}{4}(r - r_0)^4$, where $r_0 = \omega_0 - 1$. The second contribution, f_n, arising from the nematic elasticity given by Eq. 2.7, in the one elastic constant approximation is $f_n = \frac{K(r)}{2}\left(\nabla \mathbf{n}\right)^2$, where $K(r)$ is the elastic constant associated with the orientational order of the deformable particles and can, in general, also be a function of the shape of the particles.

We first consider a continuum of deformable particles confined between two parallel plates in 2D subjected to simple shear flow, described by the velocity profile $u_x = \dot{\gamma} y$. Along the channel, $\hat{x}$ direction, we assume translational invariance. In the model of rigid nematics discussed in Chapter 2.4, this has previously resulted in Eq. (2.17) for the orientation angle of the director field and was justified in the limit $\dot{\gamma}\xi_0 \gg \Gamma A_Q$. This is the limit we consider in this section, and we discuss the reverse limit, $\dot{\gamma}\xi_0 \ll \Gamma A_Q$ in Sec. 3.3.1. The strain rate tensor for this two dimensional parallel flow, when diagonalised in the basis of the principal axes of the particles, reads $\frac{\dot{\gamma}}{2}\left(\begin{smallmatrix} 1 & 0 \\ 0 & -1 \end{smallmatrix}\right)$ indicating extension and compression along the principal axes. In other words an isotropic material element will deform along the principal axis of deformation [97, 98], defined as the eigenvector of the strain rate tensor with the most positive eigenvalue, in addition to the rotation induced by the vorticity tensor.

Defining the director of the elongated particles $\mathbf{n} = (\cos\theta, \sin\theta)$, where $\theta \in (-\pi/2, \pi/2]$ is the angle to the flow direction, and non-dimensionalising time,

$t' = (\Gamma_r A_r)t$, the governing Eqs. (3.8) and (3.9) simplify to

$$\dot{r} = \alpha(r+1)\sin 2\theta - (r - r_0)\left(1 + \epsilon(r - r_0)^2\right), \tag{3.10}$$

$$\dot{\theta} = \frac{\alpha}{2}\left(\xi_0 r \cos 2\theta - 1\right), \tag{3.11}$$

where $\alpha \equiv \dot{\gamma}/\left(\Gamma_r A_r\right)$ is a Péclet number that quantifies the relative importance of the shear to the resistance to deformation, and $\epsilon \equiv A_r^*/A_r$ is the ratio of the elastic deformation parameters. In the following analysis we use $\epsilon = 0.1$ and consider the case of inherently circular particles, *i.e.,* with equilibrium shape $r_0 = 0$. Due to the lack of inertia in our system, we impose that whenever r vanishes, the orientation is set in the direction of the principal axis of deformation, which in the case of Couette flow is given by $\theta = \pi/4$. This is physically motivated as follows: If particles are being exposed to a shear at an angle such that it compresses them to an isotropic shape where there is no attributable orientation, then it follows that the particles will re-elongate along the principal axis of deformation of the given shear, where its elongating effects are at their strongest. In practice, this creates kinks in the evolution of θ of all systems we study as we are forced to discontinuously attribute a new value to θ whenever an orientation may not be defined. This effect may also be included more naturally in Eq. (3.11) by adding a term $\propto \delta(r)\cos 2\theta$ to the RHS. A similar treatment may be done for more general cases.

Dynamical states diagram

We construct a state diagram by varying the applied shear rate, (*i.e.* Péclet number α) and the flow-alignment scale (ξ_0). Recall that, in the case of a system of rigid particles, the evolution of the orientation angle, given by Eq. (2.17), shows the transition between the tumbling and flow-aligned states to depend only on the constant value of the flow-alignment parameter and not on the applied shear rate. However, due to the added coupling to the shape of the particles, we identify three distinct regions with qualitatively different dynamics as shown in Fig. 3.1.

Region I corresponds to a periodic behaviour in the shape and orientation of the deformable nematic particles as shown schematically in Fig. 3.1 (see also

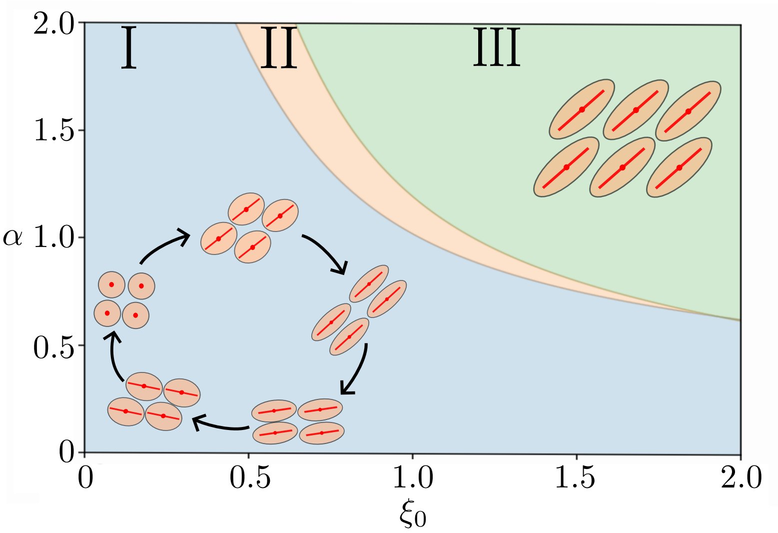

Figure 3.1: Dynamics of a continuum of deformable particles characterised in {Péclet number (α), flow-alignment scale (ξ_0)} parameter space. Region I: particles undergo cycles of elongation, re-orientation and contraction, III: particles align at a fixed angle to the flow, and II: both oscillatory and alignment behaviours are possible depending on initial conditions. The schematics of particles in region I and III illustrate the oscillatory and steady state behaviours.

Fig. 3.3(a)). This cycle of elongation, reorientation, and contraction, emerges from the deformability of the particles. To understand this, let us consider circular ($r = 0$) particles at $t = 0$. In the absence of any inertial effects, the imposed shear flow initially elongates the particles along the principal axis of deformation ($\theta = \frac{\pi}{4}$) and $r(t)$ increases. Simultaneously the vorticity component of the shear flow rotates the particles away from the principal axis. Therefore the strain rate projected along the shape direction decreases, which results in a decrease in the elongation of the deformable particles. When they regain a circular shape, they are strained along the principal axis again and the cycle repeats, as illustrated by the jumps in the evolution of θ in Fig. 3.3(a). This is akin to, but qualitatively different to the tumbling dynamics observed in rigid nematics. The time period of these shape oscillations decreases with an increase in the shear rate, α, and mildly increases with an increase in the flow alignment scale, ξ_0 while the system remains in region I, as shown in Fig. 3.2. In region II, however, increasing α or ξ_0 further allows the limit cycle trajectory in phase space to approach the saddle point. Consequently, the system enters a ghost region [99] in the phase space where the dynamics slow down considerably. In particular, the period of oscillations diverges as the system gets arbitrarily close to the homoclinic bifurcation.

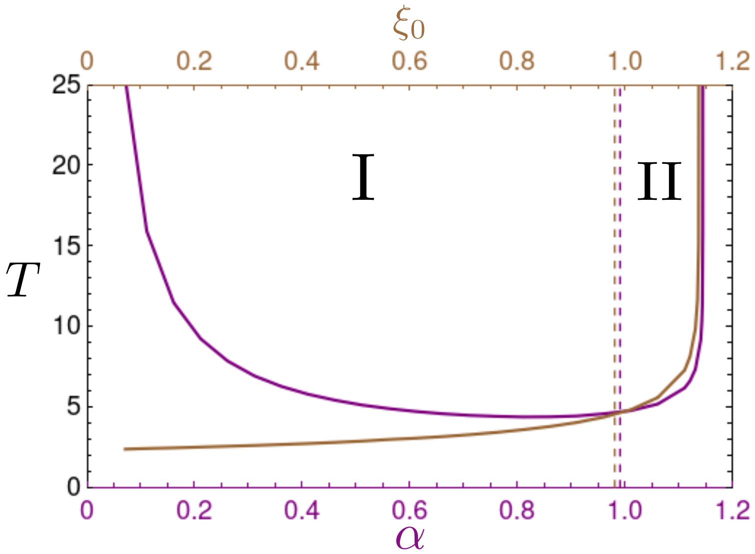

Figure 3.2: Time period, T of shape oscillations in regions I and II as α (purple, $\xi_0 = 1$) and ξ_0 (brown, $\alpha = 1$) are varied.

We note that if $r_0 > 0$ the particles can undergo a full tumbling motion, rotating through 2π without the shape becoming circular. We discuss this case in the next section.

Region III, corresponding to flow alignment, emerges if the imposed shear rate α or the flow alignment scale ξ_0 are sufficiently large. The system reaches a steady state at an angle to the flow $\theta_s = \frac{1}{2}\arccos\left(\frac{1}{\xi_0 r_s}\right)$ and a particle deformation r_s which increases with both α and ξ_0. Fig. 3.3 (c) shows the evolution to a steady state, $r(t') = r_s, \theta(t') = \theta_s$ in region III. The steady alignment angle θ_s reduces to the Leslie angle $\theta_L = \frac{1}{2}\arccos\left(\frac{1}{\xi_0 r_0}\right)$, which describes the angle that rigid nematics make with the flow axis, in the limit $\alpha \ll 1$, with $r_0 > 0$. Deformability introduces a dependence of the alignment angle on the shear rate.

The boundary separating regions I and III is not sharp. In the region labelled II in Fig. 3.1 the initial conditions may drive the system to a flow aligned state or to a state exhibiting shape oscillations. Fig. 3.3 (b) illustrates the bistability of region II; some initial conditions lead to a steady state, whereas others result in shape oscillations.

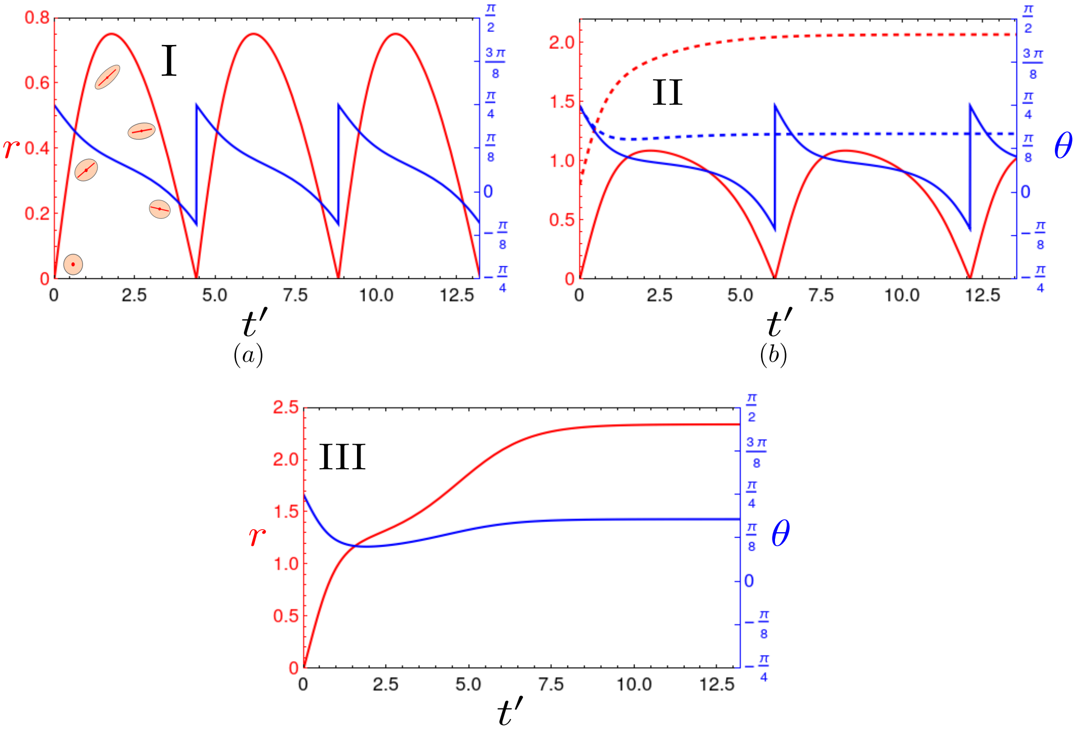

(a)

(b)

(c)

Figure 3.3: Time evolution of r (red) and θ (blue) corresponding to Regions I - III. $\xi_0 = 1$ and $\alpha = \{0.8, 1.0, 1.2\}$ in $(a) - (c)$ respectively. In (a), the oscillatory evolution of the deformable particles is schematically indicated. In (b) solid/dashed lines represent two different initial conditions (circular/elongated particles at $t' = 0$). In (c), the system reaches an aligned state of deformed particles.

Phase space description

A helpful way to clarify the distinction between the three regions is by representing the dynamics of the system in a phase space plot spanned by polar co-ordinates, $\{r, \theta\}$, as shown in Fig. 3.4. In the plots, the radial distance from the origin indicates the extent of deformation (r) while the azimuthal angle measured from the $x-$axis indicates the direction of elongation of the particles (θ). The singular point at the origin corresponds to a circular particle without an attributable orientation. The streamlines correspond to the direction (but not the magnitude) of the time derivatives, $\{\dot{r}, \dot{\theta}\}$. The existence of the three distinct regions is due to the occurrence of two consecutive bifurcations that occur in the $r - \theta$ space, as the parameter α (or equivalently ξ_0) is varied. For small α, all phase space trajectories converge towards the origin (circular shape) and thus join the limit cycle indicated by the red

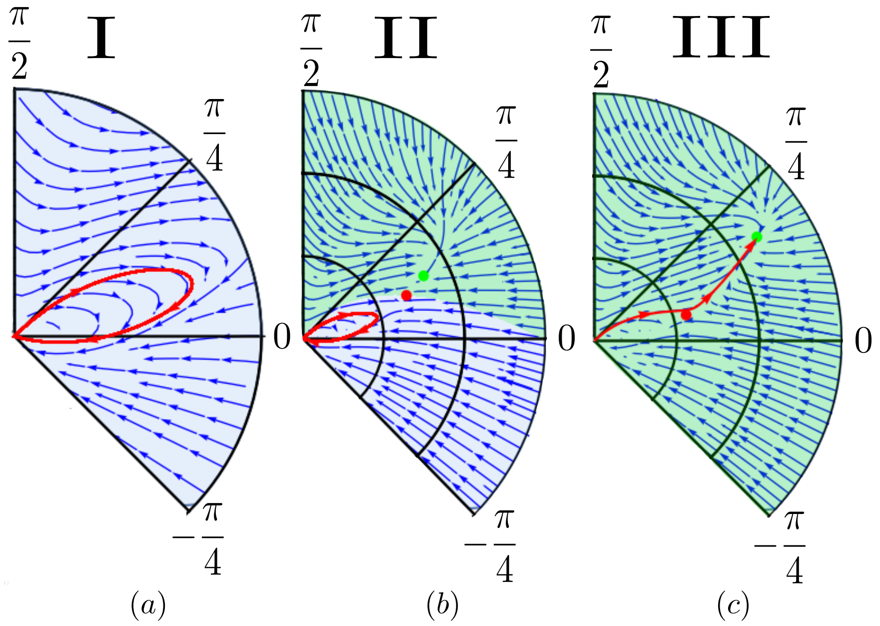

Figure 3.4: Phase space trajectories of the deformable nematics in $\{r, \theta\}$ space. Only a sector of the phase space is shown for brevity. Concentric circles correspond to unit intervals in r. Red trajectories correspond to the initial conditions $\{0, \pi/4\}$. $\xi_0 = 1$ and $\alpha = \{0.8, 1.0, 1.2\}$ in I-III respectively. (a) Region I: all trajectories converge towards the origin, eventually joining the limit cycle indicated by the red curve. (b) Region II: steady state $\{\dot{r} = 0, \dot{\theta} = 0\}$ solutions exist as saddle (red) and stable (green) points. Green background corresponds to the attractor basin of the stable fixed point. (c) Region III: all trajectories ultimately end up at the stable fixed point.

curve in Fig. 3.4 (a). This limit cycle corresponds to the oscillatory shape dynamics observed in region I. As α is increased, a saddle-node bifurcation occurs in the phase space creating an unstable saddle point (in red) and a stable fixed point (in green) as shown in Fig. 3.4 (b), where the basin of attraction of this stable fixed point is shaded in green color. The coexistence of the limit cycle and the stable fixed point results in the bistability observed in region II. Finally, for sufficiently large values of α, a homoclinic bifurcation occurs, the saddle point collides with the limit cycle and the limit cycle opens up as shown in Fig. 3.4 (c). Thus, all solutions converge towards the stable fixed point giving rise to region III.

The phase boundary separating region I from region II and III in Fig. 3.1 can be determined analytically from the requirement that there exists exactly one solution to the steady-state of Eqs. (3.10) and (3.11), *i.e.* we require values of

$\{\alpha, \xi_0\}$ such that the set of equations

$$\alpha(r_s + 1)\sin 2\theta_s - r_s\left(1 + \epsilon r_s^2\right) = 0, \tag{3.12}$$

$$\frac{\alpha}{2}\left(\xi_0 r_s \cos 2\theta_s - 1\right) = 0, \tag{3.13}$$

admits a unique solution for $\{r_s, \theta_s\}$. The solution to Eq. (3.13) is given by $\cos 2\theta_s = 1/(\xi_0 r_s)$. Eliminating θ_s, from Eq. (3.12), we find an expression for $\alpha(r_s, \xi_0)$,

$$\alpha(r_s, \xi_0) = \frac{r_s\left(1 + \epsilon r_s^2\right)}{(r_s + 1)\sqrt{1 - 1/(\xi_0 r_s)^2}}. \tag{3.14}$$

The dependence of $\alpha(r_s)$ for fixed values of ξ_0 is shown in Fig. 3.5.

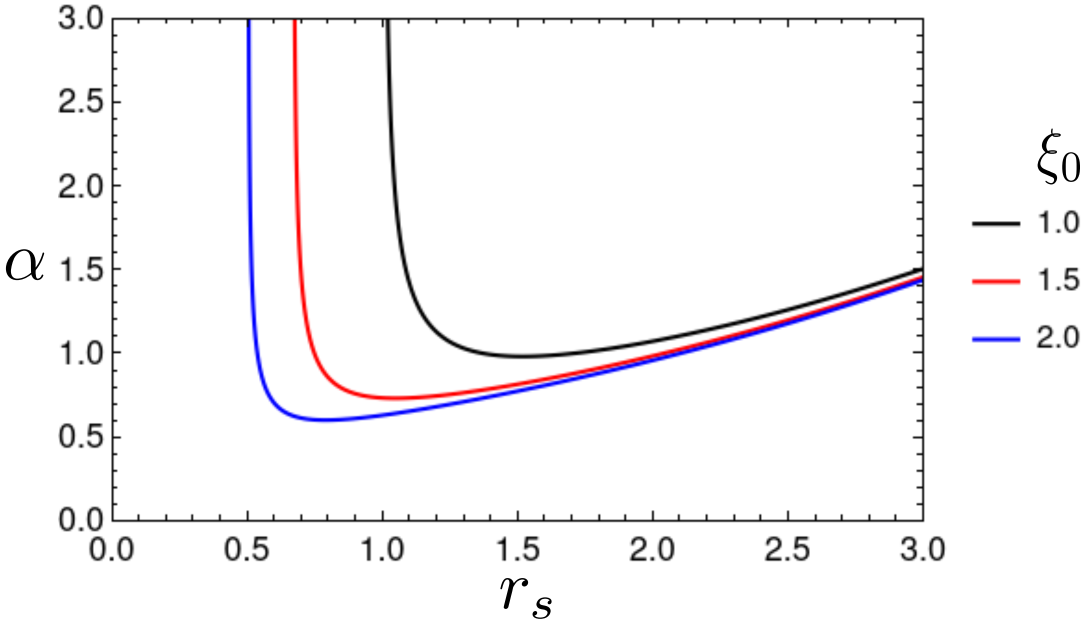

Figure 3.5: Plot of $\alpha(r_s)$ given by Eq. 3.14 for varying values of ξ_0. The turning point corresponds to the value of α with a unique solution for r_s.

Clearly there is a minimum in the function $\alpha(r_s)$. For larger values of α, there are two solutions: the smaller solution corresponds to the saddle point and the larger solution corresponds to the fixed point in the $\{r, \theta\}$ space. Below the minimum, there are no solutions, *i.e.* the saddle-node bifurcation does not occur. At the turning point, there is a unique solution for r_s. Calculating $d\alpha/dr_s = 0$, the resulting quintic equation is:

$$r_s(r_s(\xi_0^2 + \epsilon(r_s(r_s(3 + 2r_s)\xi_0^2 - 3) - 4)) - 1) - 2 = 0, \tag{3.15}$$

which can be solved numerically to determine the value of α for which the unique solution exists for a given ξ_0. By varying ξ_0 and repeating this process, the full phase boundary for region I may be computed. The respective boundary in Fig. 3.1 has been computed in this way. However, a similar approach is not readily available to analytically determined the boundary between regions II and III.

Moreover, this procedure also allows us to determine the value of r_s and θ_s along the boundary separating region I from the rest of the phase diagram. These values correspond to the least elongation r_s^m and the corresponding alignment angle θ_s^m at which the deformable nematics can flow align. The values of r_s^m and θ_s^m obtained as a function of the flow-alignment scale ξ_0 are shown in Fig. 3.6. θ_s^m decreases with

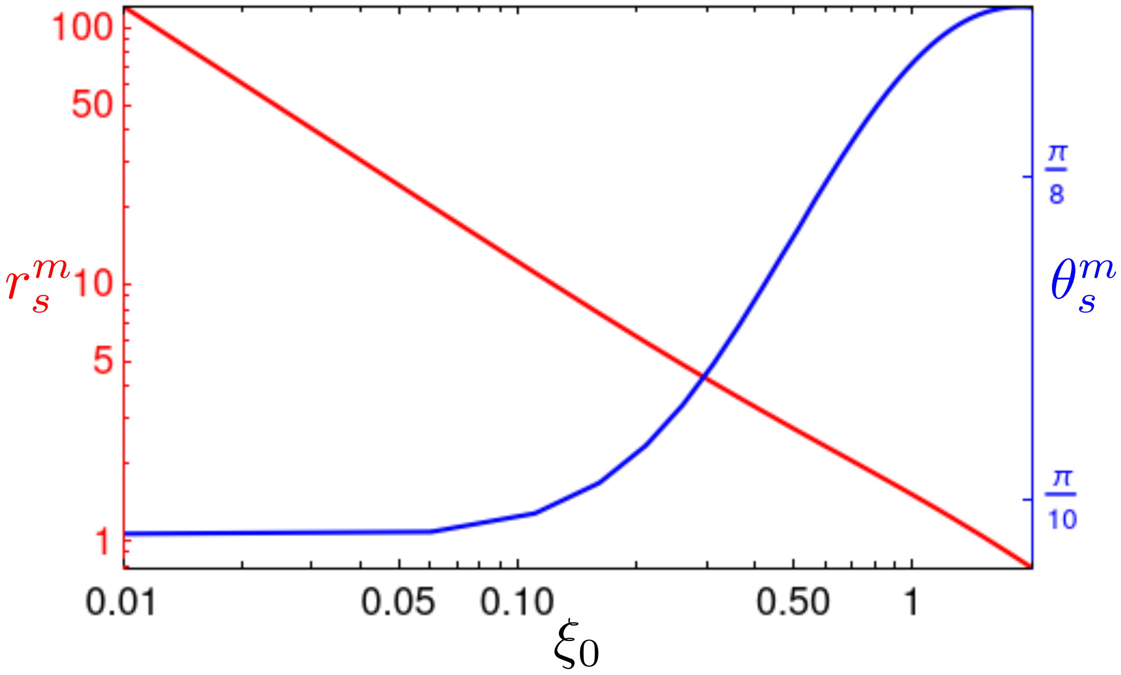

Figure 3.6: Minimum values of the extent of elongation r_s^m (red curve) and the alignment angle θ_s^m (blue curve) of the flow aligning deformable particles as ξ_0 is varied. θ_s^m asymptotes to a constant as $\xi_0 \to 0$ showing that the minimum angle at which a deformable nematic flow-aligns never reaches zero.

decreasing ξ_0. We may arrive at an analytic expression for its asymptotic value by considering the behaviour of Eq. (3.15) as $\xi_0 \to 0$ and $r_s^m \to \infty$, while their product remains finite. This is further motivated by the fact that Fig. 3.6 shows

$r_s^m \sim 1/\xi_0$. Considering the relevant terms of Eq. (3.15) we obtain,

$$\epsilon(r_s^m)^3\left(2\xi_0^2(r_s^m)^2-3\right)=0, \tag{3.16}$$

which has a non-zero solution of $r_s^m(\xi_0\to 0)=\sqrt{3/2}/\xi_0$. Substituting this into Eq. (3.13) gives $\theta_s^m(\xi_0\to 0)=\frac{1}{2}\arccos\sqrt{2/3}$. This result shows that, within this model of deformable nematics, there is a non-zero minimum flow alignment angle. This is physically motivated by the fact that a finite angle is required to keep the nematic elongated enough to sustain the flow alignment and is in contrast to rigid nematics which exhibit a minimum flow alignment angle of zero.

The above analysis of deformable nematics shows that, even in the simplest of systems, the inclusion of deformability into the nematic equations gives rich results that contrast with nematic models of rigid particles.

Shape dependent nematic order

In the previous section, we have implicitly set the nematic order parameter to be constant. Here, we present how this specific limit arises and discuss what happens when the assumption of constant nematic order parameter is relaxed.

We consider a free energy density given by Eq. (2.6)

$$f=\frac{A_Q}{2}\left(S_{eq}^2-\frac{2}{3}Q_{ij}Q_{ji}\right)^2+\frac{K(r)}{2}\left(\partial_k Q_{ij}\right)^2,$$

where $S_{eq}=r/(r+1)$, the value of S that minimises the free energy. $S=0$ for circular particles and $S\to 1$ as the aspect ratio of the deformed particles approaches ∞. We motivated this choice in Sec. 3.2 by arguing that highly elongated particles will tend to align more effectively due to volume exclusion effects in a confluent system. Thus, for the case of Couette flow we obtain the following system of equations:

$$\dot{S}=\frac{8\kappa}{3}\left(S_{eq}^2-S^2\right)S+r\xi_0\alpha\sin 2\theta\left(\frac{4}{9}+\frac{1}{3}S-\frac{3}{2}S^2\right) \tag{3.17}$$

$$\dot{r}=\alpha(r+1)\sin 2\theta-r\left(1+\epsilon r^2\right) \tag{3.18}$$

$$\dot{\theta}=\frac{\alpha}{2}\left(\xi_0\frac{3S+4}{9S}r\cos 2\theta-1\right), \tag{3.19}$$

where we $\kappa=\Gamma A_Q/(\Gamma_r A_r)$ and we have set $r_0=0$. In the previous section, we considered the limit $\Gamma A_Q\ll\xi_0\dot{\gamma}$, which gives a steady-state value of $S=2/3$. Here,

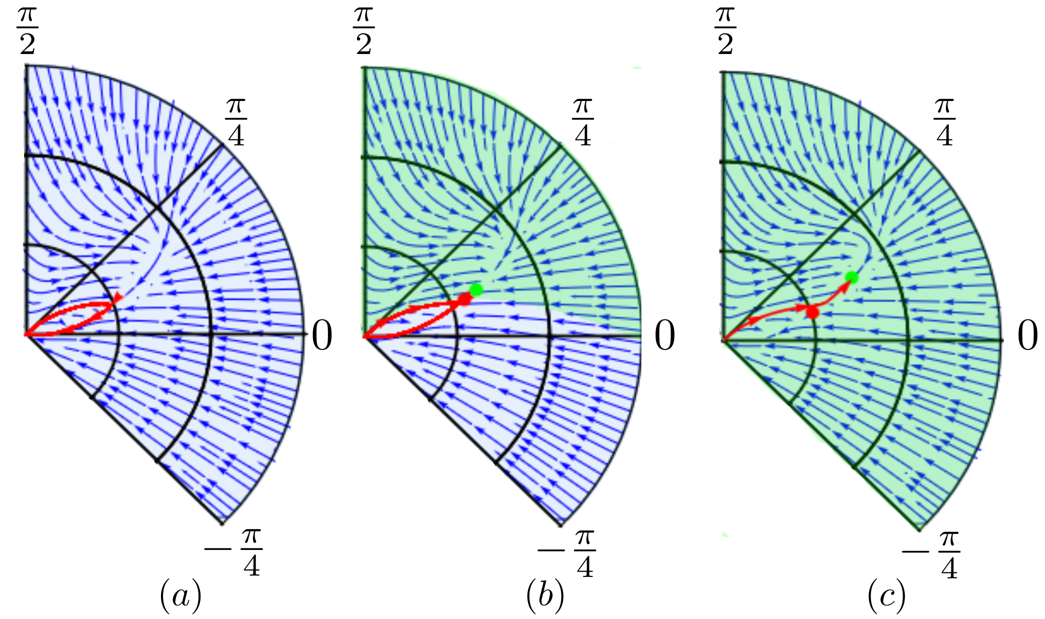

Figure 3.7: Phase space trajectories of the deformable nematics in $\{r, \theta\}$ space in the simplified case of $S = S_{eq}$, thus relaxing the assumption of constant S. Here, $\xi_0 = 1$ and $\alpha = \{0.85, 0.91, 0.95\}$ in $(a) - (c)$ respectively. Red trajectories correspond to the initial conditions $\{0, \pi/4\}$. Steady state $\{\dot{r} = 0, \dot{\theta} = 0\}$ solutions exist as saddle (red) and stable (green) points. Green background labels the basin of attraction for the stable point.

we consider the limit $\Gamma A_Q \gg \xi_0\dot{\gamma}$, where S can be approximated as $S = S_{eq} = r/(r+1)$, reducing the number of ODEs to 2.

We have performed numerical simulations for $S = S_{eq}(r) = r/(r+1)$. We find that the same saddle-node bifurcation exists in the $r - \theta$ space, but, naturally, at different values of the variables and parameters. Fig. 3.7 shows the relevant phase space diagrams. It is clear that the qualitative results remain unchanged. This is because, the main factor behind these results is the shape dependent flow-aligning parameter. A phase diagram similar to Fig. 3.1 may be computed with only quantitative differences.

Given the above discussion, one we would expect that S only plays a quantitative role. This is indeed the case, and we illustrate it by considering the following parameters: $r_0 = 0, \xi_0 = 1, \alpha = 0.8, \epsilon = 0.1$, which places the system in Region I of the phase diagram reported in the manuscript. We set initial conditions $r(0) = 0, \theta(0) = \pi/4, S(0) = 2/3$. The following three cases: $\Gamma A_Q/(\xi_0\dot{\gamma}) \ll 1, \approx 1$ and $\gg 1$ are considered. Fig. 3.8 below shows the plots of $r(t), \theta(t), S(t)$ for the cases $\Gamma A_Q/(\xi_0\dot{\gamma}) = \{0.00125, 1.25, 125\}$ by varying the value of κ. While $S(t)$ is now a dynamical variable, there is only a quantitative change in the plots between the different values of $\Gamma A_Q/(\xi_0\dot{\gamma})$. Unsurprisingly, these quantitative changes also translate to a shift in the phase boundaries of Fig. 3.1. The qualitative form remains the same.

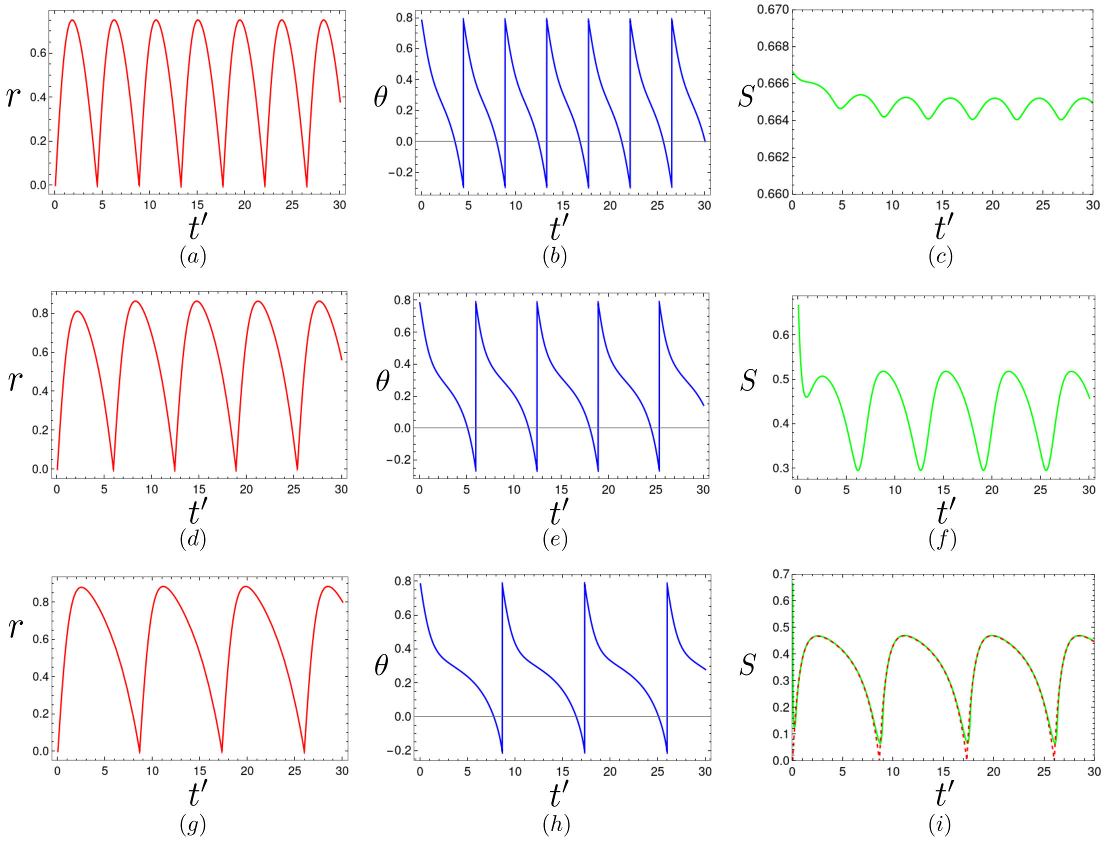

(a) (b) (c)

(d) (e) (f)

(g) (h) (i)

Figure 3.8: Time evolution of r (red), θ (blue) and S (green) for different values of the parameter κ. $(a) - (c)$ $(\Gamma A_Q/(\xi_0\dot{\gamma})) = 0.00125$. The value of S oscillates very closely around 2/3, verifying the validity of the approximation $S = 2/3$ in this limit. $(d) - (f)$ $(\Gamma A_Q/(\xi_0\dot{\gamma})) = 1.25$, which corresponds to an intermediate regime where r attains values of $\mathcal{O}\left(\Gamma A_Q/(\xi_0\dot{\gamma})\right)$. In this case, small quantitative changes can be seen. $(g) - (i)$ $(\Gamma A_Q/(\xi_0\dot{\gamma})) = 125$, corresponding to the limit $(\Gamma A_Q/(\xi_0\dot{\gamma})) \gg 1$. In (i), the red dashed line corresponds to $S_{eq} = r/(r+1)$, verifying the validity of the approximation $S = r/(r+1)$ in this limit which was used to eliminate Eq. (3.17) and simplify the system.

3.3.2 Non-circular particles

In Sec. 3.3.1 we considered deformable nematics with a circular equilibrium shape, $r_0 = 0$. Here, we consider the case of a continuum of particles that inherently have an elongated shape, $r_0 > 0$. The phase-space diagram in this case is qualitatively similar to that of circular particles presented in Fig. 3.1. The three distinct regions I-III remain, but with their phase boundaries shifted to lower α, and lower ξ_0, not necessarily by an equal amount. This shift arises because a flow aligned state can be maintained at lower shear rates as r_0 increases.

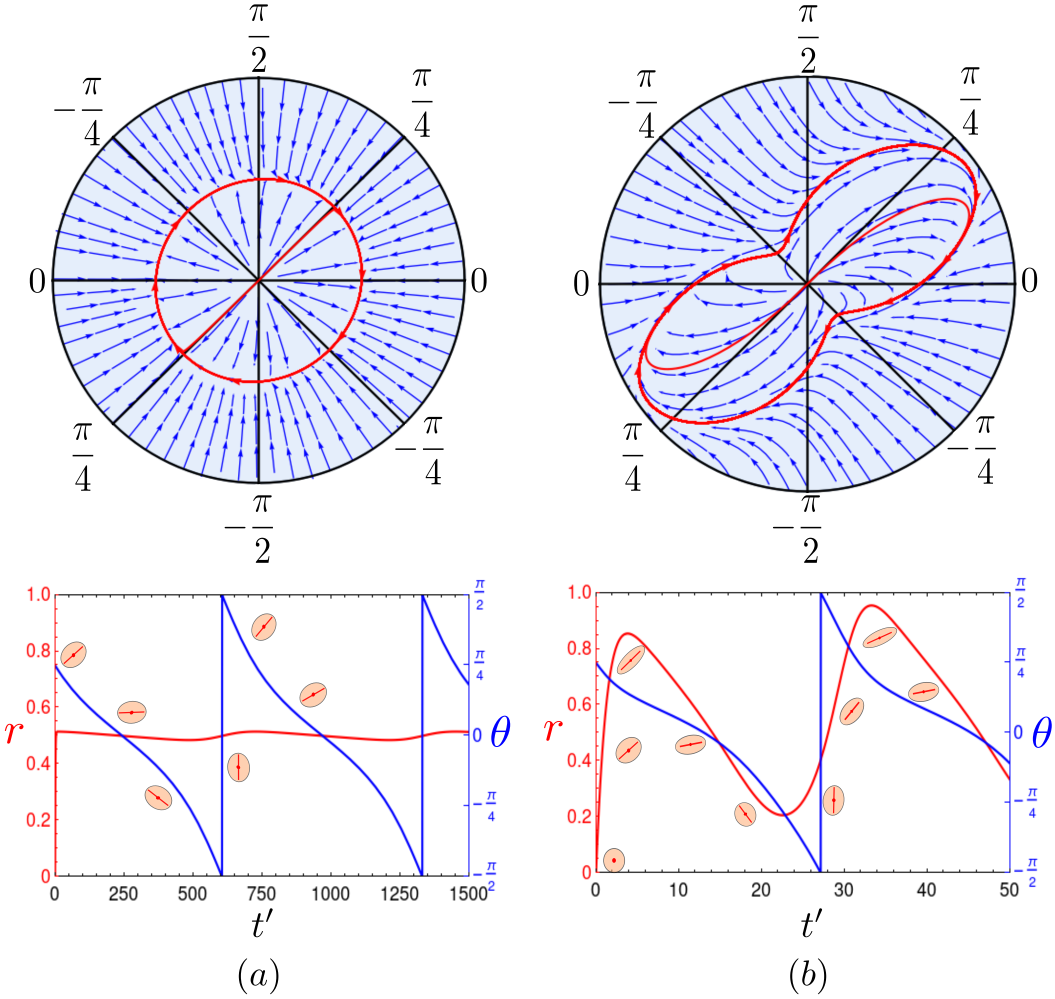

(a) (b)

Figure 3.9: Shape oscillations and tumbling motion of inherently elongated ($r_0 > 0$), deformable nematics: temporal variation of $\{r(t'), \theta(t')\}$ (bottom) and the corresponding phase space trajectories in the $\{r, \theta\}$ space (top). (a) $\alpha = 0.001 \ll 1$, where the limit of rigid nematics is recovered. (b) $0 < \alpha = 0.25 < \alpha_c$ where the variation in particle deformation is more pronounced. Here, $\xi_0 = 1$. The red trajectories correspond to the initial conditions $\{0, \pi/4\}$.

The steady states that the system achieves in regions II and III remain qualitatively the same, but the dynamics in region I becomes richer as full tumbling trajectories become possible. Fig. 3.9 shows the phase space trajectories of a deformable nematic with an equilibrium shape of $r_0 = 1/2$ as α is varied. For $\alpha \ll 1$, the strain rate is too weak to deform the particles appreciably, but the vorticity component drives the rotation. Thus, the shape oscillations observed in region I remain, but with a small amplitude as shown in Fig. 3.9 (*a*) (bottom). Since the vorticity drives the particles to rotate through an angle 2π, the limit cycle in phase space closely follows a circle of radius $r = r_0$ as shown in Fig. 3.9 (*a*) (top). The dynamics observed in this limit corresponds to the dynamics of rigid nematics with an effective Leslie flow-aligning parameter $\xi_0 r_0$.

As α is increased, the extent of elongation (for $\theta > 0$), and that of contraction (for $\theta < 0$) also increase. Though the tumbling motion persists, the trajectory in phase space is deformed into a dumbbell (see Fig. 3.9 (*b*)). At a critical value $\alpha_c(r_0)$, the trajectory reaches the origin of phase space, and the particles re-extend along $\theta = \pi/4$ giving qualitatively the same trajectories as for nematic particles with $r_0 = 0$.

3.4 Poiseuille flow

3.4.1 Imposed flow

Equations of motion

In this section, we consider a continuum of deformable nematics confined between two parallel plates separated by a distance L, and subjected to a Poiseuille flow. The flow is generated by applying a pressure gradient G along the length of the channel. The velocity field is given by $u_x(y) = \frac{G}{2\eta} y(L - y)$, where η is the viscosity of the fluid, with a position-dependent shear rate $\dot{\gamma}(y)$. The governing equations for the evolution of the elongation and the orientation of the principal axis of the deformable particles are

$$\dot{r} = \alpha_p(1 - 2y')(r + 1)\sin 2\theta - r(1 + \epsilon r^2), \tag{3.20}$$

$$\dot{\theta} = \frac{\alpha_p}{2}(1 - 2y')\left(\xi_0 r \cos 2\theta - 1\right) + \beta^2 \frac{r^2}{(r+1)^2} \partial^2_{y'}\theta, \tag{3.21}$$

where $y' = y/L \in [0, 1]$ is the dimensionless spatial variable and $\alpha_p = GL/(2\eta\Gamma_r A_r)$ is the Péclet number. The last term in Eq. (3.21) accounts for Frank-Oseen elasticity arising from gradients in θ. The functional form of the elastic constant, $K(r) = K_0 r^2/(r+1)^2$ is chosen as an approximation to capture the dependence on the shape of the particles [100]. The dimensionless parameter $\beta^2 = \Gamma K_0/(\Gamma_r A_r L^2)$ controls the strength of nematic elasticity. For simplicity, and to keep the independent simulation parameters to a tractable number, we omitted elastic terms emerging from $K(r)$ in Eqs. (3.20) and (3.21). Their inclusion has no qualitative effect on the results (see Appendix B.1.1).

Simulations were run with $\alpha_p = 1.8, \xi_0 = 1, \epsilon = 0.1$. The value of β was varied by changing K_0. Neumann boundary conditions were applied for the director field at the walls. Initial conditions were $r(y', 0) = 0.1$ and $\theta(y', 0) = \pm\pi/4$ for $y' \lesseqgtr 1/2$ respectively. The analysis that follows assumes that the Poiseuille flow is imposed, *i.e.* it is unaffected by elastic stresses, and thus corresponds to the limit of large Ericksen number. We will explore the consequences of varying the Ericksen number in the next section.

Resulting dynamics

In Fig. 3.10 we plot the spatio-temporal evolution of the elongation and orientation of the deformable particles for $\beta = 0$ as a kymograph. The variation in the shear rate across the channel leads to particles near the walls aligning as in Region III, while particles around the centre of the channel orbit as in Region I with periods that depend on the local shear rate. Thus, (i) a wall-bound band consisting of relatively more elongated particles and (ii) a central band with relatively less elongated particles but with a spatio-temporally evolving pattern form inside the channel. Rigid, tumbling nematic liquid crystals can exhibit banding due to strong anchoring boundary conditions on the walls [101, 102], but, here the spatial segregation into central and wall-bound bands arises purely from the deformability of the particles and its coupling to the orientational dynamics.

The steady state of the system is not unique for $\beta \neq 0$, but depends on the simulation protocol. As an example, in Fig. 3.11 $(a)-(b)$ we plot the spatio-temporal evolution of the particles' elongation and orientation when β is increased from zero

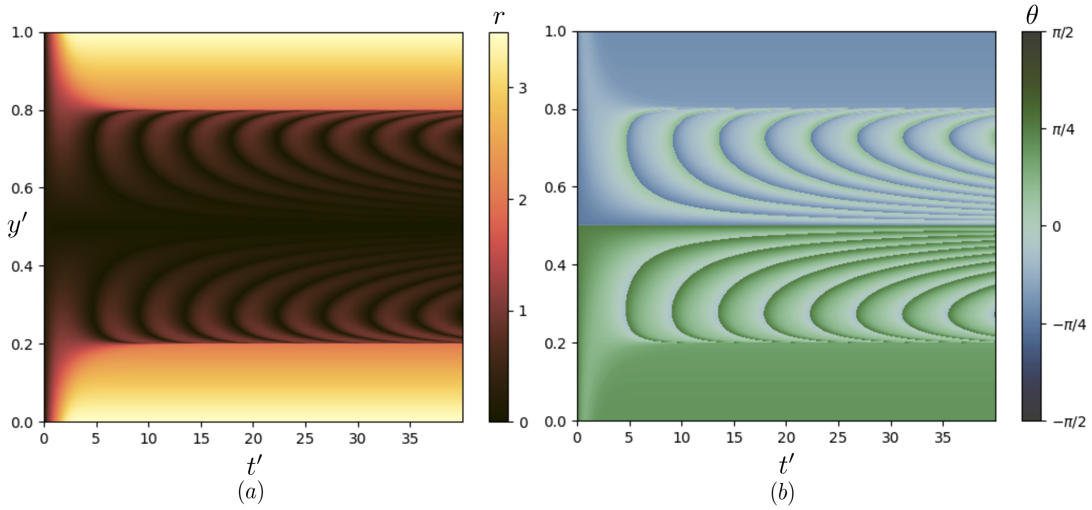

(a) (b)

Figure 3.10: Kymographs showing spatio-temporal evolution of (a) $r(y', t')$, and (b) $\theta(y', t')$ of deformable nematics in a Poiseuille flow for $\beta = 0$.

to 0.3 in steps of 0.1 every 40 time steps. Results of the reverse protocol when β is systematically decreased are shown in Fig. 3.11 $(c) - (d)$. In both cases the initial conditions are $(r = 0.1,\ \theta = \pm\pi/4)$. The figures show qualitative differences in the dynamics for a given value of β. In particular, in the second case (Fig. 3.11 $(c) - (d)$), this choice of initial conditions helps to stabilise a flow aligning state in the entire channel for large β. For intermediate values of β, we note that the wall-bound layers which were previously at a steady, flow-aligned state, may be disrupted and begin to also exhibit shape oscillations. However, for both the low and high β regimes, they retain their steady state and, in the latter case, prevent the oscillations of the centre layers altogether.

We may then quantify the state of the system as a function of the Péclet number, α_p, and the nematic elasticity, β, for the initial conditions $(r = 0.1,\ \theta = \pm\pi/4)$. In the phase plot in Fig. 3.12 the color represents l_c/L, the width of the central band as a fraction of the channel width: regions A, B and C correspond to $l_c/L \approx 1, 0$ and $0 < l_c/L < 1$ respectively. When α_p is small, even particles near the wall cannot reach a flow-aligned steady state, and hence the central band of shape oscillating particles occupies the entire channel ($l_c = L$) irrespective of the value of β (Region A). With an increase in α_p, and at $\beta \lesssim 0.2$ there is flow-alignment near the walls, decreasing the width of the central band (Region C). For larger β the

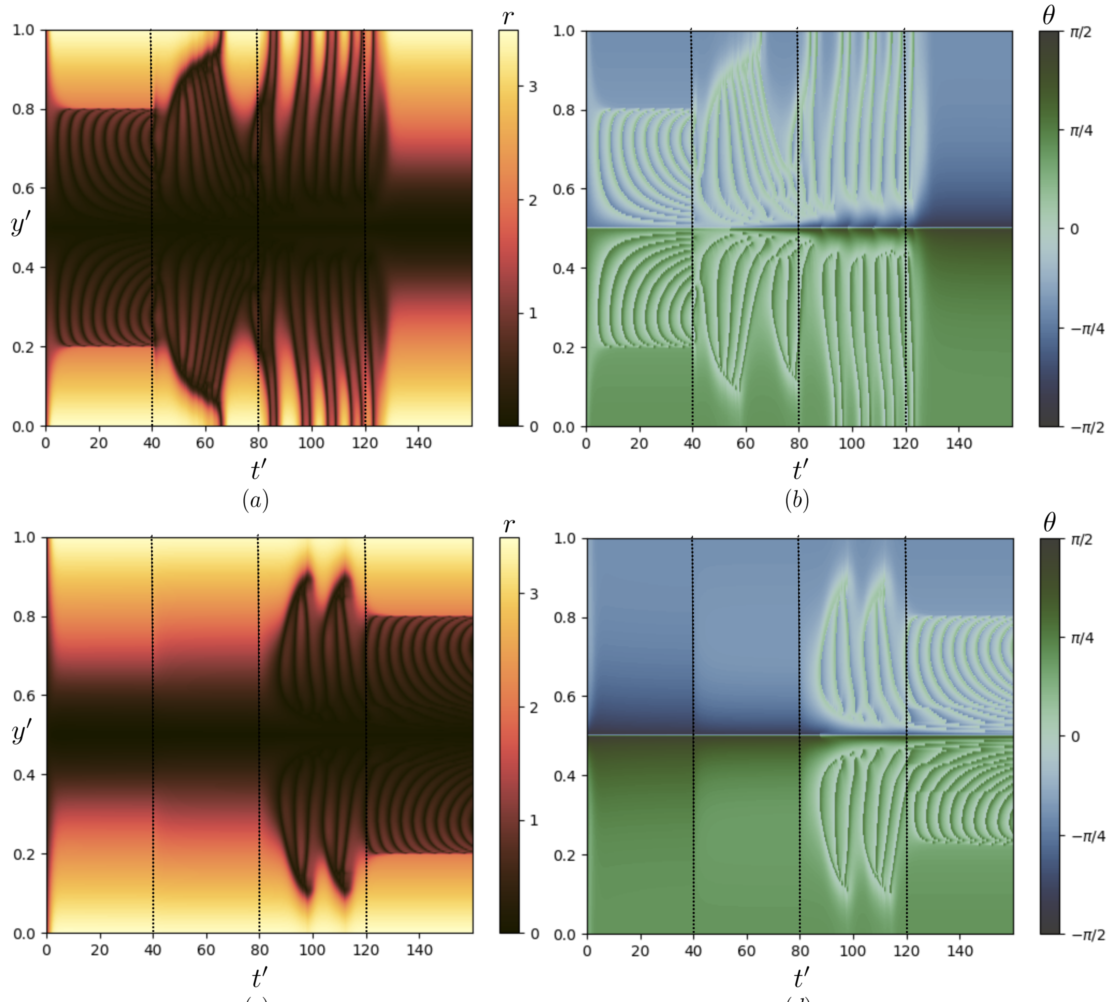

(a) (b)

(c) (d)

Figure 3.11: Kymographs of $((a),(c))$ $r(y',t')$ and $((b),(d))$ the angle of orientation $\theta(y',t')$. The simulation protocol is varying β in the range 0 and 0.3 in increments of 0.1 every 40 units of time in $(a)-(b)$. $(c)-(d)$ correspond to the backwards scenario where β is reduced from 0.3 to 0.

system is not able to overcome the nematic initial conditions and all nematogens remain flow-aligned (Region B). However, Region B disappears for random initial conditions. We discuss the steady-state solutions in this region further below.

While Fig. 3.11 illustrates the spatio-temporal evolution, $r(y',t')$ as β is varied in a stepwise fashion, we may form a more complete picture of the consequences of the nematic elasticity by considering both the elongation and orientation angle. Fig. 3.13, shows kymographs of r and θ for $\alpha_p = 1.8$ and $\beta = 0.05$ over a longer simulation period. Inclusion of nematic elasticity ($\beta \neq 0$) results in further development of the spatial coherence in the microstructure of deformable particles.

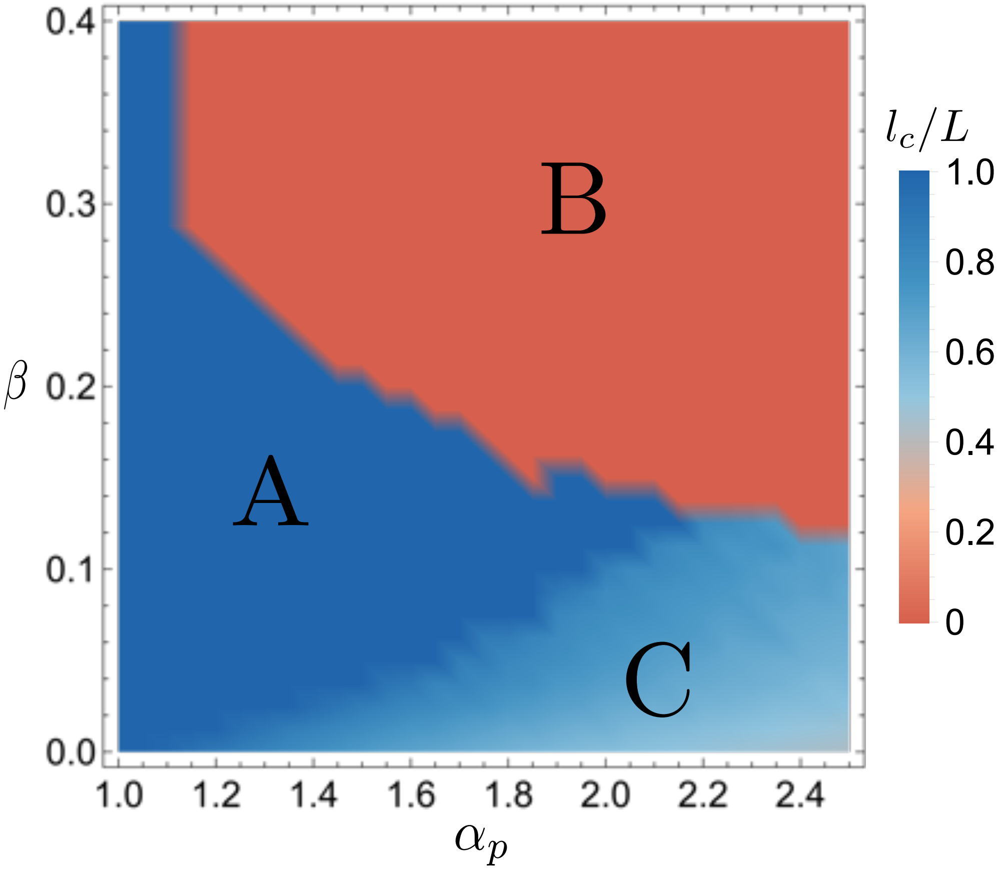

Figure 3.12: Phase diagram measuring the fraction of the central band, l_c/L (defined as the portion of the system exhibiting shape oscillations) for initial conditions $r = 0.1,\ \theta = \pm\pi/4$.

The dynamics continue to be time dependent with the central band expanding and contracting continuously, in addition to the tumbling dynamics of particles in the central band observed at $\beta = 0$. Note that the features associated with the temporal evolution of the central band seen in Fig. 3.13 are similar to that in Fig. 3.11 where β is changed stepwise.

Finally, we consider the case where the system is deep in region B of Fig. 3.12, where a steady state is achieved in more detail. Fig. 3.14 shows the spatial variation of the steady-state solutions, $r_s(y')$ and $\theta_s(y')$ for $\alpha_p = 2, \beta = 0.25$. At the wall, $\theta_s(y')$ reaches a constant value to satisfy the boundary condition. Near the centre of the channel, the symmetry $\theta(y') = -\theta(y' + 1/2)$ enforces that $\theta_s \to \pm\pi/2$, resulting in a bend-like solution. These solutions may be obtained by solving the differential-

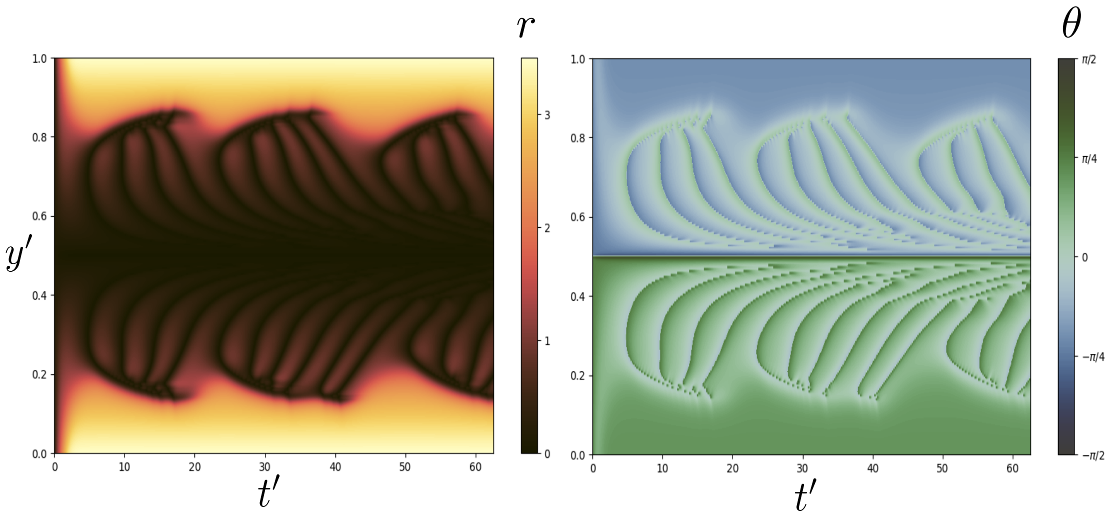

(a) (b)

Figure 3.13: Kymographs of (a) $r(y',t')$ and (b) $\theta(y',t')$ in a Poiseuille flow for $\alpha_p = 1.8, \beta = 0.05$.

algebraic system corresponding to $\dot{r} = 0, \dot{\theta} = 0$ in Eqs. (3.20) and (3.21).

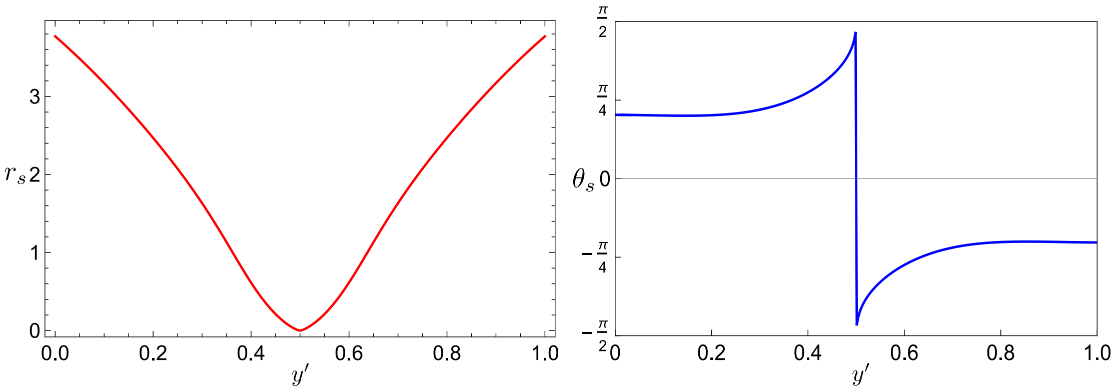

Figure 3.14: Steady state solutions, $r_s(y')$ and $\theta_s(y')$ for a system of deformable nematics with $\alpha_p = 2$, $\beta = 0.25$. The apparent discontinuity at $y' = 1/2$ in $\theta_s(y')$ is due to the nematic nature of the particles which automatically respects the equivalence of $\theta = \pm\pi/2$.

In the above analysis, we have assumed an imposed Poiseuille flow in order to present a minimal model, which includes the most relevant physics in a way that is amenable to semi-analytical and relatively simple numerical analysis. In the next section, we consider the more general case where we use the Q tensor formulation and keep the flow field as a dynamical variable which we solve for, including all the components of the stress tensor in the Navier-Stokes equations. It is also noteworthy that boundary conditions may play a significant role in the ultimate dynamics of these systems. Preliminary simulations of anchoring boundary conditions for different chosen values of the anchoring angle have shown qualitatively different results. We do not include these here and leave the analysis of boundary conditions for future work.

3.4.2 Full nematohydrodynamics

In this section, we perform simulations using a hybrid lattice Boltzmann method to solve the full Beris-Edwards equation for the **Q** tensor, the Navier-Stokes equations for the flow field **u** and the time evolution of the shape variable, r, including the elastic backflow and functional derivative terms, which we had neglected in the previous section. We therefore numerically solve the system of Eqs. (2.11), (2.12), (2.14) and (3.9) in a channel of width L, with translational invariance along the $\hat{x}$ direction, Neumann boundary conditions for r and **Q** and no-slip boundary conditions for **u** at the walls. A constant pressure gradient G is applied along the flow direction.

The following parameters are chosen for the simulations: lattice grid size $\Delta x = 1$ and time step size $\Delta t = 1$, $L = 200, \xi_0 = 1, G = 1.5 \times 10^{-5}, \eta = 2/3, \Gamma_r = 0.05, A_r = 0.025, A_r^* = 0.0025, A_Q = 0.4, S_{eq} = 2/3, \rho = 1$. The parameters are chosen to ensure that the dimensionless parameters $\alpha_p = 1.8$ and $\beta = 0.05$ are kept constant. Initial conditions were $r(y, 0) = 0.1$ and $\theta(y, 0) = \pm\pi/4$ for $y \lesseqgtr 100$ respectively, while the velocity field is initialised as a Poiseuille flow given by $u_x(y, 0) = \dfrac{G}{2\eta} y(L - 2y)$.

To quantify and compare the elastic and viscous stresses, we define the Ericksen number $Er = \dfrac{\eta u_m L}{K_0}$ the ratio of viscous to elastic stresses. Here u_m is the mean velocity across the channel width, and is equal to $GL^2/12\eta$ for a pure parabolic flow.

We consider the following two cases:

1. $\{\Gamma, K_0\} = \{12.625, 0.01\}$ that gives $Er = 1000$, thus yielding viscous stresses much greater than elastic stresses. The dynamics obtained are similar to the results presented in the Sec. 3.4.1. The results are illustrated using kymographs of the degree of elongation $r(y', t')$ and the angle of orientation $\theta(y', t')$ in Fig. 3.15($(a) - (b)$).

2. $\{\Gamma, K_0\} = \{2.525, 0.05\}$ that gives $Er = 200$, an intermediate value of the Ericksen number. In this case, elastic stresses become comparatively larger and the resulting velocity profile exhibits small deviations from the parabolic flow. The results are illustrated using kymographs of the degree of elongation $r(y', t')$ and the angle of orientation $\theta(y', t')$ in Fig. 3.15($(c) - (d)$). There are only quantitative changes to the results such as the oscillation period and the extent of elongation even at this value of Er. Namely the observations such as the existence of non-periodic shape oscillations across the channel and the enhanced flow-alignment for more elongated particles near the walls remain.

It is evident that the fully coupled system qualitatively reproduces the results presented in the previous section, verifying the validity of the simplified model we had assumed. Moreover this analysis gives us an estimate of the range of Er for which the assumption of imposed flow is valid. The results for Poiseuille flow show how more complex solutions emerge due to shape deformations and nematic elasticity. In both cases, the model of deformable nematics gives results that contrast with nematic models of rigid particles.

3.5 Summary

In this chapter, we developed a minimal continuum model of deformable nematics through the introduction of a dynamical equation of motion for the aspect ratio of the particles, which we approximated as ellipses. Motivated by the recent interest in the significance of particle shape in biological physics and soft matter more broadly, we studied how a minimal coupling of shape and orientation qualitatively alters the dynamics of systems of deformable particles. This was achieved by coupling the particle shape to the nemato-hydrodynamic equations through both thermodynamic and hydrodynamic contributions. In the case of the former we argued that, in a confluent system, highly elongated particles will tend to align more effectively due to volume exclusion effects, thus increasing nematic order. For the latter, we introduced a shape dependence on the competition between flow-aligning and vorticity.

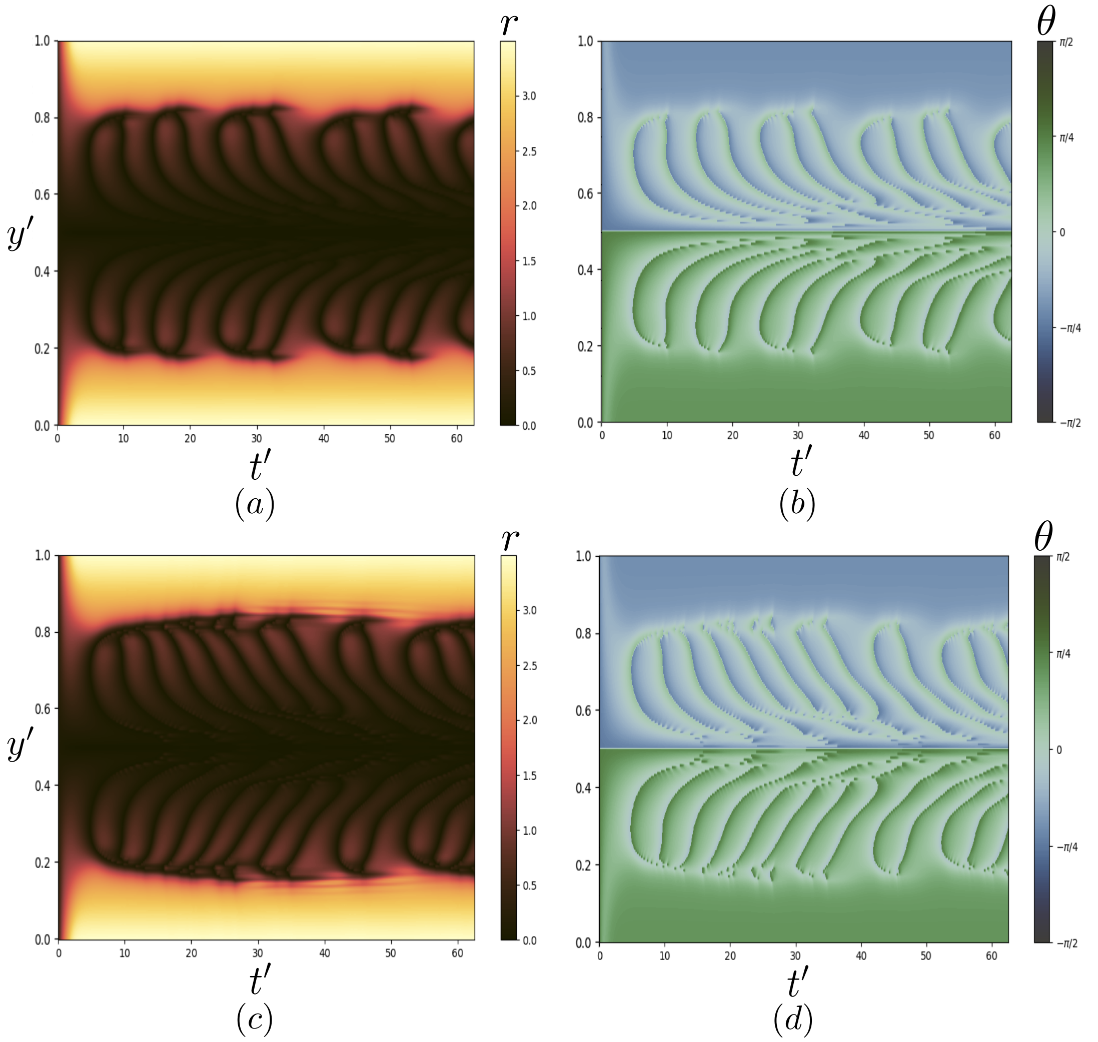

(a) (b) (c) (d)

Figure 3.15: Kymographs of $r(y', t')$ and $\theta(y', t')$, obtained using the full Navier-Stokes model with $\mathbf{Q}$ tensor formalism and solved using the hybrid lattice Boltzmann method. Simulations are run for $\alpha_p = 1.8, \beta = 0.05$ and for $(a) - (b)$ $Er = 1000$, and $(c) - (d)$ $Er = 200$, respectively.

To understand the consequences of our extension to the nemato-hydrodynamic model, we first analysed channels with imposed flows and a constant nematic order. The coupling of particle shape and orientational dynamics lead to novel dynamics that could not be captured by a model of rigid nematics. In a simple shear flow, we found that the system may settle in one of two distinct states of periodic shape oscillations, or a constant steady state of finite elongation and flow-aligned orientation, depending on the applied shear rate. This was found to be linked to the shape-orientational coupling introduced in the model. In a Poiseuille flow, the spatially dependent shear rate and the nematic elasticity created a co-existence of regions that displayed shape oscillations and flow alignment. In both cases, our model gives results that contrast with nematic models of rigid particles.

We also considered the presence of additional elastic terms and removed the assumptions of infinite Ericksen number and constant magnitude of the nematic order, with no qualitative differences seen. Thus, the simple model proposed in this chapter is a useful way of analysing the dynamics and rheology of deformable nematics. The results here also have biological reference; many eukaryotic cells are deformable and extension of the current analysis for cellular layers and tissues would be interesting. Therefore, in the next chapter, we consider the case of active deformable nematics, which extends the active nematic models which are based on rigid, elongated particles.

4

Active nematics with deformable particles

In this chapter we apply the model of deformable nematics presented in Chapter 3 to a bulk active system, such as a confluent cell monolayer. We first discuss how the mechanism for deformable particle re-orientation discussed in Chapter 3 behaves in a system dominated by active dipolar forces such as the ones introduced in Eq. (2.19). We then perform a linear stability analysis on the nematohydrodynamic equations for deformable, circular cells. We show that a threshold activity is required to generate sufficient active stress to overcome an elastic barrier to deforming their shape in order to drive tissue-scale flows. Above this threshold the system enters an active turbulent state. Further, using numerical simulations, we illustrate the novel dynamics of an active turbulent system of deformable nematics, akin to, but qualitatively different from the active turbulence in rigid nematics discussed in Chapter 2.5.1. We find a dynamical steady-state with regions of elongated cells and strong flows coexisting with quiescent regions of isotropic cells. Finally, we discuss the robust statistical features and characteristic length-scales that emerge. The results in this chapter demonstrate that a minimal model that introduces deformability in the active nematic theory can lead to novel dynamics that could not be previously captured under the assumption of rigid particles, while still reproducing important results of the original models such as the existence of motile topological defects, nematic domains, and chaotic flows. The model we present here allows for several testable predictions, such as the measurement of the average aspect ratio of cells within a monolayer as their activity is varied, the elongation of cells around topological defects, and the asymmetric stresses that result from this effect.

4.1 Introduction

In Chapter 2, we discussed how the theories of rigid active nematics have been successful in describing some of the qualitative features seen in living systems. Such systems, such as motile cells constantly consume chemical energy from their surroundings to create active forces which drive mechanical work. This was incorporated mathematically by an additional contribution to the stress tensor.

In this chapter, we explore how the dynamics of a bulk, active system, such as a confluent cell monolayer, described by the active nematohydrodynamic Eqs. 2.11, 2.12, 2.14 presented in Chapters 2.4 and 2.5 behaves when relaxing the assumption that the cells are rigid. The assumption of rigid particles in active nematic models may be a reasonable description for systems consisting of rod-shaped cells such as fibroblasts [38] or *Escherichia coli* [103]. However, many particles, such as epithelial cells, e.g. Madin-Darby Canine Kidney (MDCK), can undergo large shape changes and thus their aspect ratio can vary significantly when subjected to active forces [10, 11, 104]. The analysis in this chapter is motivated by the observation of active turbulence in confluent cell layers where cells can be deformed such as the MDCK cell line [24, 43].

In Chapter 3 we described some of the consequences of large variations in the shape, and its coupling back to the orientational dynamics, of particles in the case of an externally driven, passive system. In the case of an active system, the dynamics become richer, with striking qualitative differences to that of rigid active nematics. For example, recent works have shown that intercellular stresses in cell monolayers are enhanced by cell deformation, creating a positive feedback loop that affects the collective behaviour of the layer [105], an effect that we successfully capture here as well. In this chapter, we will focus on the effects of the variation of the shape of particles on the dynamics of a system of confluent cells where active forces play a dominant role.

This chapter is structured as follows: In Sec. 4.2, discuss the re-orientation mechanism introduced in Chapter 3 in the context of flows generated by active forces. In Sec. 4.3, we consider an active system of inherently circular, nematic particles and perform a linear stability analysis of their shape, revealing the existence of an activity threshold required to maintain elongation. In Sec. 4.4, we follow this up by numerically simulating a system of active, deformable nematics where the activity is sufficient to transition into active turbulence. In this thesis, we define active turbulence by the existence of long-lived (on the order of the simulation time), motile topological defects. We will discuss the relevant statistical quantities and highlight the qualitative and quantitative differences between our model and rigid active nematics. Finally, in Sec. 4.5 we provide a summary of the results, the limitations of our model and future pathways.

4.2 Re-orientation mechanism in active flows

In Chapter 2, we discussed how forces arising from the dipolar active stress give rise to flows that exhibit shear. When a deformable nematic particle is subjected to such flows, its aspect ratio and orientation may change due to both flow-driven effects, such as extension/compression and thermodynamic effects such as its relaxation towards the free energy minimum associated with its shape, as in Fig. 4.1.

Phase space description

In our model of active nematics, particles generate pure shear flows along their principal axes, with the direction reversed between contractile/extensile nematics. To illustrate the re-orientation mechanism arising due to the deformable nature of the active particles, we first consider the idealised case of a *passive* particle subjected to a pure shear flow at an angle to their long axis. In Chapter 3, we have considered the case of re-orientation due to a shear flow, which included a vorticity component. Here, we solve the coupled time evolution of particle orientation $\mathbf{n}$, defined to be at

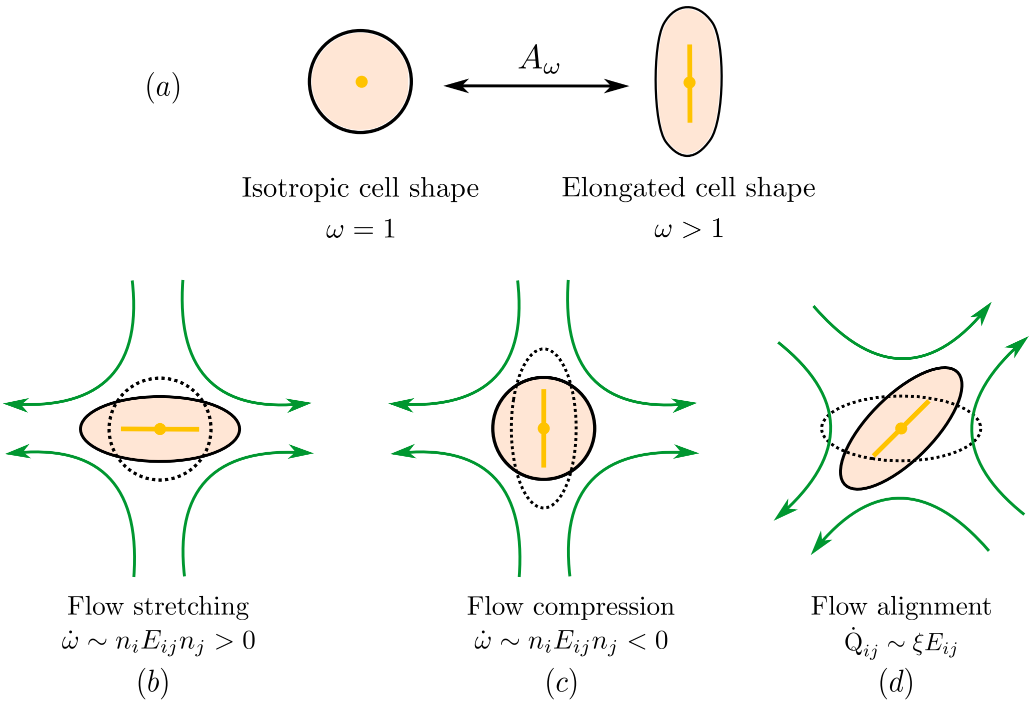

Figure 4.1: Particle deformations driven by (a) free energy minimisation towards an equilibrium shape, (b) flow stretching, (c) flow compression, and re-orientation due to (d) flow alignment. In $(b)-(d)$, dotted lines represent the shape and orientation of particles at a previous time.

an angle θ from the compressional axis of the flow, and aspect ratio ω. We therefore solve Eq. (2.14) for the director field in the Ericksen-Leslie limit [55] for a finite flow-aligning parameter, coupled to Eq. (3.6) with $\Gamma_\omega = 0$ for simplicity.

Depending on the position in the $\{\theta, \omega\}$ phase space, there are two distinct re-orientation mechanisms: If the angle θ between the compressional flow axis and particle orientation is sufficiently large, particles undergo rotation where their shape changes over time, but in the process, the particles remain anisotropic as their orientation rotates until it aligns with the extensional flow axis (red trajectory in Fig. 4.2). This is akin to the re-orientation mechanism one would see in a traditional model of rigid nematic particles, discussed in Chapter 2. If θ is small, however, the elongated particles have to rotate through a larger angle to align with the extensional axis of the flow. While doing so, they get squeezed by the compressional flow until they become isotropic, $\omega = 1$. Subsequently, they re-elongate towards the extensional flow axis since it is the principal axis of deformation $(Q_{ij} \sim E_{ij})$ as discussed in

Chapter 3, and their aspect ratio increases again (blue trajectory in Fig. 4.2).

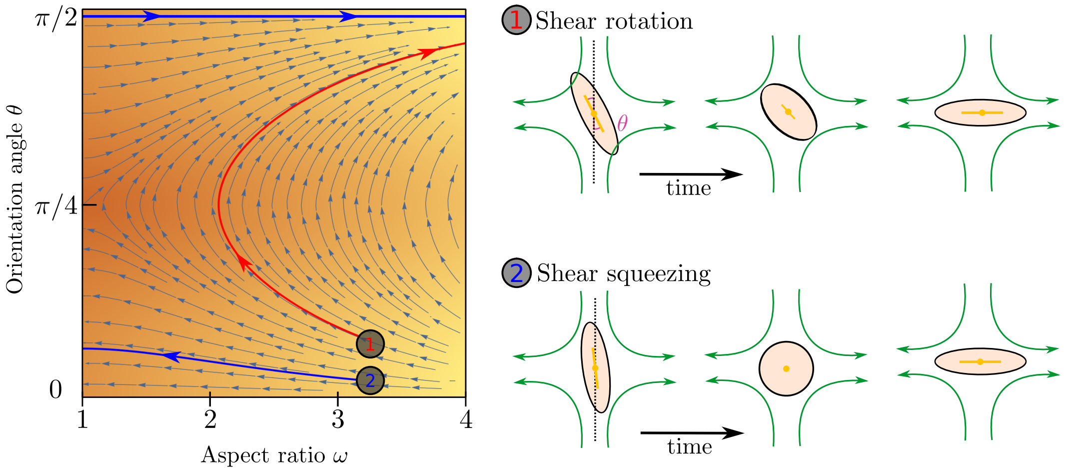

Figure 4.2: Left: Phase space trajectories of the evolution of ω subject to a compressional flow at an angle θ to the director. Red trajectory represents a re-orientation of particles towards the extensional axis, while maintaining an anisotropic shape ($\omega > 1$) (shear rotation). Blue trajectory represents re-orientation due to particles being squeezed to an isotropic shape ($\omega = 1$), and subsequently re-elongating along the extensional axis (shear squeezing). Right: Rotation and squeezing of a particle as described by the red/blue trajectories.

While we consider an idealised case of pure shear flow in the above example, the re-orientation mechanisms illustrated are general and are observed in our numerical simulations of active turbulent systems. In Chapter 3, we investigated how deformability plays a role in flows with both a strain rate and vorticity component, potentially resulting in oscillations of both the orientation and shape of particles, in this case, there is no vorticity component to drive rotation; the particles eventually align with the extensional axis, but through two possible trajectories.

4.3 Linear stability analysis

Before proceeding to the discussion of active turbulence in a model of deformable nematics, we first investigate the behaviour of an active system consisting of nearly circular particles. The analysis of the stability of the underformed particle shape allows us to develop an insight on the competition between the extensile active forces that drive elongation and the free energy cost of deforming particles from their equilibrium shape. Hence, we are now solving Eqs. (2.11), (2.12) with the inclusion of the active stress tensor, given by Eq. (2.21), coupled to the evolution of the orientational tensor and aspect ratio, Eqs. 2.14 and (3.6), respectively. We restate these equations here for easy reference:

$$\partial_i u_i = 0, \tag{4.1}$$

$$\rho \left(\partial_t + u_k \partial_k\right) u_i = \partial_j \Pi_{ij}, \tag{4.2}$$

$$\left(\partial_t + u_k \partial_k\right) Q_{ij} - \mathcal{W}_{ij} = \Gamma H_{ij}, \tag{4.3}$$

$$\left(\partial_t + u_k \partial_k\right) \omega = 2\omega E_{\parallel} - \Gamma_\omega \frac{\delta \mathcal{F}}{\delta \omega}, \tag{4.4}$$

where $H_{ij} = -\delta\mathcal{F}/\delta Q_{ij} + (\delta_{ij}/3)\delta\mathcal{F}/\delta Q_{kk}$ is the molecular field associated with a free energy density,

$$f = A_Q \left(S_{eq}^2 - \frac{2\mathrm{Tr}(\mathbf{Q}^2)}{3} \right)^2 + \frac{K_Q}{2} \left(\nabla \mathbf{Q}\right)^2 + A_\omega \frac{1}{2}(\omega - \omega_0)^2 + A_\omega^\star \frac{1}{4}(\omega - \omega_0)^4, \tag{4.5}$$

where $S_{eq} = (\omega - 1)/\omega$ and the remaining terms of the generalised co-rotational derivative $\mathcal{W}_{ij}$ read as

$$\mathcal{W}_{ij} = \left(\xi(\omega) E_{ik} + \Omega_{ik}\right) \tilde{Q}_{kj} + \tilde{Q}_{ik} \left(\xi(\omega) E_{kj} - \Omega_{kj}\right) - 2\xi(\omega) \tilde{Q}_{ij} Q_{kl} W_{lk}, \tag{4.6}$$

and the total stress tensor, Π_{ij}, is given by

$$\begin{aligned} \Pi_{ij} =& 2\eta E_{ij} - p\delta_{ij} - \xi(\omega)[H_{ik}\tilde{Q}_{kj} + \tilde{Q}_{ik}H_{kj} - 2\tilde{Q}_{ij}(Q_{kl}H_{lk})] \\ &+ Q_{ik}H_{kj} - H_{ik}Q_{kj} - \partial_i Q_{kl} \left(\frac{\partial f}{\partial_j Q_{lk}} \right) - \zeta Q_{ij}. \end{aligned} \tag{4.7}$$

Here, we consider an extensile system $\zeta > 0$ of inherently circular particles $\omega_0 = 1$. We perform a stability analysis around a quiescent isotropic system by adding a small perturbation to the aspect ratio of particles, $\omega = 1 + \delta\omega$. The shape perturbation $\delta\omega \sim \exp\{(i\mathbf{q}\cdot\mathbf{r} + \lambda t)\}$ is applied along a wavevector $\mathbf{q} = q\,(\cos\theta, \sin\theta, 0)$ with a growth rate λ which will characterise the stability of the circular particles and we assume particles deform along their long axis.

It will be convenient to work in Fourier space for the following calculations. To that end, we define the inverse Fourier transform for a fluctuating field f' as

$$f'(\mathbf{r}, t) = \int d\lambda dq \tilde{f}(\mathbf{q}, \lambda) e^{i\mathbf{q}\cdot\mathbf{r} + \lambda t}, \tag{4.8}$$

where $\tilde{f}(\mathbf{q},\lambda)$ is the associated Fourier transform of the field. The time evolution equation for the tensorial order parameter $\mathbf{Q}$, Eq. (2.14), is eliminated by setting $\mathbf{n} = \hat{x}$ and $S = (\omega - 1)/\omega$, its equilibrium value that minimises the bulk free energy, given by Eq. (4.5). The relevant equations of motion to first order in the perturbed fields (the aspect ratio and flow fields) are then:

$$\partial_t \omega' = 2E'_{\parallel} - \Gamma_\omega A_\omega \omega' + \frac{3}{2}\Gamma_\omega K_Q \nabla^2 \omega', \tag{4.9}$$

$$\rho \partial_t u'_i = \partial_j \left(2\eta E'_{ij} - p'\delta_{ij} - \frac{3}{2}\zeta\omega'(n_i n_j - \frac{1}{3}\delta_{ij}) \right). \tag{4.10}$$

In Fourier space, incompressibility reads

$$q_j \tilde{u}_j = 0 \Rightarrow \tilde{u}_x = -\frac{\sin\theta}{\cos\theta}\tilde{u}_y. \tag{4.11}$$

Hence, Eq. (4.10) in Fourier space reads:

$$\rho\lambda\tilde{u}_i = \eta \left(-q_i \underbrace{q_j \tilde{u}_j}_{=0} - q^2 \tilde{u}_i \right) - q_i \tilde{p} - \frac{3i}{2}\zeta\tilde{\omega} q_j \left(n_i n_j - \frac{1}{3}\delta_{ij} \right). \tag{4.12}$$

Setting $\mathbf{n} = (1,0,0)$ and considering $i = x$, we get

$$\rho\lambda\tilde{u}_x = -\eta q^2 \tilde{u}_x - iq\cos\theta\tilde{p} - i\zeta\tilde{\omega} q\cos\theta, \tag{4.13}$$

from which we can solve for $\tilde{p}$,

$$\tilde{p} = \frac{i}{q\cos\theta}\left(\rho\lambda + \eta q^2\right)\tilde{u}_x - \zeta\tilde{\omega} = -\zeta\tilde{\omega} - \frac{i\sin\theta}{q\cos^2\theta}(\rho\lambda + \eta q^2)\tilde{u}_y, \tag{4.14}$$

where we have used incompressibility (4.11) in the final step to eliminate $\tilde{u}_x$ in favour of $\tilde{u}_y$. Now, if we consider $i = y$, we get

$$\rho\lambda\tilde{u}_y = -\eta q^2 \tilde{u}_y - iq\sin\theta\tilde{p} - \frac{3i}{2}\zeta\tilde{\omega}\left(-\frac{1}{3} q\sin\theta \right). \tag{4.15}$$

Substituting the expression Eq. (4.14) for $\tilde{p}$ into Eq. (4.15), we get

$$\left(\rho\lambda + \eta q^2\right)\tilde{u}_y = -\frac{\sin^2\theta}{\cos^2\theta}\left(\rho\lambda + \eta q^2\right)\tilde{u}_y + iq\sin\theta\zeta\tilde{\omega} + \frac{i}{2} q\sin\theta\zeta\tilde{\omega}, \tag{4.16}$$

which allows us to solve for $\tilde{u}_y$

$$\tilde{u}_y = \frac{3iq\cos^2\theta\sin\theta\zeta\tilde{\omega}}{2\left(\rho\lambda + \eta q^2\right)}. \tag{4.17}$$

Next, we consider the equation of the perturbed aspect ratio, Eq. (4.9) in Fourier space, which reads:

$$\lambda\tilde{\omega} = 2iq\cos\theta\tilde{u}_x - \Gamma_\omega A_\omega\tilde{\omega} - \frac{3}{2}\Gamma_\omega K_Q q^2\tilde{\omega}. \tag{4.18}$$

Substituting for $\tilde{u}_x$ by using Eq. (4.17) for $\tilde{u}_y$ and the incompressibility relation, Eq. (4.11), we finally get

$$\lambda\tilde{\omega} = \frac{3q^2\cos^2\theta\sin^2\theta\zeta}{\left(\rho\lambda + \eta q^2\right)}\tilde{\omega} - \Gamma_\omega A_\omega\tilde{\omega} - \frac{3}{2}\Gamma_\omega K_Q q^2\tilde{\omega}, \tag{4.19}$$

which, after some algebraic manipulation and a double angle formula gives the dispersion relation

$$q^2\left[\left(\eta + \frac{3}{2}\Gamma_\omega K_Q\rho\right)\lambda + \Gamma_\omega A_\omega\eta - \frac{3}{4}\zeta\sin^2 2\theta\right] + \frac{3}{2}\Gamma_\omega K_Q\eta q^4 + \rho\lambda^2 + \Gamma_\omega A_\omega\rho\lambda = 0. \tag{4.20}$$

The isotropic state is unstable when the growth rate λ becomes positive. For a solution with $\lambda > 0$ to exist for some value of q, we require the coefficient of q^2 to be negative. Therefore, there is a critical value of the activity, ζ_c below which an isotropic system will be stable, given by

$$\zeta_c = \frac{4\Gamma_\omega A_\omega\eta}{3\sin^2 2\theta}. \tag{4.21}$$

ζ_c is clearly minimised when $\theta = \pi/4$. At this angle, the parallel and perpendicular components of the flow work in tandem to create the most efficient elongation of the particles. The resulting dispersion relation is plotted in Fig. 4.3.

Previously, activity was found to create nematic order due to flow aligning effects as long as the product $\xi\zeta$ was positive, and above a certain threshold [27]. Here we provide a mechanism where activity may induce nematic order without the need of flow alignment. Starting from an isotropic system of circular particles, active forces first cause elongation and then thermodynamic forces encoded in the free energy, (4.5) that tend to align elongated particles, or higher order hydrodynamic effects may allow for further nematic order to be established. Indeed, nematic ordering due to flow-driven effects is demoted to a second order effect due to the shape dependence of the flow-aligning parameter, $\xi(\omega) = \xi_0(\omega - 1)$ as given by the co-rotation term, (4.6). Intuitively, we understand that particles require their shape to be sufficiently anisotropic before they can establish strong nematic ordering.

To highlight the competition between active forces and deformation energy costs further, we explicitly write down the critical wavevector, q_0 below which the instability grows:

$$q_0^2 = \frac{\sin^2 2\theta}{2\Gamma_\omega \eta} L_{act}^{-2} - \frac{2}{3} L_{nem}^{-2}, \tag{4.22}$$

which depends on a balance between the active length-scale, $L_{act} = \sqrt{K_Q/\zeta}$, and a newly introduced, passive length-scale, $L_{nem} = \sqrt{K_Q/A_\omega}$. It is important to

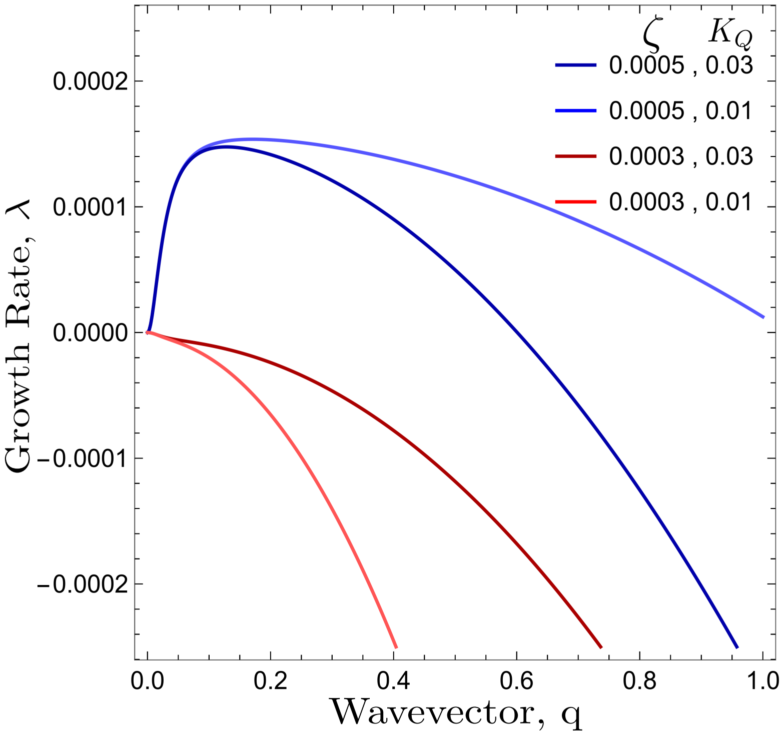

Figure 4.3: Dispersion relation of $\lambda(q)$ from Eq. (4.20) plotted for $\theta = \pi/4$ for different values of $\{\zeta, K_Q\}$. Red/blue curves correspond to activity values smaller/greater than the threshold activity, ζ_c respectively.

note that the above analysis only applies to linear order. The activity threshold given by Eq. (4.21) is a necessary but not sufficient condition for an active nematic system of deformable particles to transition into active turbulence, where non-linear restoring effects become important. In the next section we calculate a lower bound for the activity required to maintain a state of active turbulence based on the flow fields around motile topological defects.

An analytical expression may be obtained for the most unstable wave vector, q_m, which corresponds to the local maximum of the growth rate, λ_m. This is

$$q_m^2 = \frac{\sqrt{2\rho K_Q\Gamma_\omega\zeta \sin^2 2\theta J_+^2 R} - 4\rho K_Q\Gamma_\omega\eta T}{2K_Q\Gamma_\omega\eta J_-^2}, \tag{4.23}$$

$$J_\pm = 2\eta \pm 3\rho\Gamma_\omega K_Q, \tag{4.24}$$

$$R = 3\zeta \sin^2 2\theta - 4\Gamma_\omega A_\omega\eta + 6\rho A_\omega K_Q\Gamma_\omega^2, \tag{4.25}$$

$$T = 3\zeta \sin^2 2\theta - \Gamma_\omega A_\omega J_-. \tag{4.26}$$

Despite the complicated form of the above expression, the competition between activity versus elasticity and energy is shown to be a determining factor for the most unstable modes.

Finally, by assuming a sinuisodal form for the perturbation, $\omega' = \epsilon \sin \mathbf{k}\cdot\mathbf{r}$ for an arbitrarily small value of ϵ and wave vector $\mathbf{k}$ and using the Fourier transform of the sin function, we may also find a solution of the flow field, $\tilde{u}_y$.

$$\tilde{u}_y = \frac{3ik\cos^2\theta\sin\theta\zeta}{2(\rho\lambda + \eta k^2)}\frac{1}{2i}(2\pi)^2\epsilon\left[\delta(\mathbf{k}+\mathbf{q}) - \delta(\mathbf{k}-\mathbf{q})\right]. \tag{4.27}$$

Setting $\lambda = 0$ for simplicity, $\theta = \pi/4$, and inverting the Fourier transform, we get the full flow field (see Fig. 4.4), which reads.

$$u_y = -\frac{3}{4\sqrt{2}}\frac{\zeta\epsilon}{\eta k}\cos\left[\frac{1}{\sqrt{2}}(x+y)\right], \tag{4.28}$$

$$u_x = \frac{3}{4\sqrt{2}}\frac{\zeta\epsilon}{\eta k}\cos\left[\frac{1}{\sqrt{2}}(x+y)\right]. \tag{4.29}$$

The form of the flows that are set up is not unexpected. For particles oriented along the $\hat{x}$ direction, the most efficient elongation may be achieved by applying a shear at an angle of $\theta = \pi/4$, where the long/short axes are most efficiently lengthened/shortened, to increase the overall aspect ratio of the particles. The result of our linear stability analysis implies that, in a confluent system of deformable particles which inherently prefer to have an isotropic shape and exhibit extensile activity, there is a threshold value for the activity required to maintain the particles elongated. This activity may come, for instance, from surrounding nutrients such as ATP. Hence, the result presented here may be experimentally verified by considering a large cell monolayer (so as to approximate the relevant boundary conditions) that exhibits extensile stresses at different concentrations of ATP.

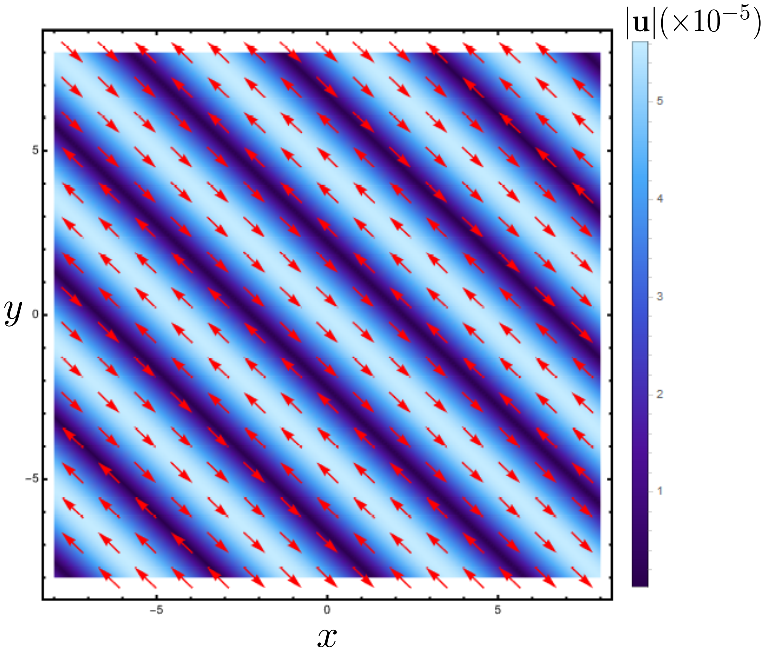

Figure 4.4: Example of the flow field generated by active forces of slightly elongated deformable nematics, given by Eqs. ((4.28), (4.29)). Red arrows indicate flow direction. Colour map represents flow magnitude. Relevant parameter values are $\zeta = 0.001$, $q = 0.2$, $\eta = 2/3$, $\epsilon = 0.01$. The flow fields set up have a characteristic length-scale, which depends on the most unstable wave vector, q_m, and become unstable for activities above the critical value, ζ_c.

4.4 Active turbulence

As we have seen in the previous section, a sufficiently active system is able to drive elongation, and in turn, nematic ordering. If the activity is large enough to transition into active turbulence, highly non-linear effects become important, and we need to solve the full set of Eqs. (4.1) - (4.4) in the most general case. In this section we present the numerical analysis for a bulk system of deformable nematics that exhibits active turbulence, where motile topological defects constantly exist and chaotic flows drive the turbulent behaviour.

4.4.1 Numerical details

We use a hybrid lattice Boltzmann-finite difference method, as highlighted in Chapter 2.6 and discussed in more detail in Appendix A to solve the equations of motion (4.1, 4.2, 4.3, 4.4) [63]. We use a lattice of size is 200×200 with a lattice spacing $\Delta x = 1$, LB timestep $\Delta t = 1$ and periodic boundary conditions to simulate the bulk dynamics of a confluent tissue of highly deformable cells. Unless stated otherwise, the simulation parameters are $\Gamma_Q = 0.1, A_Q = 0.1, K_Q = 0.015, \xi_0 = 0, \Gamma_\omega = 0.01, A_\omega = 0.04, A^\star_\omega = 0.003, \omega_0 = 1, \zeta = 0.001, \rho = 1, \eta = 2/3$. The relevant inverse time-scales are as follows: $\Gamma_\omega A_\omega$, the rate of relaxation of the particles to their preferred shape, $\Gamma_Q A_Q$, the rate of relaxation of the order parameter towards the free energy minimum, and ζ/η, the rate of active stresses injected into the system. In the absence of flow gradients, the regime where $\Gamma_\omega A_\omega \gg \Gamma_Q A_Q$, the magnitude of nematic order, S responds slowly to changes in shape, creating a time delay associated with how particles will align after their shape changes. In the inverse case, nematic alignment responds quickly to shape changes. In the following, we focus on the latter regime. The relevant length-scales are the active length-scale $L_{act} \sim \sqrt{K_Q/\zeta}$ and the passive length-scale $L_{nem} \sim \sqrt{K_Q/A_\omega}$, which sets the scale of shape gradients. Simulations are initialised with random noise in ω around a finite value of $\omega = 1.3$ and $S = (\omega - 1)/\omega$, which is the equilibrium value of the associated free energy we choose, given by Eq. (4.5). We use a runtime of 2×10^5 LB timesteps. Since active turbulence requires a finite time to be established starting from the initial conditions, all quantities are measured after a sufficiently long time of 10^5 timesteps has passed in the simulations.

4.4.2 Dynamics in active turbulence

For values of the extensile activity above which flows are maintained the system enters an active turbulent regime. Fig. 4.5 shows a snapshot of the dynamical steady state corresponding to active turbulence in the system of deformable particles. At any given point in time the system is characterised by distinct regions of elongated particles separated by areas where there is little or no particle extension. There is strong nematic ordering in the regions where the particles are extended, and it is possible to identify the motile topological defects characteristic of active turbulence. Fig. 4.5 (*c*) is to be contrasted with Fig. 2.6 which shows the qualitative dynamics of active turbulence of rigid active nematics. There is a clear difference in the spatio-temporal variation of the nematic order, S, which is a consequence of the thermodynamic effect incorporated into our deformable model where highly elongated particles will tend to align nematically more strongly. This allows for large spatial variations in the nematic order, which, in turn, set up a bootstrap mechanism where the active forces become stronger as cells become more elongated, and vice versa, provided that there are sufficiently large gradients in the orientational field. Such an effect cannot be captured in rigid active nematics, and S only varies slightly from its constant value near nematic domain boundaries. Given the above, it is then not surprising that there will also be a qualitative change in the relevant length-scales associated with topological defect density, which we discuss below.

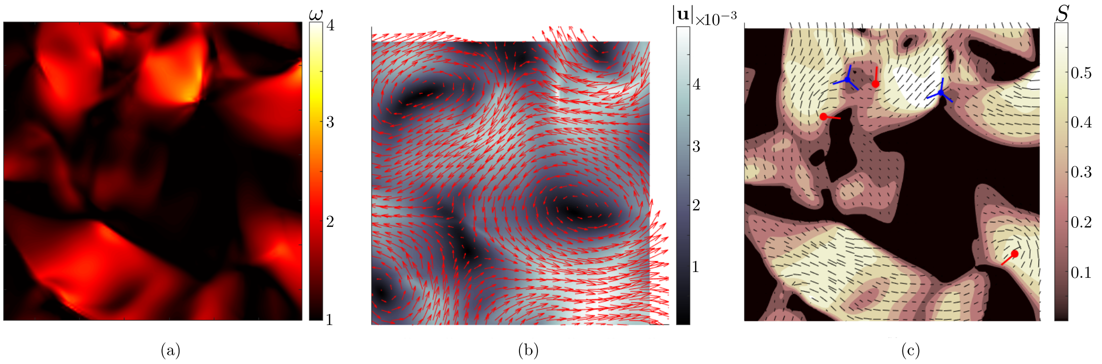

(a) (b) (c)

Figure 4.5: Fully developed active turbulence with deformable particles. (a) Aspect ratio, ω of particles. (b) Velocity field, $\mathbf{u}$. Colour scale indicates the magnitude of the velocity. (c) Nematic director field $\mathbf{n}$ and scalar order parameter S. Colour scale indicates the magnitude of S. Red/blue symbols correspond to the core of ±1/2 defects respectively. +1/2 defects are oriented such that the tail is along the line shown.

Nematic domains

In active turbulence with particles of fixed length, nematic domains are broken up by the active instability and by the passage of topological defects. However, in the case of deformable particles there is an additional mechanism which results in regions of circular particles. Within a nematic domain, the gradients in $\mathbf{Q}$ tend to be smoothened out due to the effect of the nematic elasticity ($\sim K_Q \nabla^2 \mathbf{Q}$), and thus active forces ($\sim \zeta \nabla \cdot \mathbf{Q}$) are diminished. Since these are the forces that tend to elongate particles in an extensile active nematic, the magnitude of the projected strain rate onto the long axis, $E_{\parallel}$, drops, and it is no longer able to overcome the free energy cost of deformation, ($\sim A_\omega(\omega - \omega_0)^2$). For inherently circular particles ($\omega_0 = 1$), which is the case that we are discussing here, the particles within these domains will therefore begin to contract and in turn, so will their nematic order. This process illustrates how the coupling between the active nematohydrodynamic equations and the shape evolution of deformable particles leads to a new mechanism that strongly drives the nematic order in a confluent tissue. However, it is worth noting that the turbulent nature of the system makes the above discussion highly idealised. In practice, it is likely that this process will be disrupted due to nearby vortices and/or motile topological defects that move through the tissue. Fig. 4.6 shows an idealised sketch of the process.

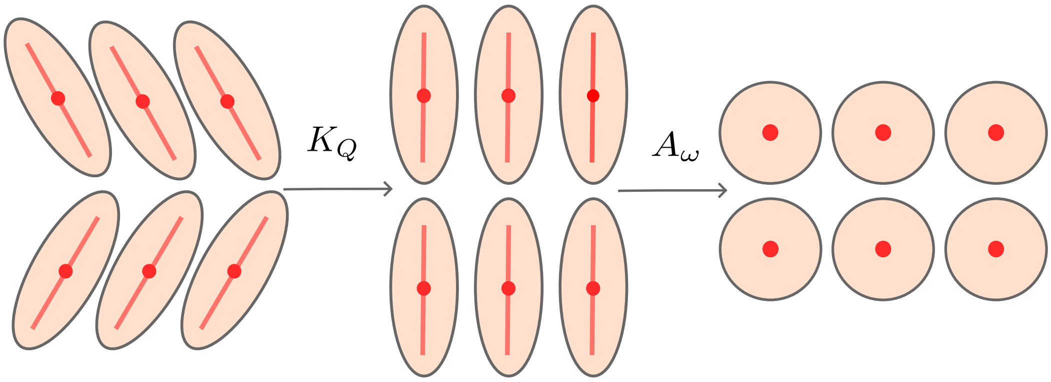

Figure 4.6: Creation and contraction of nematic domains. Nematic elasticity smooths out gradients in the director field, resulting in a domain of aligned directors. The active force vanishes and particles contract due to the elastic free energy cost.

Analysis of physical parameters

We now investigate how physical parameters affect the dynamical state of the system of deformable particles by measuring the time and space averaged aspect ratio, $\langle\omega\rangle$ as the activity parameter ζ, the elastic deformation parameter A_ω, the elastic constant, K_Q and the flow alignment parameter, ξ_0 are varied. In all cases, activity was high enough to keep the system in active turbulence. Fig. 4.7 (a) shows that $\langle\omega\rangle$ increases linearly with the activity for extensile systems. In active turbulence where the evolution of the flow field is dominated by driving from the active stress,

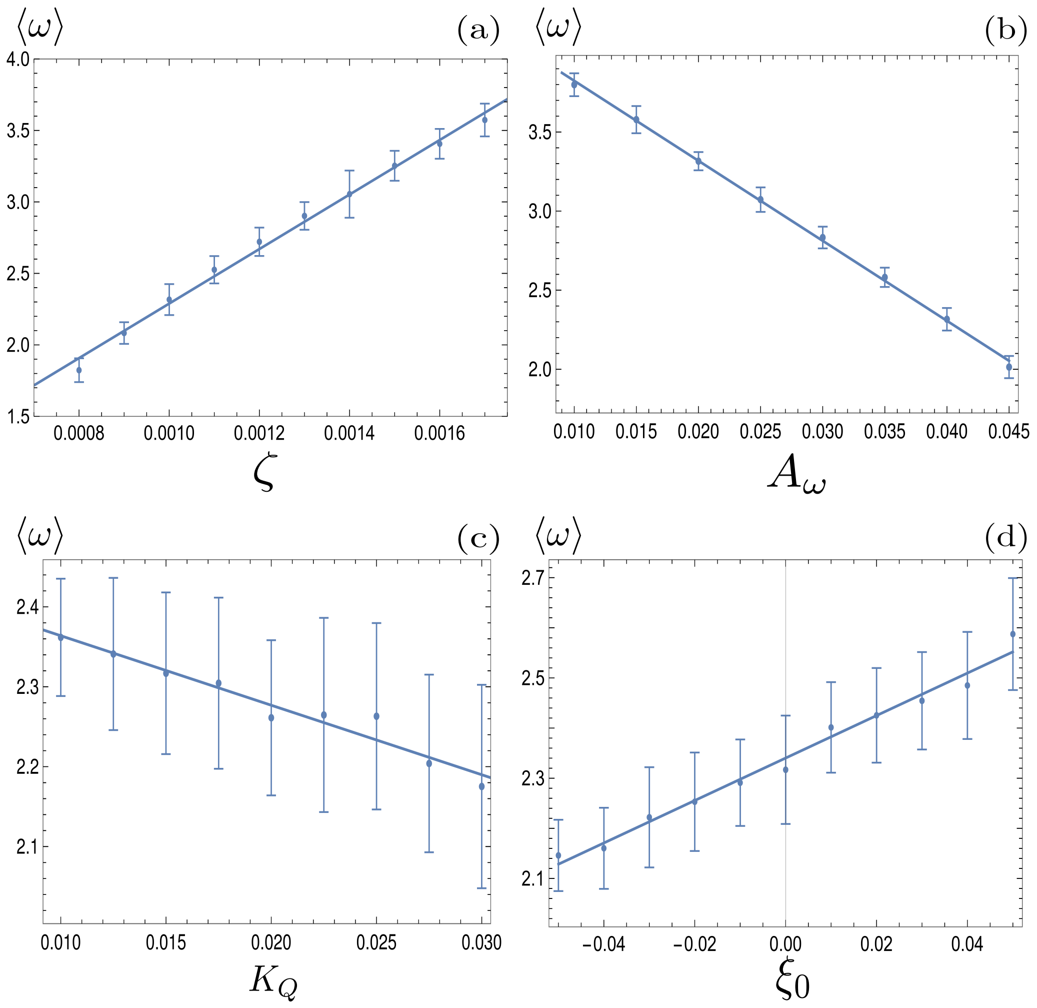

Figure 4.7: Average aspect ratio as a function of (a) the activity, ζ, (b) elastic deformation parameter, A_ω, (c) the elastic constant, K_Q and (d) the flow alignment parameter ξ_0. A linear relationship using a least-squares fit has been plotted in each case. Error bars are given by the standard deviation of the spatial average of the aspect ratio over 10^5 timesteps.

the magnitude of the velocity, and consequently the strain rate, increase with the activity parameter, resulting in a higher degree of elongation. Conversely, Fig. 4.7 (b) shows that $\langle\omega\rangle$ decreases linearly with A_ω. As the elastic energy cost of deforming particles increases, the average aspect ratio will decrease. Next, as K_Q is increased, gradients in the director field are smoothed out, reducing the overall active stress and consequently reducing elongation. This effect is relatively small compared to the other parameters, as Fig. 4.7 (c) shows. Finally, $\langle\omega\rangle$ also increases linearly with the value of the flow aligning parameter, ξ_0, shown in Fig. 4.7 (d). As ξ_0 increases, particles will align more efficiently with the extensional flow axis, thus increasing their elongation.

System length-scales

Next, we look at any emergent length-scales in the system. As we have already shown, in a system of fully developed active turbulence, distinct domains of elongated, anisotropic particles coexist with domains of isotropic particles. To quantify the size of these domains, we calculate the normalised correlation function defined as

$$C_\omega\left(r\right) = \frac{\langle\left(\omega\left(\mathbf{r_0},t\right)-\bar{\omega}\left(t\right)\right)\left(\omega\left(\mathbf{r_0}+\mathbf{r},t\right)-\bar{\omega}\left(t\right)\right)\rangle_{\mathbf{r_0},t}}{\langle\left(\omega\left(\mathbf{r_0},t\right)-\bar{\omega}\left(t\right)\right)^2\rangle_{\mathbf{r_0},t}}, \tag{4.30}$$

where $\bar{\omega}$ is the spatial average of the aspect ratio at each point in time and $\langle\cdot\rangle$ denotes a space and time average over all points separated by a distance r. Fig. 4.8 shows how C_ω varies with distance, scaled by the active length-scale, L_{act}=$\sqrt{K_Q/\zeta}$ for different choices of the activity and elasticity parameters ζ and K_Q respectively. The collapse of the data to a single curve shows that the size of the domains is governed by L_{act}, as in active turbulence with fixed length nematogens, reflecting that flow gradients, which occur on this length scale are responsible for the correlations in the aspect ratio of particles. Additionally, we note the existence of a region of anti-correlation at intermediate distances. This may be explained in a similar fashion to vorticity correlations in active nematics [71, 106]. In an extensile system, the flows generated will *mostly* be such that they tend to elongate particles. However, this is not true throughout the entire system, and patches where the projected strain rate contracts particles will appear at a characteristic length-scale, which is directly related to the active length-scale. Consequently, at these distances, we find that the shape of the particles will be anti-correlated.

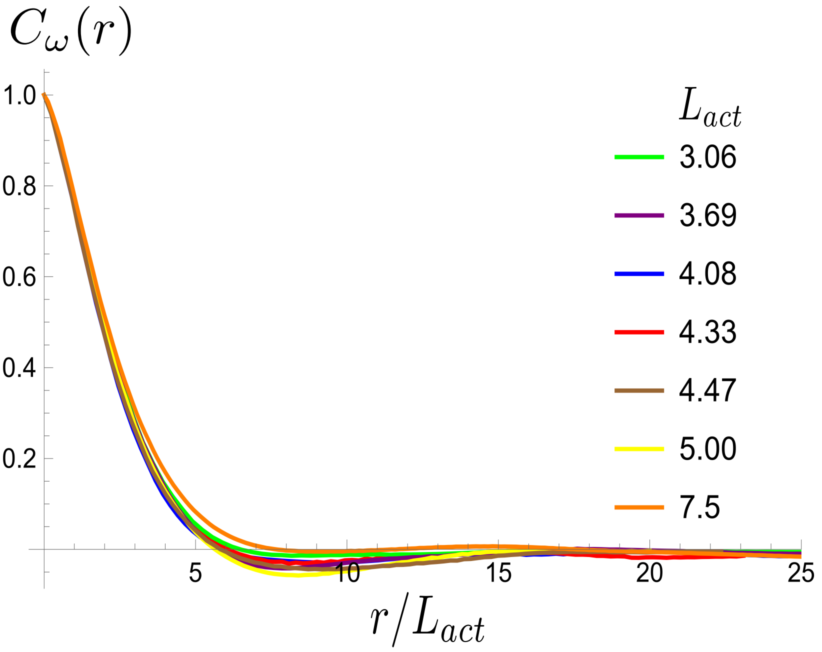

Figure 4.8: Aspect ratio correlation, C_ω as a function of distance, scaled by the active length-scale, $L_{act} = \sqrt{K_Q/\zeta}$. Different coloured curves correspond to differing values of L_{act}, generated by varying ζ and K_Q independently in systems exhibiting fully developed active turbulence. The dips in C_ω below 0 suggest a reproducible anti-correlation at intermediate distances.

We also measure the density of topological defects throughout the system as the activity ζ, the elastic constant K_Q and the cell elasticity A_ω are varied. To obtain this data we track defects [107, 108] and also set a cut-off value $\omega = 1.1$ below which topological defects cannot be observed.

As Fig. 4.9 shows, the defect density scales as $(L^*_{act} L_{nem})^{-1}$ where the modified active length-scale is defined as $L^*_{act}=\sqrt{K_Q/(\zeta - \zeta^*)}$, where ζ^* is the threshold activity required to keep the system in active turbulence - this is taken to be the activity value below which circular cells dominate the system and consequently, topological defects cannot exist. An estimate for this threshold activity is given below.

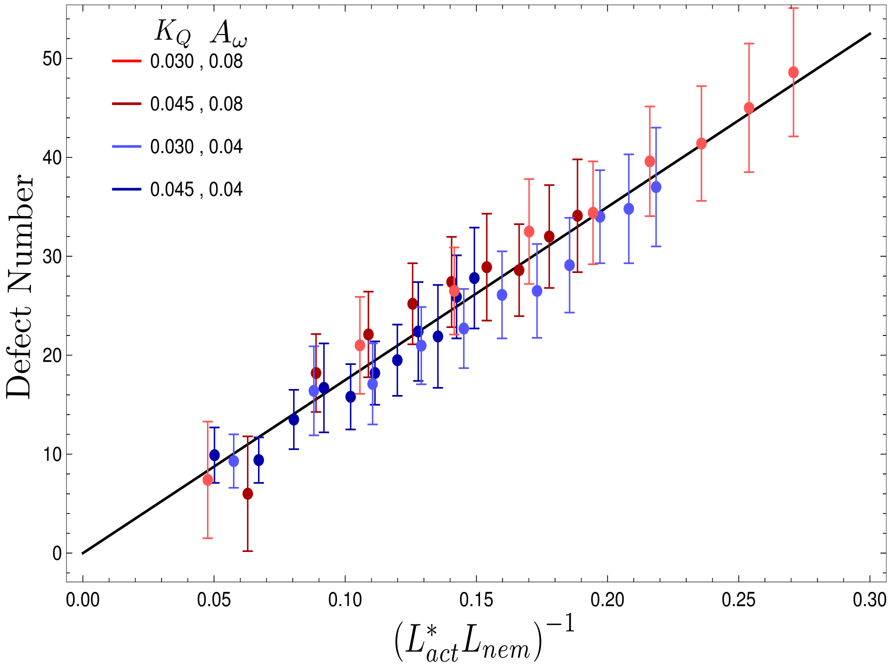

Figure 4.9: Average number of topological defects as a function of the inverse modified active length-scale, L^*_{act} multiplied by L_{nem}. The plotted line shows a least-squares fit through all the data points. Data points were collected by varying the activity parameter, ζ for different realisations of the parameters $\{K_Q, A_\omega\}$. Error bars are given by the standard deviation of the spatial average of the defect number over 10^5 timesteps.

This is an empirical result and is a fundamentally different scaling than fixed length active nematics where the defect density scales with the inverse active length-scale squared, $L_{act}^{-2} = \zeta/K_Q$ [34, 106]. Indeed it seems very reasonable that other length-scales should be involved. One clear difference from the usual active nematic models is that the active stresses depend on the local magnitude of the order parameter and therefore vary across the system, particularly at interfaces, and this will influence the defect count. A plausible explanation for this scaling is as follows: L^*_{act} plays a similar role to L_{act} in traditional active nematics, with a constant offset in the activity due to a minimum threshold required to achieve active turbulence. Secondly, the deformation energy A_ω will tend to reduce the magnitude of the aspect ratio, ω, and therefore the order parameter, S. In turn, this will reduce the effectiveness of the nematic elasticity which depends on S. There is then a reduced, effective elastic constant $\sim K_Q/A_\omega$ so the defect density scales with $L_{nem}^{-1} \sim \sqrt{A_\omega/K_Q}$.

Activity threshold for turbulence

In Fig. 4.9, we referenced an activity threshold, ζ^* that is required to transition into active turbulence. One of its defining characteristics as discussed at the beginning of this section is the existence of motile topological defects. At an activity less than that, no motile topological defects will exist. Therefore, as a first order approximation, we require that the active forces that particles in the vicinity of topological defects experience should keep them at an anisotropic shape, *i.e.* the flow-driven elongation from the extensile active forces around the defects should balance the free energy cost of elongation. If this is not the case, topological defects would not be identifiable since circular particles have no attributable orientation.

An estimate for the threshold activity ζ^* may then be obtained by using the velocity field around ±1/2 defects [66] to calculate the projected strain rate, $E_{\parallel}^{\pm}$. For a defect of range R, a director given by $\mathbf{n} = (\pm\cos\theta/2, \sin\pm\theta/2, 0)$ and assuming $S = (\omega - 1)/\omega$ outside the core, the strain rate is given in polar coordinates by

$$E_{\parallel}^{+}(r,\theta) = \frac{\omega-1}{\omega}\frac{\zeta}{16\eta}\left(\cos 2\theta + 3\right) \tag{4.31}$$

$$E_{\parallel}^{-}(r,\theta) = -\frac{\omega-1}{\omega}\frac{3\zeta}{80\eta}\left(\cos 6\theta + 5\left(\frac{r}{R} - 1\right)\right), \tag{4.32}$$

where $r \in [0, R]$ is the distance from the defect core. By substituting (4.31) into Eq. (4.4), neglecting advection and quartic contributions in the free energy, a simple calculation yields a lower bound to the activity required for particles to elongate along the axis of symmetry of +1/2 defects,

$$\zeta^* = 2\Gamma_\omega A_\omega \eta \tag{4.33}$$

which directly links the ability of the flow gradients ($\sim \zeta$) to overcome the relaxation of the aspect ratio towards the free energy minimum ($\sim \Gamma_\omega A_\omega$).

Comparing Eqs. 4.33 and 4.21, we see that $\zeta^* = \frac{3}{2}\zeta_c$, an increase of 50% from the optimal case of the latter where the wave vector perturbation was along, $\theta = \pi/4$. This matches up with the expectation that the true value of the activity required to transition into active turbulence is larger than the one required for the linear instability. Since motile topological defects are inherently a non-linear phenomenon that arises through the coupling of the nematohydrodynamic equations this comparison illustrates how non-linear effects in the active nematohydrodynamic equations become important at large elongations and nematic order magnitude. Furthermore, this estimate ignores elasticity - it is lower than the numerical values observed in simulations by between 10% for low values of the elastic constant and 50% for high values of the elastic constant.

In this section, we have focused on extensile materials. Contractile systems of particles which are inherently circular will not show any dynamical behaviour because active forces just reinforce the thermodynamic forces restoring the particles to circular. Since contractile activity promotes cell rounding, contractile cell layers stay isotropic and quiescent unless cell elongation is promoted through a free energy contribution, $\omega_0 > 1$. This could be an appropriate choice for systems such as fibroblasts, whose aspect ratio ranges from $\omega_0 \approx 2 - 5$, but have only been studied under a rigid body assumption [109]. Similar qualitative behaviours have been observed in our simulations of contractile systems in fully developed active turbulence, which we have not included in this thesis. Furthermore, we note that our model is restricted to nematic driving: polar forces which can lead to coherent motion of circular cells are also observed in cell monolayers, and the resultant force on a cell does not necessarily act along its nematic axis [30, 110].

4.5 Summary

In this chapter, we have presented the application of our model of deformable nematics presented in Chapter 3 in an active system. By analysing the linear stability of isotropic systems with initially circular nematogens, we showed that there is a finite activity threshold in order to extend particles sufficiently and consequently drive further flows. Above this threshold the system may enter a dynamical steady state characterised by coexisting regions of elongated particles, which tend to align nematically and are associated with topological defects and spatiotemporal chaotic flows, and quiescent regions consisting of isotropic particles.

The turbulent nature of the flows associated with active turbulence means that isotropic particles will be elongated by tissue-scale flow gradients from neighbouring nematic regions, while the extensional flow deep in nematic regions whose gradients in the orientational field decrease will be suppressed over time. Therefore, in regions of high nematic order, the aspect ratio of particles will begin to decrease due to the elastic shape energy. In this dynamical steady-state, particles continuously get stretched by flow gradients and subsequently contract in the absence of flow gradients, leading to large variations of cell shape. This, in turn, modulates their ability to achieve nematic order and leads to a bootstrap effect where elongated particles tend to have a greater magnitude of nematic order, and therefore generate stronger active forces than isotropic particles. Furthermore, we have shown that the associated length-scales of an active turbulent system, such as the characteristic spacing between topological defects, differs from the length-scales observed in active nematic theories of rigid particles.

We close this chapter by highlighting models that resolve individual cells and which show similar shape variations. Vertex models are widely used for understanding tissue dynamics due to their ability to describe the geometry of each individual cell in a confluent epithelium, which in turn allows them to encode physics that would otherwise not be captured by particle-based approaches [111, 112]. Indeed, cell shape anisotropies have been observed to be the main driving factor in simulations of the vertex model for unjammed tissues [113–115] and interpreted in terms of a continuum model [80]. Additionally, shape-tension coupling has been shown to produce nematic order through the creation of active T1 transitions that drive tissue shapes and elongate cells in an epithelium vertex model [116, 117]. In turn, the resulting shape anisotropy, when coupled to an epithelium where viscous dissipation dominates over substrate friction has been shown to drive long-range velocity correlations, enabling the emergence of flows where spatiotemporal organisation is possible [118]. These results displayed by active vertex models demonstrate how cell shape dynamics are linked to collective processes, such as cancer invasion, wound healing and morphogenesis.

Other approaches, such as phase field models where each cell is described by an individual field are a particularly convenient way to describe cell-level dynamics. Intracellular and intercellular forces may be implemented in a transparent way, and passive and active contributions may be distinguished. Active phase field models have been successful in capturing the emergence of active nematic behaviours [46, 119, 120] and cell sorting [121] in cell monolayers. Further, the ability of cells to mediate their shape and area has been shown to be a driving factor in the spontaneous formation of holes in confluent cell monolayers, driven by the large strains near topological defects [122]. The model discussed in this chapter is limited by the assumption of constant density throughout the system. In that regard, it would be interesting to explore the consequences of relaxing this assumption in future works. This would allow us to explore the effects of shape variations on the formation of holes in confluent systems, as seen in other models [122].

Mean field theories of cell shape variations based on the vertex and cellular Potts models have also been presented where the energy function used to penalise cell shape and area, coupled with the geometrical restriction of confluency a probability distribution function of the aspect ratio of cells which has shown excellent agreement with simulations and experiments [81, 123].

5

Phase synchronisation of deformable particles

In this chapter, we switch gears from the continuum level descriptions analysed previously in this thesis and discuss *dilute* suspensions of particles where the continuum level nematohydrodynamic equations introduced in Chapter 2 do not apply. We begin by providing a brief introduction to the mathematical tools that we shall use from the literature of phase synchronisation. Broadly speaking, phase synchronisation, or "phase locking" refers to the phenomenon where the relative phase angles of weakly coupled oscillators will eventually repeat in a consistent pattern. In the context of this work, phase synchronisation will refer to an emergent phenomenon where the particles under consideration eventually develop nematic order, *i.e.* their orientations are aligned at all times. Importantly, we shall show that this can happen not by particle-particle interactions, but due to a non-linear coupling to an oscillatory driving. Ultimately, we show how a system of non-interacting, deformable particles may create global nematic order through such a mechanism in the presence of oscillating flows.

We begin by considering pedagogical examples that are closely tied to our final goal. First, we consider the simplest case of rigid nematics in oscillating shear flow and show that phase synchronisation is not possible for this system. Following that, we consider oscillating chiral flows instead, where we find phase synchronisation occurring, suggesting that the coupling of the oscillatory driving to the evolution of the phase variable is an important ingredient. We then show that, by relaxing the assumption of rigidity, oscillations in the shape of particles may also lead to phase synchronisation. In doing so, we show that the ability of particles to modulate their shape, along with its coupling to the orientational dynamics is a viable route to inducing nematic order. Finally, we consider how a dilute suspension of non-interacting deformable nematic particles subjected to an oscillating shear flow may develop global nematic order that arises through the phenomenon of phase synchronisation. To demonstrate this, we use a dynamical systems approach.

5.1 Introduction

Classical theories predict the emergence of nematic order: Some examples include Maier-Saupe theory based on anisotropic attractive interactions [124, 125] and Onsager's theory based on the gain in translational entropy at the expense of lowered orientational entropy of the particles [52]. Athermal, active and external fields [46, 126–129] can also drive the isotropic - nematic transition. Notably, all these approaches rely on the interactions between anisotropic particles or external fields that directly induce order and, as previously discussed in this thesis, they also ignore a characteristic feature ubiquitous in soft and biological matter, namely the deformability of the constituents, e.g., polymers, soft colloids, emulsions and cells [4, 130].

Meanwhile, in previous chapters, we have discussed how nematic order in a confluent system at a large scale may be driven through volume exclusion effects, where highly elongated particles will tend to align more effectively with each other so as to occupy the entire available space. In this chapter, we will drop this assumption and show how shape deformability in conjunction with shape anisotropy can induce nematic order of non-interacting particles in a periodically driven, dilute suspension, via a phase synchronisation mechanism. As opposed to particle-particle interactions that are traditionally responsible for nematic order in liquid crystals

[51, 55] or synchronisation in Kuramoto models [131], the proposed mechanism is rooted in non-equilibrium driving.

This chapter is structured as follows: In Sec. 5.2 we provide a brief introduction to the mathematical formulation of phase synchronisation and illustrate how this will be applied in our case. Then, in Sec. 5.3 we apply the mathematical tools presented to some pedagogical examples. In particular, we show how a system of rigid particles in an oscillatory shear flow will *not* exhibit phase synchronisation, whereas they will do so for an oscillatory chiral driving and for a steady shear flow, with active shape oscillations. We then follow that up in Sec. 5.4 by considering the main system of discussion in this chapter - anisotropic, deformable nematic particles subjected to an oscillating shear flow. By analysing the dynamical system, we show that the synchronised state corresponds to a unique, stable limit cycle confined in the state space of the dynamical variables. These synchronised regions emerge as Arnold tongues. These are well known structures in the parameter-space of the driving parameters [132, 133]. Finally, in Sec. 5.5 we provide a discussion and summary of our results.

5.2 Introduction to phase synchronisation

In Sec. 5.1 we referred to the phenomenon of phase synchronisation. It is based on the well known fact that two weakly coupled oscillators can synchronise their oscillations [133] and there are several examples of synchronisation which are ubiquitous, such as flashing fireflies [134], pendulum clocks [135], mammalian cell cycles [136], beating cilia of microorganisms [137, 138], and optomechanical and nanomechanical oscillators [139, 140]. A particular case of synchronisation is the entrainment of an oscillator by an external, periodic driving. In this case, the coupling is unidirectional, *i.e.* the external driving can influence the oscillator but not vice versa, which is the type of coupling we will be focusing on in this chapter. Then the frequency and phase of the driven oscillator gets locked onto the driving signal, resulting in phase synchronisation [132, 133]. Examples of systems that exhibit phase synchronisation due to entrainment are hair cells of the inner ear [141, 142], Josephson junctions [143, 144] and driven colloidal systems in periodic potentials [145, 146].

We now present the mathematical analysis that underlies these examples. Consider a general dynamical system of the form

$$\dot{\mathbf{x}} = \mathbf{F}(\mathbf{x}; \alpha),$$

where $\mathbf{x}$ is the vector consisting of all the dynamical variables, $F(\cdot)$ is a general nonlinear differentiable function and α is a control parameter of the system. If we now allow this control parameter to oscillate in time with some small amplitude ϵ, i.e. $\alpha(t) = \alpha_0 + \epsilon \sin(\omega t)$, then we have

$$\dot{\mathbf{x}} = \mathbf{F}(\mathbf{x}; \alpha_0 + \epsilon \sin(\omega t)).$$

If $\epsilon \ll \alpha_0$, then we can perform a perturbation expansion in powers of ϵ and get the following leading order equations:

$$\dot{\mathbf{x}} \approx \mathbf{F}(\mathbf{x}; \alpha_0) + \epsilon \left.\frac{\partial \mathbf{F}}{\partial \alpha}\right|_{\alpha=\alpha_0} \sin(\omega t).$$

Hence, an oscillatory parameter perturbation can be viewed as a periodically varying external driving (with a state dependent coefficient) and we get the general form of the dynamical system

$$\dot{\mathbf{x}} = \mathbf{F}(\mathbf{x}; \alpha_0) + \epsilon \mathbf{G}(\mathbf{x}; \alpha_0) \sin(\omega t), \tag{5.1}$$

where $\mathbf{G}(\mathbf{x}; \alpha_0) = \left.\frac{\partial \mathbf{F}}{\partial \alpha}\right|_{\alpha=\alpha_0}$.

We can do a reduction of our dynamical system to the phase variable ψ that changes along the limit cycle of the undriven system *i.e.* $\epsilon = 0$. We introduce ψ, as is traditionally done during phase reduction of a dynamical system when analysing for synchronisation [133], as follows:

$$\frac{d\psi(\mathbf{x})}{dt} = \omega_n. \tag{5.2}$$

ψ is a co-ordinate along the limit cycle and it grows uniformly with $\dot{\psi} = \omega_n$ where $\omega_n = 2\pi/T_n$ with T_n as the natural period of the limit cycle of the unperturbed system.

The dynamics of this phase variable ψ for the unperturbed system are given by

$$\frac{d\psi_u}{dt} = \omega_n = \frac{\partial \psi_u}{\partial \mathbf{x}} \cdot \dot{\mathbf{x}} \tag{5.3}$$

Now, the dynamics of ψ for the perturbed system can be calculated in a similar way using our leading order equation Eq. (5.1) for the driven system as follows (see Chapter 7 of [133]):

$$\begin{aligned} \frac{d\psi}{dt} &= \frac{\partial \psi}{\partial x_i} F_i(\mathbf{x}; \alpha_0) + \epsilon \frac{\partial \psi}{\partial x_i} G_i(\mathbf{x}; \alpha_0 \sin \omega t), \\ &= \omega_n + \epsilon S(\psi) \sin \omega t, \end{aligned} \tag{5.4}$$

where $S(\psi) = \frac{\partial \psi}{\partial x_i} G_i(\mathbf{x}; \alpha_0)$ and it is understood that the RHS is calculated on the limit cycle of the unperturbed system, hence the first term reduces to ω_n as given by Eq.(5.3).

Integrating Eq. (5.4) for the ψ over one period of the driving $T = 2\pi/\omega$ we obtain

$$\begin{aligned} \int_{kT}^{(k+1)T} \frac{d\psi}{dt} dt = \int_{kT}^{(k+1)T} \omega_n dt + \int_{kT}^{(k+1)T} \epsilon S(\psi) \sin(\omega t) dt, \\ \psi_{k+1} = \psi_k + 2\pi \frac{\omega_n}{\omega} + \epsilon\, f(\psi_k), \end{aligned} \tag{5.5}$$

where $f(\psi_k) = \int_{kT}^{(k+1)T} S(\psi) \sin(\omega t) dt.$ Thus, we get a circle map with some nonlinear function $f(\cdot)$ which can in general exhibit phase synchronisation behaviour [147] with the quantitative details of regions of synchronisation governed by the form of the nonlinearity $f(\cdot)$.

The above procedure is general and will become more concrete when we apply it in the next section for a number of different systems, and illustrate some of the consequences and results of the phase synchronisation in the cases where it exists.

5.3 Applications of phase synchronisation

In this section, we consider three different systems as examples to illustrate the mechanism of phase synchronisation, or lack thereof, by employing the mathematical formulation discussed in 5.2 and numerical simulations.

5.3.1 Rigid elongated particles in oscillating shear flow

We consider a dilute suspension of rigid nematics subjected to an imposed oscillatory shear flow, where we ignore any backflow effects from the particles on to the flow. In this case we only have one ordinary differential equation describing the orientational dynamics of the angle of the particles to the x-axis, θ, commonly known as the Jeffery's equation [148]. This reads as

$$\dot{\theta} = \frac{\dot{\gamma}}{2}\left(\beta(r)\cos 2\theta - 1\right). \tag{5.6}$$

Here $\dot{\gamma} = 1 + A\sin\omega t$ is the imposed shear rate, with an oscillatory component of magnitude A and angular frequency ω. The shape dependent term $\beta(r)$ is given by

$$\beta(r) = \frac{(r+1)^2 - 1}{(r+1)^2 + 1}, \tag{5.7}$$

where r is the aspect ratio of the particle, minus unity, and is fixed. Assuming that $A \ll 1$, we may apply the procedure highlighted in Sec. 5.2 to construct the circle map of the system which will, in turn, allow us to identify whether the system is capable of phase synchronisation. We first simplify the ODE to the following:

$$\dot{\theta} \approx F(\theta) + A\,G(\theta)\sin(\omega t),$$

where

$$G = \left.\frac{\partial F}{\partial \dot{\gamma}}\right|_{\dot{\gamma}=1} = F(\theta).$$

Hence we have,

$$\dot{\theta} = F(\theta) + AF(\theta)\sin(\omega t). \tag{5.8}$$

Introducing the phase variable ψ_u of the undriven system as follows

$$\psi_u = \omega_n \int_0^\theta \dot{\theta'}^{-1}(\theta', t)\,d\theta',$$

with $\dot{\psi_u} = \omega_n$ where $\omega_n = 2\pi/T_n$ with T_n as the period of the limit cycle of the unperturbed system. Thus we get,

$$\frac{d\psi_u}{d\theta} = \frac{\omega_n}{\dot{\theta}} = \frac{\omega_n}{F(\theta)},$$

where the derivative is calculated on the limit cycle of the unperturbed system $\dot{\theta} = F(\theta)$ (see Chapter 7 of Ref. [133] for further details), giving

$$\frac{d\psi_u}{d\theta} F(\theta) = \omega_n.$$

Now the rate of change of the phase variable for the driven system results in,

$$\frac{d\psi_d}{dt} = \frac{d\psi_u}{d\theta}\dot{\theta} = \frac{d\psi_u}{d\theta} F(\theta) + A\,\frac{d\psi_u}{d\theta} G(\theta)\sin(\omega t).$$

Once more, $d\psi_u/d\theta$ is calculated on the limit cycle of the unperturbed system. This procedure gives,

$$\frac{d\psi}{dt} = \omega_n + A\,\frac{d\psi}{d\theta} G(\theta)\sin(\omega t), \tag{5.9}$$

where we have dropped the subscripts and understand that the RHS corresponds to dynamics of the unperturbed system. By changing variables everywhere from θ to ψ we can rewrite the above equation as

$$\frac{d\psi}{dt} = \omega_n + A\,S(\psi)\sin(\omega t), \tag{5.10}$$

where $S(\psi) = \frac{d\psi}{d\theta} G(\theta)$.

Now, in general, integrating Eq. (5.10) over one period of the driving oscillator *i.e.* $T = 2\pi/\omega$ will give a circle map as follows

$$\int_{kT}^{(k+1)T} \frac{d\psi}{dt} dt = \int_{kT}^{(k+1)T} \omega_n dt + A \int_{kT}^{(k+1)T} S(\psi)\sin(\omega t) dt,$$

$$\psi_{k+1} = \psi_k + 2\pi\frac{\omega_n}{\omega} + f(\psi_k), \tag{5.11}$$

where $f(\psi_k) = \int_{kT}^{(k+1)T} S(\psi)\sin(\omega t)dt$. However, in this case we have

$$S(\psi) = \frac{d\psi}{d\theta} G(\theta) = \frac{d\psi}{d\theta} F(\theta) = \omega_n.$$

Hence, in this case $f(\psi_k) = 0$ and the circle map reduces to

$$\psi_{k+1} = \psi_k + 2\pi\frac{\omega_n}{\omega}.$$

This will give periodic or quasiperiodic limit cycles when the ratio of the two frequencies ω_n and ω is a rational or an irrational number, respectively, but it will never exhibit phase locking [147]. Therefore, rigid particles will never phase synchronise with the oscillatory driving and, as a result, a dilute suspension of them will therefore also not phase synchronise with each other through the external driving alone. The above analysis shows that not all oscillatory perturbations will result in phase locking and synchronisation, suggesting that the nature of the non-linearity is a key ingredient.

5.3.2 Rigid elongated particles with oscillating chiral activity

In Sec. 5.1, we introduced the idea that the nature of the non-linearity due to the external oscillatory driving is a key factor in determining whether phase synchronisation occurs. Indeed, periodic driving of other internal degrees of freedom may result in phase synchronisation. As a first example, we consider rigid nematic particles in steady shear flow having a time-periodic internal chiral activity. The orientational dynamics of such a particle are modelled by

$$\dot{\theta} = \frac{\dot{\gamma}}{2}\left(\beta(r)\cos(2\theta) - 1\right) + \omega_a(t) \tag{5.12}$$

where $\omega_a(t) = A\sin(\omega t)$ is a pulsating internal chiral activity *i.e.* angular velocity, and $\dot{\gamma}$ is now fixed. In the absence of the chiral activity, the system will have a natural period of oscillations, given by the time it takes for the orientation to rotate by an angle of π, due to the nematic symmetry of the particles. We refer to this natural period as T_n. Following the same analysis as in Sec. 5.3.1, we arrive at the equation for the phase variable, defined once more by Eq. (5.3.1)

$$\psi_{k+1} = \psi_k + 2\pi\frac{\omega_n}{\omega} + f(\psi_k), \tag{5.13}$$

where $f(\psi_k) = \int_{kT}^{(k+1)T} \frac{d\psi}{d\theta}\sin(\omega t)dt \neq 0$ since the relation between the phase variable and the dynamical variable is not trivial, *i.e.* $d\psi/d\theta$ is not a periodic function of t such that the integral vanishes. This gives a circle map with some nonlinearity $f(\cdot)$ and the system can exhibit phase synchronisation for a range of parameters.

To illustrate this, we construct the associated Arnold tongues of synchronisation obtained by numerically solving the system of a suspension of non-interacting particles that each follow the dynamics given by Eq. (5.12). These are shown in Fig. 5.1. We see that the tips of the Arnold tongues appear when the driving period, T is an integer multiple of the natural period of the non-oscillatory driven system, T_n. This phenomenon makes intuitive sense and has been observed in the literature [133]. If the period of the oscillatory driving is near an integer multiple of the natural period of the system, only a small perturbation is required to attenuate the natural period and synchronise them completely. Within the Arnold tongues, the limit cycles of each individual particle that is subjected to this flow will synchronise with each other, and their orientation angles will become equal at each point in time. This is a well known result in the literature of phase synchronisation referred to as phase locking and is a point we will revisit later [133].

Given the above analysis, an important conclusion we may arrive at is that a required ingredient for phase synchronisation to take place is the nature of the non-linearity that is introduced from the oscillatory driving. In Sec. 5.3.1, the oscillatory shear did not lead to synchronisation, whereas the chiral activity considered here does so. Next, we will consider whether non-linearities associated with the shape of particles are sufficient to drive phase synchronisation.

5.3.3 Elongated particles with active shape deformations

In this section, we consider actively shape-changing elongated particles in steady shear flow and show that they can also exhibit phase synchronisation and hence nematic order emerges for many such non-interacting particles. Motile cells and microswimmers can undergo shape oscillations or move their appendages in a periodic way to propel themselves at low Reynolds number and these oscillatory motions maybe approximated as active shape fluctuations [149–151]. It has been shown using a triangular bead-spring model that active shape changes can phase lock to flow-induced tumbling [152].

Here we analyse a simple situation of periodic oscillations in the shape parameter r of our model. We start with the equation for orientational dynamics of the rigid

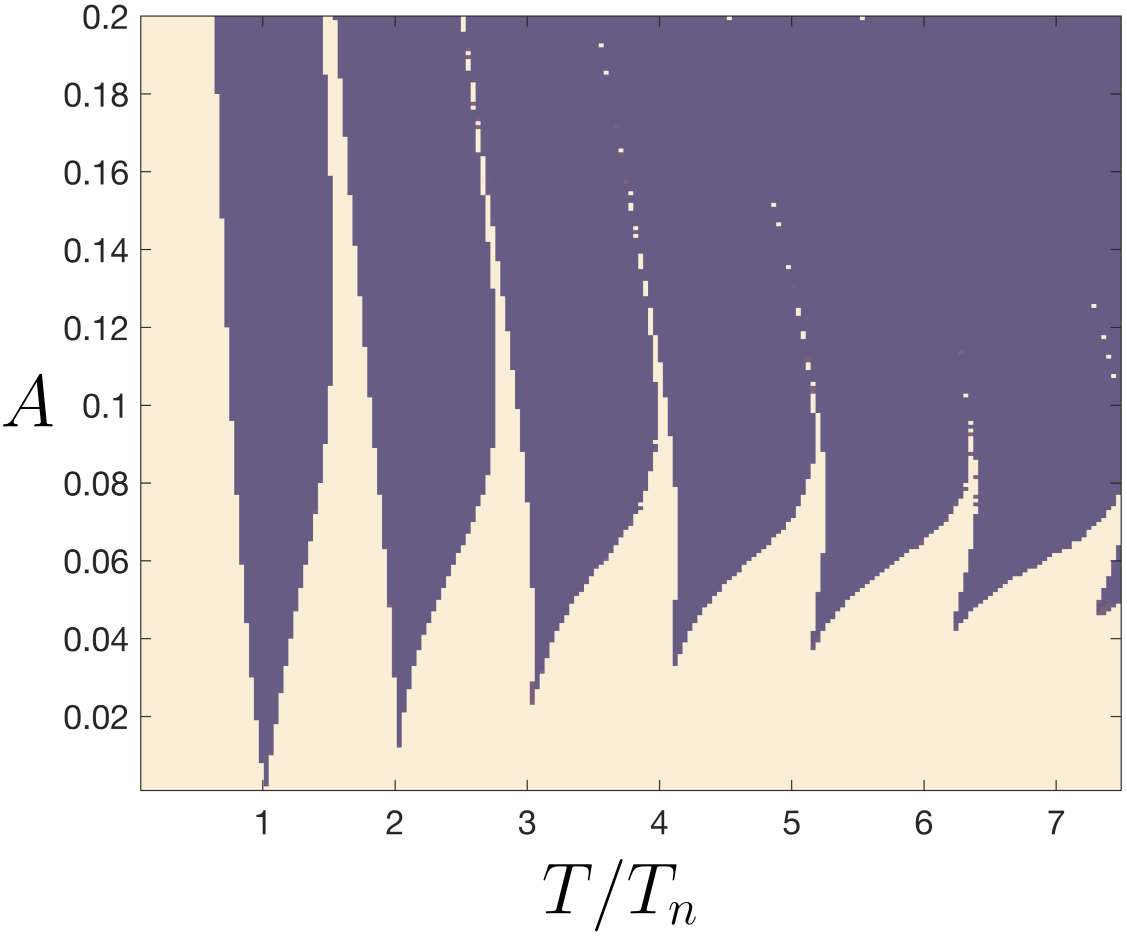

Figure 5.1: Arnold tongues showing phase synchronisation (violet regions) in the parameter space formed by the ratio of the driving period T to the natural period T_n and the driving amplitude A for rigid elongated particles whose orientational dynamics are governed by Eq. (5.12), with fluctuating chirality given by $\omega_a(t) = A\sin(\omega t)$ with $r = 3$. Here $\omega = 2\pi/T$, $\dot{\gamma} = 1$ and $T_n \approx 13.35$. Arnold tongues were generated by running simulations for sufficiently long times, $t \approx 1000T$ and checking whether the periods converged within a small tolerance. Violet regions not visible at low values of A and integer values of T/T_n are due to the resolution of parameter grids.

elongated particle as in Eq. 5.6

$$\dot{\theta} = \frac{\dot{\gamma}}{2}\left(\beta(r)\cos 2\theta - 1\right) = F(\theta; r). \tag{5.14}$$

However, instead of introducing a time dependence in the flow, we consider an active particle undergoing shape oscillations given by $r = r_0 + A\sin(\omega t)$, where r_0 is the mean value of the shape parameter, and $A \ll r_0$. Then, doing a perturbation expansion in A and only keeping the leading order term we get

$$\dot{\theta} \approx F(\theta) + A\,G(\theta)\sin(\omega t), \tag{5.15}$$

where $F(\theta) = F(\theta; r)$ evaluated at $r = r_0$ and

$$G(\theta) = \frac{\partial F}{\partial r}\bigg|_{r=r_0} = 2\dot{\gamma}\cos(2\theta)\frac{r_0+1}{((r_0+1)^2+1)^2}, \tag{5.16}$$

which can be written in terms of $F(\theta)$ as follows

$$G(\theta) = \frac{4(r_0+1)}{((r_0+1)^4-1)}F(\theta) + \frac{2\dot{\gamma}(r_0+1)}{((r_0+1)^4-1)}. \tag{5.17}$$

We now follow the same analysis as in Sec. 5.3.1 and introduce the phase variable ψ giving us $\frac{d\psi}{d\theta}F(\theta) = \omega_n$ for the unperturbed system and if we let $S(\psi) = \frac{d\psi}{d\theta}G(\theta)$ then the circle map in ψ for the perturbed system reads as

$$\psi_{k+1} = \psi_k + 2\pi\frac{\omega_n}{\omega} + A\,f(\psi_k), \tag{5.18}$$

where $f(\psi_k)$ is given by

$$\begin{aligned} f(\psi_k) &= \int_{kT}^{(k+1)T} S(\psi)\sin(\omega t)dt = \int_{kT}^{(k+1)T} \frac{d\psi}{d\theta}G(\theta)\sin(\omega t)dt \\ &= \frac{4(r_0+1)}{((r_0+1)^4-1)}\int_{kT}^{(k+1)T} \omega_n \sin(\omega t)dt + \frac{2\dot{\gamma}(r_0+1)}{((r_0+1)^4-1)}\int_{kT}^{(k+1)T}\frac{d\psi}{d\theta}\sin(\omega t)dt \\ &= \frac{2\dot{\gamma}(r_0+1)}{((r_0+1)^4-1)}\int_{kT}^{(k+1)T}\frac{d\psi}{d\theta}\sin(\omega t)dt, \end{aligned}$$

since the first term on the RHS integrates to 0 over one driving period. This again gives a circle map with some nonlinearity $f(\cdot)$ and can exhibit phase synchronisation. Arnold tongues of the regions of synchronisation are obtained by numerically solving the system are shown in Fig. 5.2.

Note that in this case we may get the form of

$$\psi(\theta) = \frac{-2\omega_0}{\sqrt{1-\beta^2}\dot{\gamma}}\arctan\left(\sqrt{\frac{1+\beta}{1-\beta}}\tan\theta\right),$$

where

$$\beta = \frac{(r_0+1)^2-1}{(r_0+1)^2+1}.$$

This allows us to explicitly calculate $d\psi/d\theta$ in terms of $\psi = \omega_0 t$ and hence get the functional form of the circle map as long as the required integral is analytically solvable. This would in turn allow us to analytically compute explicit bifurcation diagrams and fit theory to experiments, rather than matching qualitative features

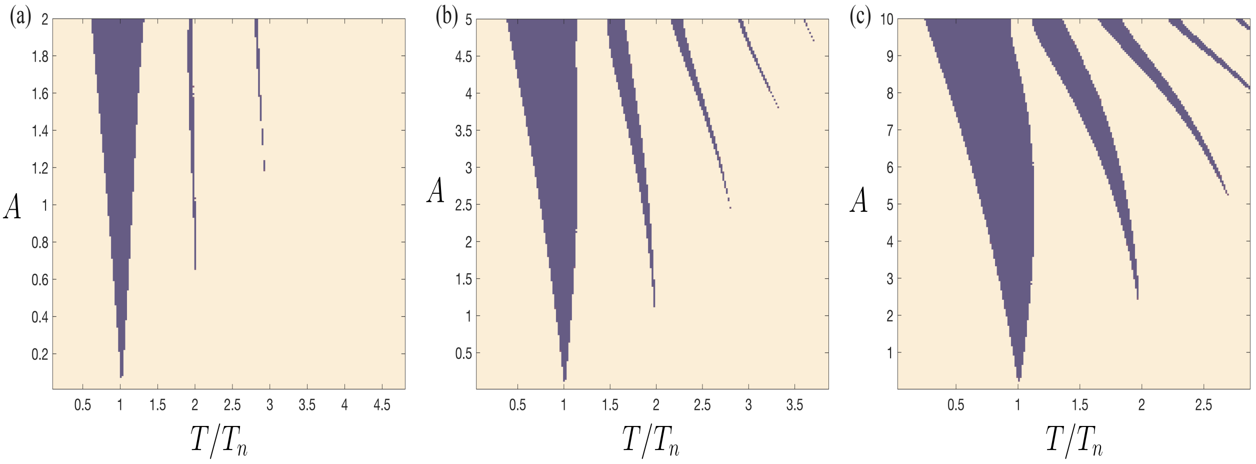

Figure 5.2: Arnold tongues showing phase synchronisation (violet regions) in the parameter space formed by the ratio driving period T to the natural period T_n and the driving amplitude A for elongated particles with active shape deformations, following Eq. (5.14) with a shape parameter given by $r(t) = r_0 + A\sin(\omega t)$ with (a) $r_0 = 2$, (b) $r_0 = 5$ and (c) $r_0 = 10$. Here $\omega = 2\pi/T$, $\dot{\gamma} = 1$ and the natural periods are $T_n \approx 10.4$ for $r_0 = 3$, $T_n \approx 19.375$ for $r_0 = 5$, and $T_n \approx 34.8$ for $r_0 = 10$. Arnold tongues were generated by running simulations for sufficiently long times, $t \approx 1000T$ and checking whether the periods converged within a small tolerance.

alone. However, due to time constraints, we do not pursue that in this thesis and is left for future works. It is also worth noting that this approach will not be applicable for more complex systems where the analytical form of ψ may not be readily computed.

The simplified system considered here is particularly pedagogical in relation to our analysis of how deformability allows for phase synchronisation. This is because it provides us with a way to get a physical intuition about how the edges of the Arnold tongues are determined. Within the tongues, in the (r, θ) phase space, the dynamics will display a limit cycle - a closed trajectory which other trajectories will spiral into. Depending on the exact location within the Arnold tongues, the trajectory of the limit cycle will exhibit an asymmetry that is most pronounced near its ghost region (the region in the phase space where the phase variable's speed is at its minimum), see Fig. 5.3, trajectory I.

The boundaries of the Arnold tongues may be computed by noting that at those points, the driving will tend to make the orbit of θ speed up or slow down, depending on whether the driving period is lower than, or greater than the natural period of the orbit, respectively. This prescribes some specific conditions to the values of the variables, in our case, r and θ. More specifically, from Eq. (5.14) we see that the ghost region happens around $\theta = 0$, where the strain-rate term ($\sim \cos 2\theta$) most strongly competes with the vorticity to slow down the orientational dynamics. This is modulated by the shape dependent factor $\beta(r)$ which is given by Eq. (5.7) and is a monotonically increasing function of r. Therefore, the value of the elongation will be $r = r_0 \pm A$ when trying to slow down or speed up respectively at the edges of the tongue since these are the values that will most efficiently do so. If a modulation of the shape with the greatest magnitude possible is not sufficient to drive the period of the limit cycle towards the driving period for a given set of parameters, then the system will not lie within an Arnold tongue. Additionally, the trajectory of the limit cycle at the edge of an Arnold tongue becomes completely symmetric, as shown in Fig. 5.3 trajectory II, with r reaching its maximum value at $\theta = 0$ and its minimum value at $\theta = \pi/2$.

To make this more concrete, we note that since, $T > T_n$, where T_n is the natural period of the limit cycle, the driving attempts to slow down the the rotation. The functional form of $\dot{\theta}$ shows that the critical slowing down happens at $\theta = 0$. The most efficient way to slow down the cycle further is then to have $r = r_{max} = r_0 + A$ at $\theta = 0$. This is because the strain rate term ($\sim \cos 2\theta$) in Eq. (5.14) has the opposite sign of the vorticity at that point, further exacerbating the slowdown of the limit cycle, and vice versa at $\theta = \pi/2$. This is in line with the discussion above: The edge of the Arnold tongue is determined by the extent of the ability of the shape to modulate the period. If the most efficient way of slowing down (or speeding up) a limit cycle is still not sufficient to drive the period of the limit cycle to that of the perturbation, no synchronisation can occur.

Further, we may now understand why the Arnold tongues are slanted in a specific direction. The functional form of $\beta(r)$ is concave, *i.e.* $\beta''(r) < 0, \forall r \in [0, \infty)$. This means that the value of this function changes more drastically by decreasing r, compared to increasing r by the same amount. Near $\theta = 0$, when $T < T_n$, the driving tries to have $r < r_0$ and vice versa for $T > T_n$. The former case is therefore more efficient at speeding up the limit cycle than the latter is at slowing it down. The tongues are therefore slanted in the direction of smaller T.

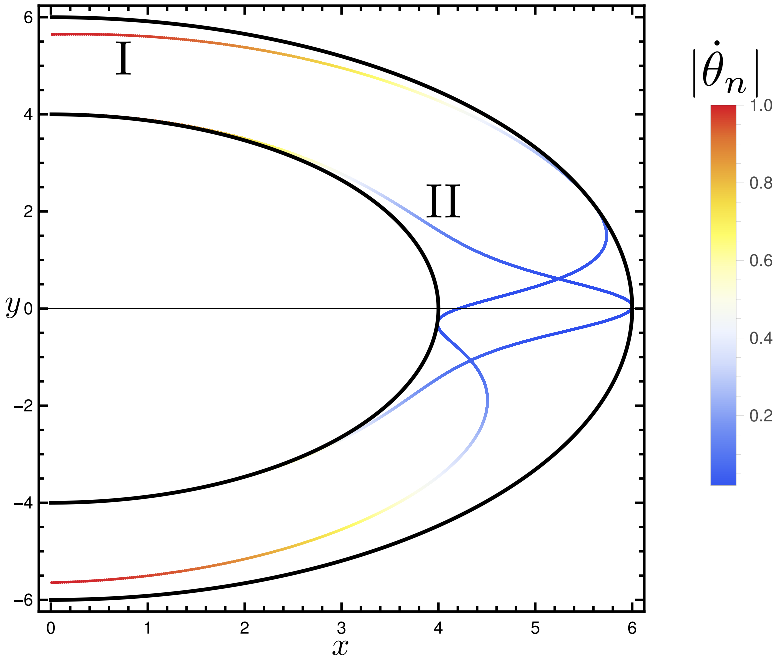

Figure 5.3: Phase space trajectories on a Cartesian grid, where the polar coordinates correspond to the values of $\{r, \theta\}$ for actively pulsating ellipses given by $r(t) = 5 + \sin \omega t$ with $\omega = 2\pi/T$ and $T = 17.98, 20.77$ for trajectories I and II respectively which are an equal amount away from the natural period, $T_n = 19.375$. Colour map corresponds to a normalised angular velocity, $\left|\dot{\theta}_n\right|$, with red/blue being fast/slow respectively. Black circles of constant r correspond to the minimum/maximum values of $r = 4, 6$ respectively. All trajectories exist within the annulus spanned by these two circles. Trajectory I exhibits asymmetry in the trajectory in the neighbourhood $\theta \approx 0$, whereas trajectory II, which is at the edge of the Arnold tongue shows almost perfect symmetry.

With the above knowledge, it is possible to compute the boundaries of the tongues, and indeed, any coordinate within the tongues using a different approach than running the full simulation for a suspension of particles as was done to generate Fig. 5.2. We may instead integrate the equation of motion to get the change in orientation over a driving period

$$\Delta\theta[T] = \int_0^T \dot{\theta}(t; T) dt + \pi, \tag{5.19}$$

with the initial condition $\theta(0) = 0$ and using $r(t) = r_0 + A \sin(\omega t + \phi_0)$, where ϕ_0 is the initial phase lag and is an input parameter. Solving $\Delta\theta[T] = 0$ for a given

A, ϕ_0 will give us the value of T that corresponds to a phase synchronised limit cycle for those parameter values. The reason for the $+\pi$ at the end is because in one cycle, θ will rotate clockwise by π (due to its nematic symmetry), making its value equal to $-\pi$ when on the synchronised limit cycle. ϕ_0 dictates where on the tongue each cycle is located and in particular, the edges of the tongue are at $\phi_0 = \pm\pi/2$, which correspond to $r = r_{max}$ and $r = r_{min}$ respectively.

Next, we consider the case where we consider the particle elongation to be a dynamical variable, *i.e.* allow it to respond to flow gradients and thermodynamic effects.

5.4 Deformable elongated particles in oscillating shear flow

In this section, we discuss the main focus of the chapter - the case of a dilute suspension of non-interacting deformable nematics subjected to an oscillating shear flow. In Sec. 5.3.1 we showed how rigid particles would *not* phase synchronise in such a flow due to the nature of the non-linear coupling that was introduced. On the other hand, in Sec. 5.3.3, we illustrated how the coupling of shape variations to the orientational dynamics is sufficient to drive phase synchronisation.

Here, we will allow both the shape variable and orientation angle of a individual particles to evolve dynamically according to their equations of motion. This will naturally lead to richer dynamics since the oscillatory flow will create periodic variations in the shape which will, in turn, couple back to the orientational dynamics. We will also delve deeper into the analysis of this system from a dynamical systems point of view, providing the mathematical context of the emergence of the Arnold tongues, the onset of global nematic order and the comparison to the case of rigid particles presented in Sec. 5.3.1.

5.4.1 Model

The model we study in this section is similar to that introduced in Sec. 5.3.1, but with a dynamical variable $r(t)$. We consider a dilute suspension of N non-interacting, deformable particles subjected to a time-dependent shear flow $\dot{\gamma}_0(1 + A\sin(\omega t))$,

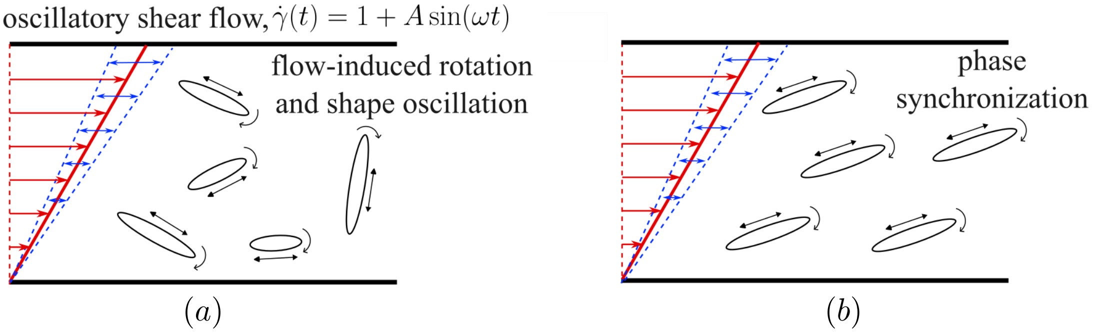

Figure 5.4: Emergence of nematic order for non-interacting deformable particles in an oscillatory shear flow. (*a*) Schematic of the system showing deformable particles suspended in a time-dependent shear flow with both a mean (red) and an oscillatory (blue) component. The initial isotropic state of random orientations $\theta_i(0)$ and varying shape parameters $r_i(0)$ develops into (*b*) a phase synchronised state at later times.

as schematically shown in Fig. 5.4 (*a*). The instantaneous state of the i^{th} particle, in two dimensions, is described by two degrees of freedom, (i) the usual shape parameter r_i, equal to the aspect ratio of the particle minus unity, and (ii) an inclination angle θ_i indicating the axis of elongation measured with respect to the flow direction. The dynamics of the i^{th} particle are described by

$$\frac{\mathrm{d}r_i}{\mathrm{d}t} = \dot{\gamma}(t)(r_i+1)\sin 2\theta_i - \frac{1}{\alpha}(r_i - r_0)\left(1 + \epsilon(r_i - r_0)^2\right), \tag{5.20}$$

$$\frac{\mathrm{d}\theta_i}{\mathrm{d}t} = \frac{\dot{\gamma}(t)}{2}\left(\beta(r_i)\cos 2\theta_i - 1\right). \tag{5.21}$$

In Eqs. (5.20)-(5.21), $\dot{\gamma}(t) = 1 + A\sin(\omega t)$, $\beta(r_i) = ((r_i+1)^2 - 1)\,/\,((r_i+1)^2 + 1)$ and time is scaled with the inverse of the mean shear rate $\dot{\gamma}_0^{-1}$. The parameter $\alpha = \dot{\gamma}_0/(\Gamma_r A_r)$ controls the strength of free energy induced shape change compared to that of the shear, ϵ describes the quartic free energy landscape and the parameter Γ_r is a relaxation rate towards the free energy minimum at $r_i = r_0$, as defined previously in Chapter 3.3.1. We numerically solve Eqs. (5.20)-(5.21) for $N = 200$ particles with random initial orientations (isotropic state). We fix $\alpha = 0.8$, $\epsilon = 0.1$ and $r_0 = 5$ in the following analysis. Additionally, while simulations are performed for individual particles, we will drop the particle label subscripts for brevity unless stated otherwise.

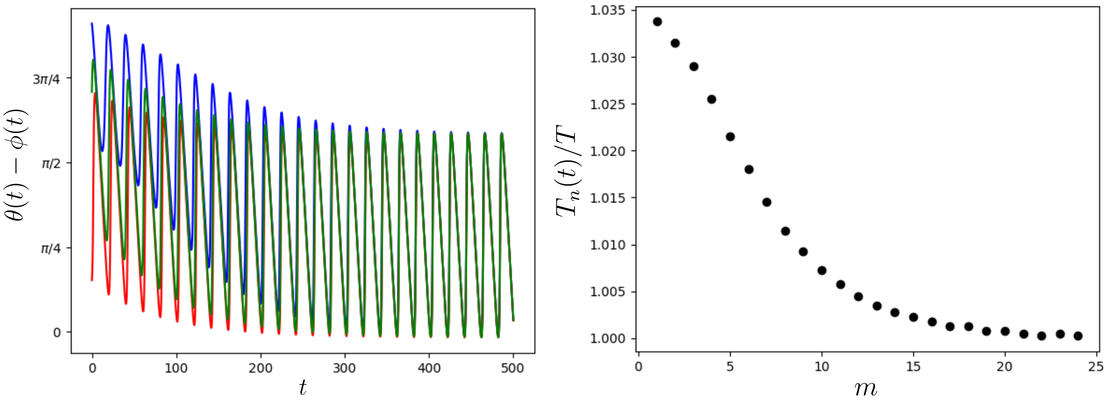

(a) (b)

Figure 5.5: Phase locking and frequency locking during synchronisation for parameter values $A = 0.5, T = 20$. (a) Phase difference between the driven oscillator of each particle and the driving oscillator, $\theta(t) - \phi(t)$, with $\phi(t) = \omega t$, as a function of time for three different initial conditions (red, blue, green). (b) Evolution of the time period of the limit cycle $T_n(t)$ scaled with the driving period T as a function of the number of driving periods m. The time period was calculated as the duration between consecutive peaks in the time series of $\theta(t)$.

5.4.2 Emergence of nematic order

Simulations show that, over time, all particles tumble in the flow at the same driving frequency ω of the imposed oscillatory shear flow. We refer to this as frequency locking. More importantly, we also find that the particles also phase lock their rotational motion with the imposed flow. This phase and frequency locking is shown in Fig. 5.5 (a) and (b), respectively. For phase locking, we see that the difference between the phase of each particle's orientation and the phase variable associated with the oscillatory driving, i.e. $\theta(t) - \phi(t)$ with $\phi(t) = \omega t$, stays bounded and converges on a unique oscillatory behavior for different particles, *i.e.* initial conditions (see Fig. 5.5 (a)). This is consistent with the general definition of phase locking where the differences between the phases should be bounded and the difference does not necessarily need to be zero or a constant value [132]. Further, from Fig. 5.5 (b), we see that the period of the orientational oscillations converges to the period of driving T with time, resulting in frequency locking.

This phase locking of each particle's orientation with the imposed oscillatory flow implies the synchronisation in the motion of all particles with each other

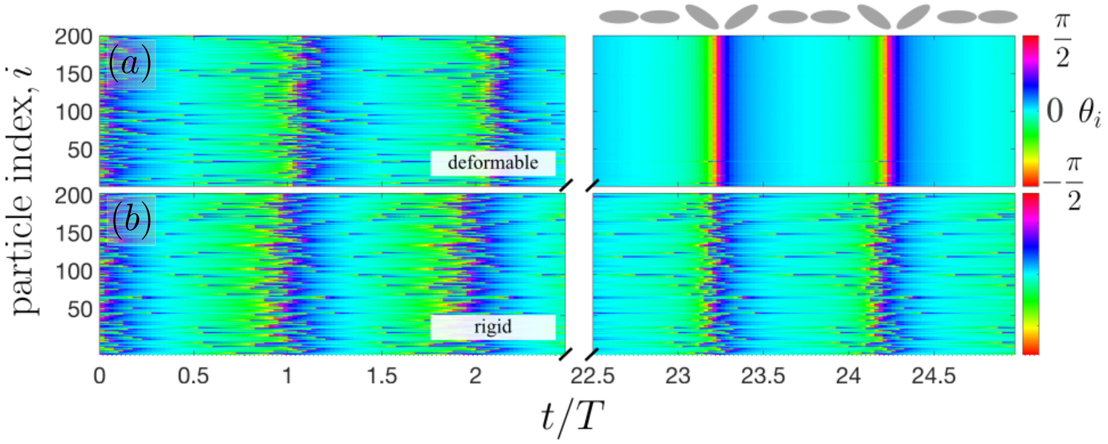

Figure 5.6: Early and late time kymographs illustrating the temporal evolution of orientation of (a) deformable and (b) rigid particles initialised with random orientations. The horizontal axis is normalised by the period of the external driving. Grey ellipses at top of (a) are a guide for particle orientation while phase synchronised. At late times, all deformable particles phase lock and develop a global nematic order. There is no phase locking observed for rigid particles. The plots are for $N = 200$, $A = 0.5$ and $T = 20$.

particle as well, and we obtain a state of collective behaviour where orientations of all non-interacting deformable particles are the same at all, sufficiently long, times ($t \gg 2\pi/\omega$). Kymographs illustrating the evolution of the orientation of particles $\theta(t)$ are shown in Fig. 5.6 (a) for early and late times. Nematic order emerges in the system as indicated schematically in Fig. 5.6 (a). The isotropy in the initial orientation of particles gradually fades away with time, and at long times the phase-synchronised state emerges with tumbling frequency ω and no variations in θ between different particles. In contrast, the kymograph obtained for rigid, elongated particles, shown in Fig. 5.6 (b) does not exhibit phase locking and the system does not develop nematic order.

To quantify the nematic order in the system, we calculate the magnitude of the nematic order parameter $S(t) = \langle \cos\left[2(\theta_i(t) - \Psi_0(t))\right]\rangle$ where $\langle\cdot\rangle$ denotes an average over N particles and $\Psi_0(t)$ is the mean orientation at time t, defined as

$$\Psi_0(t) = \frac{1}{2}\arctan\left(\frac{\sum_{i=1}^{N}\sin 2\theta_i(t)}{\sum_{i=1}^{N}\cos 2\theta_i(t)}\right).$$

The evolution of $S(t)$ for deformable particles is shown in Fig. 5.7 (black curve) which asymptotes towards unity indicating the development of permanent nematic

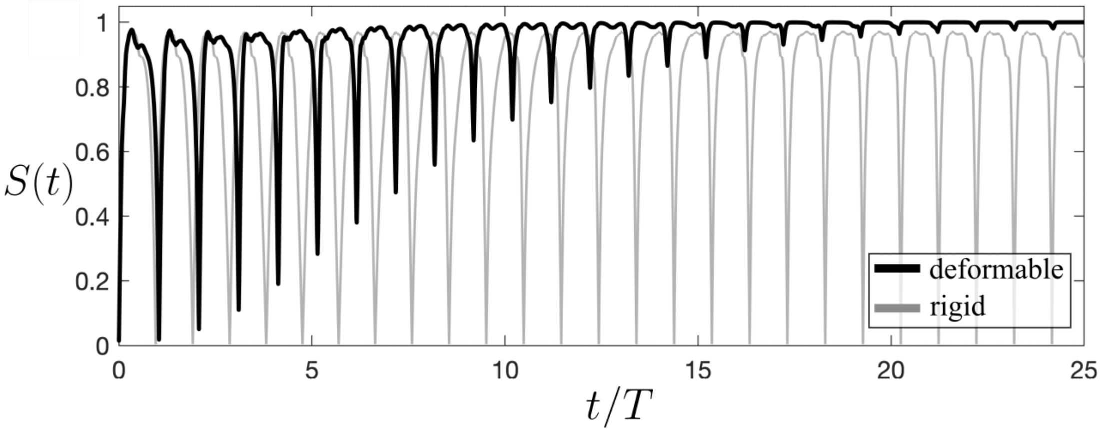

Figure 5.7: Corresponding nematic order parameter $S(t)$ for deformable (black) and rigid (grey) particles as a function of time, normalised by the period of the external driving. At long times, deformable particles develop a nematic order towards a steady state value $S \to 1$. Rigid particles show large oscillations in the measured nematic order. Periodic peaks at $S \approx 0.9$ are due to critical slowing down near the ghost region of the tumbling motion.

order in the system. The slow development of nematic order is due to the difference in time taken to phase synchronise based on initial conditions. We discuss this point further below. Conversely, the measured nematic order parameter in a system of rigid particles subjected to the same oscillatory flow (gray curve in Fig. 5.7) keeps oscillating between 0 and $\lesssim 1$. This is a qualitatively different mechanism that exhibits apparent nematic order ($S \approx 0.9$) in the case of rigid elongated particles. The difference in the dynamics arises due to the difference in the underlying physics. As discussed above, the nematic order achieved by the deformable particles is a consequence of the deformability-induced phase-locking with the imposed frequency.

On the other hand, rigid, elongated particles show transient nematic order due to their slow rotational motion at certain orientations. To elaborate, as the rigid particles tumble in the imposed shear flow and reach $\theta = 0$, that is when the rigid particles align with the flow direction, their angular velocities reduce considerably (see Eq.(5.6)). The larger the aspect ratio of the particle, the stronger is this slow down. Thus, each particle in the suspension spends longer time at $\theta \approx 0$ and this slow down in the rotational motion gives the impression that the particles have developed an orientational order (see Fig. 5.8 (e)). However, this is temporary, and

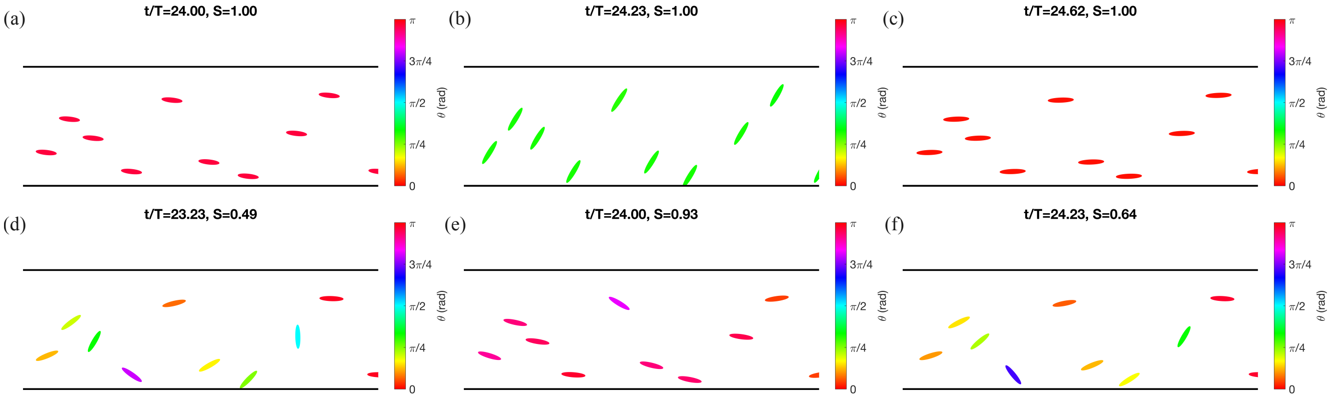

Figure 5.8: Snapshots of visualisation of simulations at long times illustrating the orientational configuration (a-c) of deformable particles, (d-f) of rigid particles. The particles are coloured according to their instantaneous orientation based on the cyclic colour bar shown. In each panel, the title shows the time of the snapshot in terms of the natural period of $T = 20$ and also the magnitude of nematic order S. Deformable particles develop a time-independent nematic order, whereas rigid particles exhibit periodical instances of 'apparent' nematic order due to slowing down of dynamics near the ghost region, corresponding to $\theta \approx 0$ configurations.

any such ordering is lost as they move away from this special direction ($\theta = 0$). Hence, the nematic order exhibited by rigid particles is only apparent and time periodic, arising from the slowing down of particles near this "ghost" region.

5.4.3 Phase synchronisation

We may use the mathematical framework introduced in Sec. 5.2 to demonstrate that phase synchronisation will arise in the system represented by Eqs. (5.20) and (5.21), where we will drop the particle labels for brevity. In terms of a dynamical system, these read as

$$\dot{\theta} = \frac{\dot{\gamma}}{2}\left(\frac{(r+1)^2-1}{(r+1)^2+1}\cos 2\theta - 1\right) = F_1(\theta, r; \dot{\gamma}), \tag{5.22}$$

$$\dot{r} = \dot{\gamma}(r+1)\sin 2\theta - \frac{1}{\alpha}(r-r_0)\left(1+\epsilon(r-r_0)^2\right) = F_2(\theta, r; \dot{\gamma}). \tag{5.23}$$

We are mainly interested in the parameter $\dot{\gamma}$ that will vary as a function of time in a time-dependent shear flow. Rewriting the system in vector notation we have

$$\dot{\mathbf{x}} = \mathbf{F}(\mathbf{x}; \dot{\gamma}),$$

where $\mathbf{x} = (\theta, r)$ and $\mathbf{F}(\mathbf{x}; \dot{\gamma}) = (F_1(\theta, r; \dot{\gamma}), F_2(\theta, r; \dot{\gamma}))$. If we now let $\dot{\gamma}(t) = 1 + A\,\sin(\omega t)$ then we perform a perturbation expansion in A assuming $A \ll 1$, and we get the following leading order equation

$$\dot{\mathbf{x}} \approx \mathbf{F}(\mathbf{x}) + A\,\mathbf{G}(\mathbf{x})\sin(\omega t),$$

where, $\mathbf{F}(\mathbf{x}) = F(\mathbf{x}; \dot{\gamma})\Big|_{\dot{\gamma}=1}$ and

$$\mathbf{G}(\mathbf{x}) = (G_1, G_2) = \left(\frac{\partial F_1(\mathbf{x}; \dot{\gamma})}{\partial \dot{\gamma}}\Big|_{\dot{\gamma}=1}, \frac{\partial F_2(\mathbf{x}; \dot{\gamma})}{\partial \dot{\gamma}}\Big|_{\dot{\gamma}=1} \right).$$

Calculating the partial derivatives gives

$$\begin{aligned} G_1 &= F_1(\theta, r), \\ G_2 &= F_2(\theta, r) + \frac{1}{\alpha}(r - r_0)\left(1 + \epsilon(r - r_0)^2\right). \end{aligned}$$

Following the previous analyses, we reduce our dynamical system from the variables (θ, r) to the phase variable ψ that changes along the limit cycle of the undriven system i.e. $\dot{\gamma}(t) = 1$, that evolves as follows:

$$\begin{aligned} \frac{d\psi(\mathbf{x})}{dt} = \omega_n &= \frac{\partial \psi}{\partial \theta}\dot{\theta} + \frac{\partial \psi}{\partial r}\dot{r} \\ &= \frac{\partial \psi}{\partial \theta}F_1(\theta, r) + \frac{\partial \psi}{\partial r}F_2(\theta, r), \end{aligned} \tag{5.24}$$

Now, the dynamics of ψ for the perturbed system can be calculated in a similar way using the leading order equations for the driven system as follows:

$$\begin{aligned} \frac{d\psi}{dt} &= \frac{\partial \psi}{\partial \theta}\dot{\theta} + \frac{\partial \psi}{\partial r}\dot{r}, \\ &= \omega_n + A\left(\frac{\partial \psi}{\partial \theta}G_1 + \frac{\partial \psi}{\partial r}G_2\right)\sin(\omega t), \\ &= \omega_n + A\,S(\psi)\sin(\omega t). \end{aligned} \tag{5.25}$$

Note that in the above, the terms on the right hand side are calculated on the limit cycle of the non-oscillatory driven system [133]. Here

$$\begin{aligned} S(\psi) &= \frac{\partial \psi}{\partial \theta}G_1(\theta, r) + \frac{\partial \psi}{\partial r}G_2(\theta, r), \\ &= \frac{\partial \psi}{\partial \theta}F_1(\theta, r) + \frac{\partial \psi}{\partial r}F_2(\theta, r) + \frac{\partial \psi}{\partial r}\frac{1}{\alpha}(r - r_0)\left(1 + \epsilon(r - r_0)^2\right), \\ &= \omega_n + S_1(\psi), \end{aligned}$$

with

$$S_1(\psi) \equiv \frac{\partial \psi}{\partial r}\frac{1}{\alpha}(r - r_0)\left(1 + \epsilon(r - r_0)^2\right).$$

By integrating Eq. (5.25) for ψ over one period of the driving $T = 2\pi/\omega$ we obtain the circle map

$$\psi_{k+1} = \psi_k + 2\pi\frac{\omega_n}{\omega} + A\, f(\psi_k), \tag{5.26}$$

where $f(\psi_k) = \int_{kT}^{(k+1)T} S_1(\psi)\sin(\omega t)dt \neq 0$. The system will therefore exhibit phase synchronisation under the right parameter values due to the additional non-linearities introduced by the coupling of shape and orientation.

5.4.4 Dynamical Analysis

Eqs. (5.20)-(5.21) constitute a non-autonomous dynamical system due to the time-dependentwwww driving $\dot{\gamma}(t)$. The trajectories in this two-dimensional state space may cross (at different times) giving rise to ambiguity and an incomplete description of the system. Hence, we convert the system to an autonomous dynamical system by introducing the new phase variable that is common for all particles, as in Sec. 5.4.2 $\phi_i = \phi = \omega t$ or,

$$\frac{\mathrm{d}\phi}{\mathrm{d}t} = \omega, \tag{5.27}$$

with $\phi(t + 2\pi/\omega) = \phi(t)$, which results in Eqs. (5.20), (5.21) and (5.27) forming an autonomous 3D dynamical system for each individual particle and allows us to pursue a state-space analysis.

A subset of the complete 3D state-space formed by variables r, θ, ϕ for a single deformable particle can be represented as the inside of a torus with ϕ the toroidal angle, 2θ the poloidal angle and r the smaller radius of the torus as shown in Fig. 5.9. In the synchronised state we find that N different initial conditions corresponding to N particles converge to a stable limit cycle orbit that lies inside the torus (the cyan curve). Furthermore, along the limit cycle all N trajectories converge to the same point at any given time.

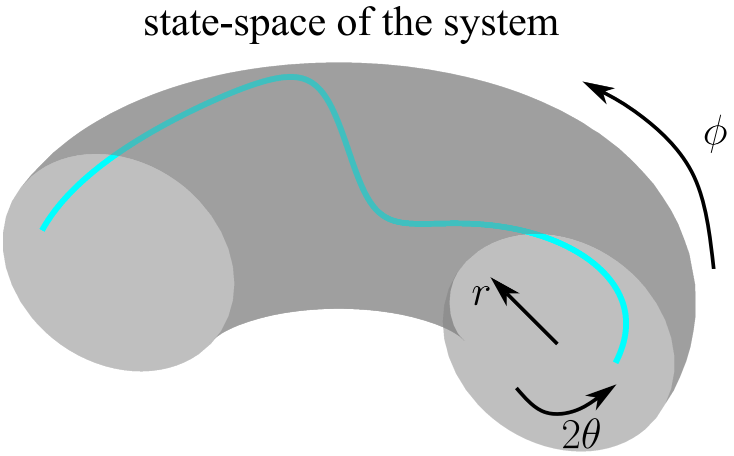

Figure 5.9: Schematic of the 3D state-space represented by a torus - driving phase ϕ as the toroidal angle, particle orientation 2θ as the poloidal angle and particle shape parameter r as the smaller radius. All trajectories starting from any initial condition, *i.e* position in the state space converge to the cyan curve, the synchronised limit cycle.

This is better illustrated in Fig. 5.10 (a) where the azimuthal projection of the torus on to a polar plane formed by $(r, 2\theta)$ is shown. The N trajectories not only converge to the projected limit cycle (cyan curve) but also to the same point (black dot) at a given time indicating phase synchronisation.

The focusing of state-space trajectories onto a point on the limit cycle can be understood as follows. All trajectories in state-space rotate at the same angular velocity $\frac{\mathrm{d}\phi}{\mathrm{d}t} = \omega$ around the torus. This implies that N random initial conditions which start at the same initial time (say, $\phi(0) = 0$) must occupy the same instantaneous cross-section of the torus – the polar plane formed by r and 2θ, at any future time $\phi(t)$. Since the state-space trajectories must eventually converge onto the stable limit cycle that wraps around the torus, there is only one point along the limit cycle at each cross-section, and hence all trajectories will converge towards this point on the limit cycle in each cross-section. This process may be contrasted with a system subjected to a steady shear flow, *i.e.,* $A = 0$. Again, all particles deform and tumble, the trajectories converge to a limit cycle orbit (red curve in Fig. 5.10 (b)) with period T_n but, since the oscillatory shear is absent, the deformable particles occupy different points along the limit cycle at any given

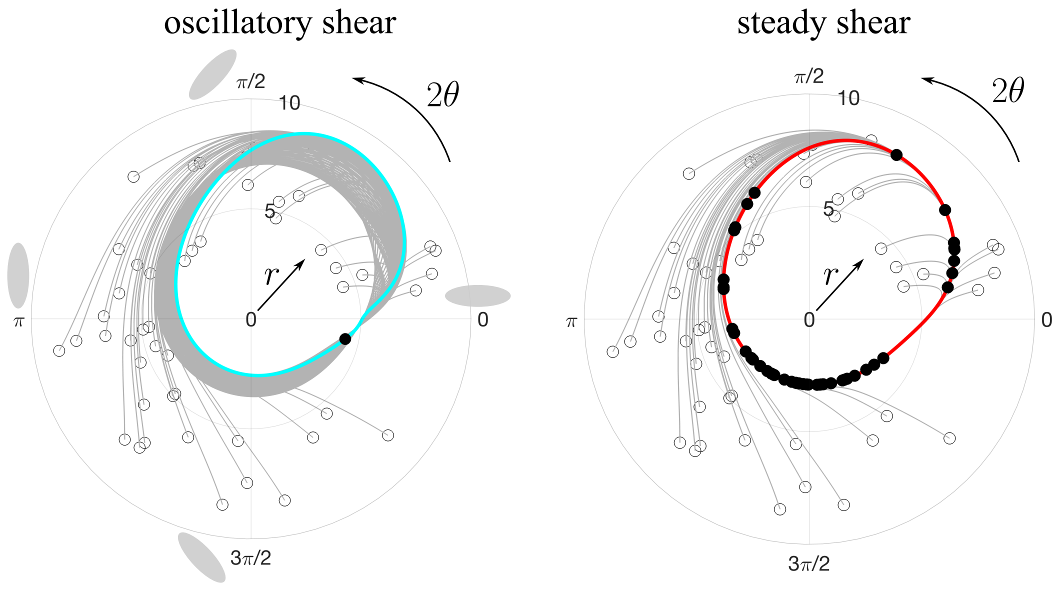

(a) (b)

Figure 5.10: Projection of the toroidal state space given in Fig. 5.9 onto the $(r, 2\theta)$ polar plane for a system subjected to (a) oscillatory shear $(A \neq 0)$ and (b) steady shear $(A = 0)$. Random initial conditions (open circles) converge to a point (filled circle) on the limit cycle (cyan) in (a), but they converge at different phases on the limit cycle (red) in (b).

time (black filled circles) *i.e.* their orientations $\theta_i(t)$ and shape $r_i(t)$ are different. Hence, deformable particles subjected to a steady shear do not phase synchronise and consequently develop no nematic order.

We may develop a better understanding of the transient dynamics of phase synchronisation by plotting trajectories on the $(r, 2\theta)$ cross-section of the torusat three different times, $t = 0$ (black open circles), $t = T$ (yellow filled circles) and $t \gg T$ (black filled circles), as shown in Fig. 5.11. The initial, randomly distributed points, first, rapidly converge onto the limit cycle of the non-oscillatory system (red curve) and, subsequently, migrate along this limit cycle and converge onto a stable point (green point), which lies on the actual, stable limit cycle of the oscillatory system (cyan curve). In other words, at short times the system behaves effectively like a non-oscillatory system and state space trajectories rapidly converge onto a ‘ghost’ orbit. At long times, spanning multiple driving periods, the oscillatory driving leads to phase synchronisation. Accompanying the stable limit cycle, the unstable limit cycle appears as an unstable point (pink cross) that repels the state-space trajectories in this plot.

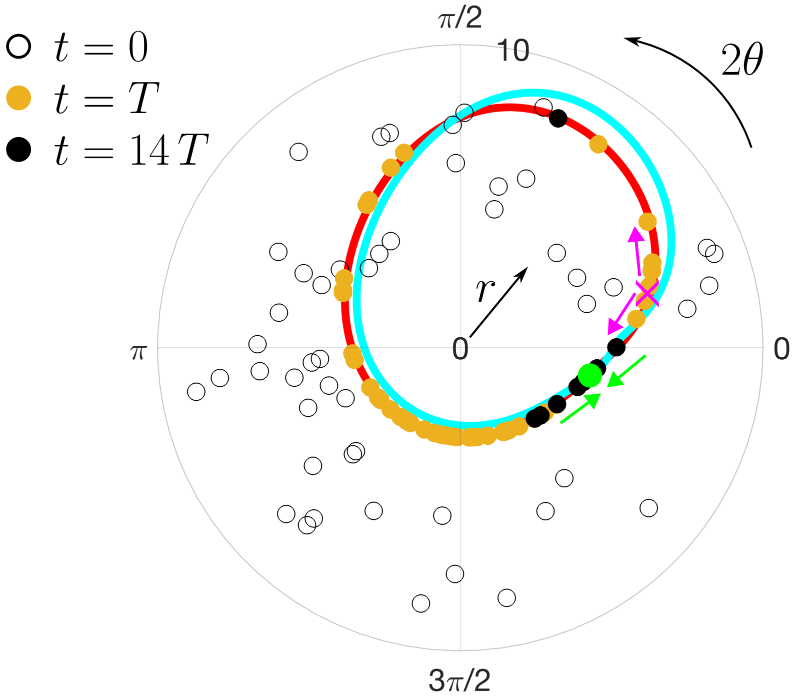

Figure 5.11: Transient dynamics in state-space. Snapshots of trajectories in the state-space as points while passing through the $(r, 2\theta)$ cross section of the torus at three different times. At $t = 0$, random initial conditions (open circles); at $t = T$, trajectories converged to the limit cycle of the steady shear system (yellow filled circles on the red curve); and at $t = 14T$, trajectories (black filled circles) converging onto the stable point (green filled circle with incoming arrows) that lies on the limit cycle of the oscillatory system (cyan curve). The unstable point (pink cross with outgoing arrows) corresponds to the unstable limit cycle in the full state-space.

5.4.5 Physical Mechanism

Fig. 5.12 (a) shows the range of amplitude, A, and oscillatory driving period, T, for which phase synchronisation occurs. The synchronisation regions (violet) occur periodically in bands near multiples of T_n, the natural time period of tumbling in a steady shear flow ($A = 0$). These structures are the Arnold tongues [133] we have discussed previously and they come in and out of existence in parameter space via a saddle-node bifurcation of cycles in state space. To illustrate this, consider a fixed value of $A = 0.5$ and traverse the primary Arnold tongue shown in Fig. 5.12 (a) horizontally in the parameter space towards larger T (with $T_n \approx 20.02$). At the

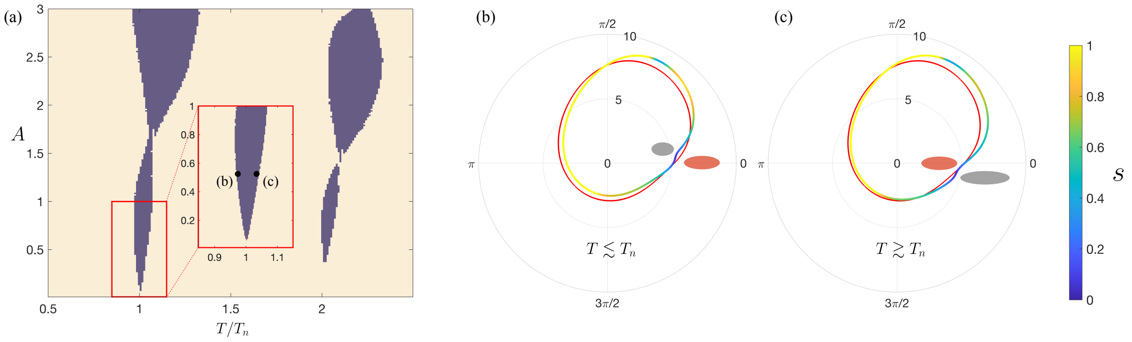

Figure 5.12: (a) Arnold tongues: regions of phase synchronisation induced nematic order (violet) in the (A, T) parameter space. The inset shows the expanded view of the first tongue. $(b) - (c)$ Limit cycles in $(r, 2\theta)$ projection of the state-space, corresponding to two points marked in (a): $T = 19.5 \lesssim T_n$ in (b) and $T = 20.7 \gtrsim T_n$ in (c). The color on the limit cycle denotes the state-space speed $s = \sqrt{(dr/dt)^2 + (d\theta/dt)^2}$. In each figure, the limit cycle for the case of steady shear ($T_n \approx 20.02$) is plotted in red. The grey and red ellipses illustrate the aspect ratio of the deformed particle (not to scale) as they pass through the ghost region (near the orientation $\theta = 0$) in the oscillatory and in the steady shear flow respectively. Compared to particles in steady shear, in (b) particles reduce their anisotropy as they pass through the ghost region to reduce their period. Conversely, in (c) particles increase their anisotropy to increase their period.

onset of the synchronisation region, a pair of stable and unstable (saddle) limit cycles are born that appear as a stable (green circle) and an unstable (pink cross) point in the 2D polar $(r, 2\theta)$ section of the state-space shown in Fig. 5.13 (a) for $T = 19.5$. Increasing T further inside the tongue results in the pair of stable and unstable points moving away from each other along the limit cycle (red) of the non-oscillatory ($A = 0$) system (see Fig. 5.13 $(b) - (c)$). At even larger T as one approaches the other end of the tongue, the two fixed points approach each other again on the limit cycle, as shown in Fig. 5.13 (c) for $T = 20.78$, and annihilate each other. Thus, the periodic appearances of the Arnold tongues near multiples of the natural period of the limit cycle T_n are facilitated by these saddle-node bifurcations of limit cycles.

The finite width of the tongues can be physically rationalised by analysing the extent to which a deformable particle can modulate the rate of tumbling and shape changes to match the driving period T of the oscillatory shear. For example, within the primary Arnold tongue in Fig. 5.12 (a), the particle decreases (increases) its tumbling period on the limit cycle when $T < T_n$ ($T > T_n$) by suitable shape deformations. For the tumbling dynamics, since the particle spends most of its

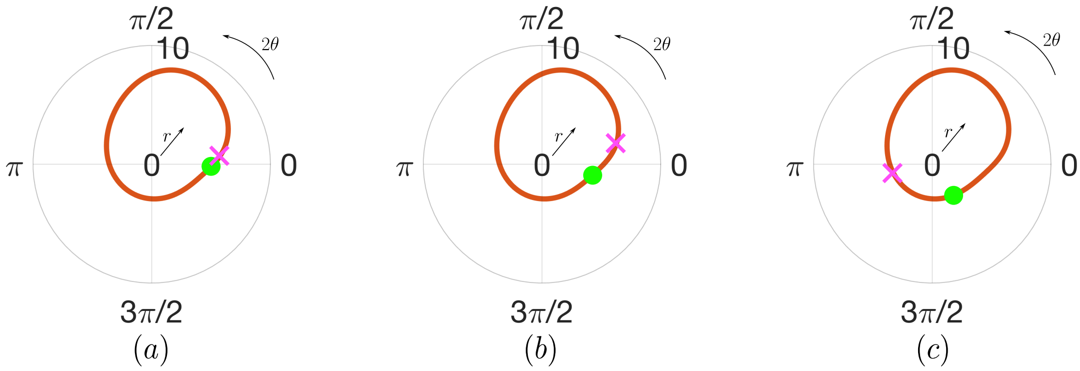

Figure 5.13: Two-dimensional $(r, 2\theta)$ section of the state-space showing (a) the birth of stable (green circle) and an unstable (pink cross) points via a saddle-node bifurcation on the limit cycle (red) of the non-oscillatory system $(A = 0)$ near $T = 19.5$. (b) These fixed points spread on the limit cycle near the middle of the tongue $(T = 20)$ and (c) then annihilate again in a saddle-node bifurcation at the other end of the tongue $(T = 20.78)$.

time near the $\theta = 0$ ghost region [153], the shape modulations near this orientation have the most significant contribution to the tumbling period. This modulation is illustrated in Fig. 5.12 (b) & (c) for $T < T_n$ and $T > T_n$ respectively.

In these figures, the limit cycle is coloured to denote the state-space speed $s = \sqrt{(dr/dt)^2 + (d\theta/dt)^2}$. The limit cycle for the non-oscillatory system (red curve) is also plotted for comparison.

We can see in Fig. 5.12 (b) that compared to that of the non-oscillatory system, the oscillatory system reduces its shape parameter r near the orientation $\theta = 0$. The reduced elongation of the particle helps it traverse the ghost region faster and thus to reduce the period of the limit cycle.

Similarly, the limit cycle in Fig. 5.12 (c) has r increased in order to traverse the ghost region slower and thus increase the period of the limit cycle. Hence, by appropriately modulating the shape near the ghost region, the particle matches the period of the limit cycle with the imposed oscillation period. Recalling the discussion in Sec. 5.3.3, we may understand that it is the extent of the particle's ability to achieve this that sets the finite width of the Arnold tongues, and is related to the time evolution equation of the shape variable, and the system parameters.

Time taken to synchronise

Given the discussion in Sec. 5.4.5, we may now understand the delay in the time taken for the establishment of the global nematic order discussed in Sec. 5.4.2. Although synchronisation is achieved for all particles within the Arnold tongues for sufficiently long time, *i.e.* all different initial conditions in our phase space representation, as $t \to \infty$, the amount of time it takes to phase synchronise can vary depending on the initial conditions. This is because, phase synchronisation in state space corresponds to converging onto the stable limit cycle where another unstable (saddle) limit cycle also exists. Hence, if an initial condition in state space is near a stable limit cycle, then it can quickly converge onto this cycle. Conversely, an initial condition near the unstable limit cycle may take a long time to converge onto the stable limit cycle.

This contrast in the time taken to converge onto the stable limit cycle is depicted in Fig. 5.14 where we have plotted the number of driving periods (colour map) required to phase-synchronise based on different initial conditions $\theta(0)$ and $\phi(0)$ for a fixed $r(0) = r_0 = 5$. It can be seen that the convergence is quicker along black regions that correspond to initial conditions that can quickly approach the stable limit cycle. Conversely, convergence is slower along white regions that correspond to initial conditions that are likely to be in the vicinity of the unstable limit cycle. Thus, the slow development of the nematic order in phase-synchronised regions, as shown in Fig. 5.7, can be attributed to initial conditions that start near the unstable limit cycle in state space and take a long time to converge onto the stable limit cycle.

Next, we consider two other interesting cases of a system of a dilute suspension of deformable particles and finally a continuum model for a dense suspension.

Shear flow with a large oscillatory component

In this section, we have mainly focused on phase synchronisation in the regime where $A < 1$, *i.e.* the oscillatory component of the shear flow is smaller than the mean steady shear rate. Here, we show that even for $A > 1$, synchronised regions persist and interestingly, we obtain time-periodic states that undergo a more

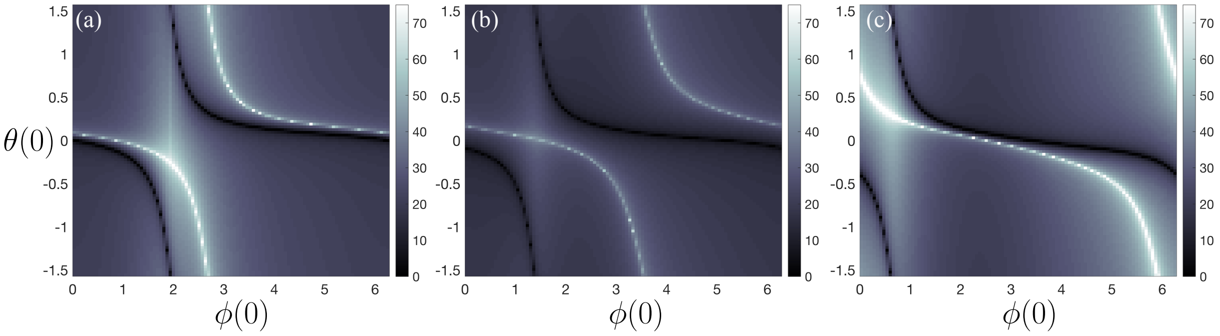

Figure 5.14: Time taken for phase synchronisation based on initial conditions $\phi(0)$ and $\theta(0)$ for a system of deformable particles in an oscillatory shear flow. Plots are shown for $A = 0.5$, $r(0) = r_0 = 5$ with (a) $T = 19.5$, (b) $T = 20$ and (c) $T = 20.7$. Colour labelling corresponds to number of periods taken for synchronisation.

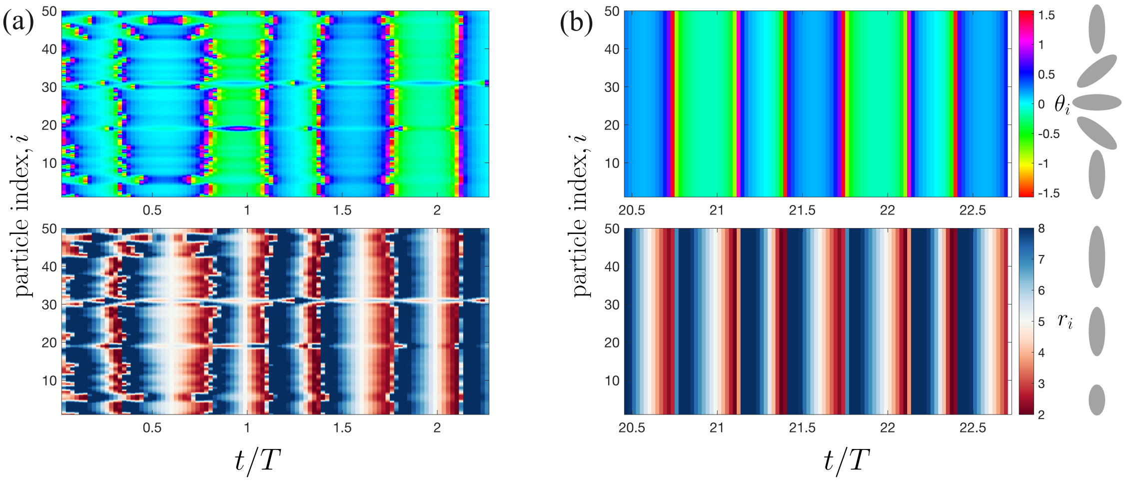

Figure 5.15: Phase synchronisation of deformable particles in time-dependent shear flow where the oscillatory flow component is larger in magnitude compared to the steady flow component i.e. $\dot{\gamma}(t) = 1 + A\sin(\omega t)$ with $\omega = 2\pi/T$ and $A > 1$. We use the parameters as $A = 3$ and $T = 22$ with $N = 50$ different initial conditions. Plots show evolution at (a) early times and (b) late times of orientation θ_i (top) and shape parameter r_i (bottom) for each independent particle (*i.e.* each initial condition).

complex oscillation mode in the synchronised phase with a mixture of tumbling and back-and-forth oscillations. An example is shown in Fig. 5.15 where kymographs of the orientation $\theta_i(t)$ and shape parameter $r_i(t)$ for $N = 50$ particles are shown at early and late times in panel (a) and (b), respectively. We find that for the parameter values corresponding to Fig. 5.15, we obtain a mixed mode composed of one tumbling and one back-and-forth orientational oscillation.

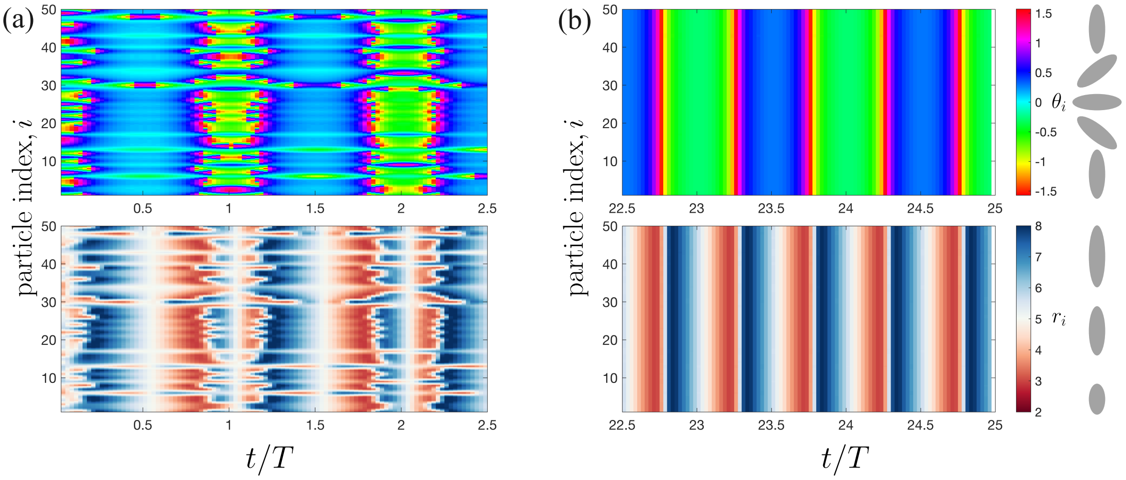

Figure 5.16: Phase synchronisation of deformable particles in an oscillating shear flow with no mean flow i.e. $\dot{\gamma}(t) = A\sin(\omega t)$ with $\omega = 2\pi/T$. We use the parameters as $A = 1$ and $T = 20$ for no mean flow and $N = 50$ different initial conditions. Plots show evolution at (a) early times and (b) late times of orientation θ_i (top) and shape parameter r_i (bottom) for each independent particle (i.e. each initial condition).

Shear flow with zero mean

We also find phase synchronisation in completely oscillatory shear flow without any mean flow component *i.e.* $\dot{\gamma}(t) = A\sin(\omega t)$. An example with kymographs is shown in Fig. 5.16 for $A = 1$ and $T = 20$. Here, instead of the particle undergoing any tumbling motion, we find a pure back-and-forth orientational oscillations which are synchronised to the driving oscillating shear.

Continuum model of deformable nematic particles

The results presented in this chapter can also be extended to a dense suspension of nematic particles, described by the continuum theory of nemato-hydrodynamics. In a one-dimensional channel setup (along the y co-ordinate) with simple shear flow having shear rate $\dot{\gamma}$; the equations of motion reduce to the following:

$$\begin{aligned} \dot{\theta} &= \frac{\dot{\gamma}}{2}\left(\lambda_0\frac{(r+1)^2-1}{(r+1)^2+1}\cos 2\theta - 1\right) + \Gamma_\theta K_0\frac{\partial}{\partial y}\left[\left(\frac{r}{1+r}\right)^2\frac{\partial\theta}{\partial y}\right], \\ \dot{r} &= \dot{\gamma}(r+1)\sin 2\theta - \Gamma_r A_r(r-r_0)\left(1+\epsilon(r-r_0)^2\right) - \Gamma_r K_0\frac{r}{(1+r)^3}\left(\frac{\partial\theta}{\partial y}\right)^2. \end{aligned} \tag{5.28}$$

Here r and θ represent averaged quantities *i.e.* averaged shape deformation and average orientation, respectively, of a collection of deformable nematic particles in some localized region. The parameter λ_0 is a flow aligning scale determining the effects of fluid flow on the dense suspension, and the parameter K_0 is an elastic constant penalizing gradients in nematic orientation. The dynamical system in Eq. (5.28) results in nematic order due to the terms $\propto K_0$ which smooth out variations in the nematic orientation. These terms capture the effects of microscopic interactions between nematic particles.

If we allow the shear rate to be time-dependent in this continuum model *i.e* $\dot{\gamma}(t)$, then one obtains different behaviours depending on K_0. For high temperatures when the system is in an isotropic state, K_0 is very small, the Eqs. (5.28) are the same as that for individual particles in the main text with the extra parameter λ_0. Hence, all our results for phase-synchronisation still hold in this limit. In fact, in the case where $\lambda_0 > 1$ synchronisation is enhanced as it exacerbates the critical slowing down in the ghost region. This is because of a separate, saddle-node infinite period (SNIPER) bifurcation of the limit cycle, that takes place at $r \to \infty$ for individual particles, and was therefore irrelevant in our previous analysis, occurs for a finite r value in the continuum description. In the regime where the nematic elasticity K_0 is comparable to the shear driving, the system encounters two effects simultaneously - the time-dependent shear driving trying to synchronise the particles through the phase synchronisation mechanism and the nematic elasticity K_0 trying to smooth out orientational order of the particles. While both of these effects would independently drive nematic ordering along the channel width, preliminary results suggest that the difference in the physical mechanisms by which they would achieve this may result in a competition between them, and may in fact hinder the emergence of nematic order.

5.5 Summary

Motivated by natural systems which exhibit synchronised behaviour, in this chapter we introduced the well known mathematical framework of phase synchronisation and, along with numerical simulations, applied it to several systems of interest. First, we showed through analytical arguments based on the literature of phase synchronisation that a dilute suspension of rigid, nematic particles in an oscillating shear flow will not phase lock with each other and will therefore exhibit no phase synchronisation. On the contrary, we have found that introducing an oscillating chiral activity instead of an oscillating shear flow creates regions of synchronisation, known as Arnold tongues, which depend on the amplitude and frequency of the oscillatory behaviour. The contrasting results between these two systems allowed us to conclude that a key element in the determination of whether a system will phase synchronise is the nature of the non-linearity associated with the external driving or activity.

We followed this up by considering elongated nematic particles subjected to a constant shear flow, but which instead experience active shape oscillations. This was relevant in understanding how the dynamics of the shape of particles may allow for the particles to modulate the period of their limit cycles and drive phase synchronisation. We found that, at the edges of the associated Arnold tongues, the shape is maximised/minimised near the ghost region of the limit cycles to most efficiently slow down or speed up the period, respectively. This gave us a physical understanding on the limits of the regions of synchronisation in the parameter space.

We then considered the more complex system of deformable nematic particles in an oscillating shear flow. We found that, since each particle individually phase locked to the external driving by modulating their shape as they tumbled in the shear flow, a steady, global nematic order emerged for long enough times. This was contrasted with the case of rigid particles where only an apparent nematic order emerged due to the critical slowing down near the ghost region of the limit cycle. An analytical analysis based on the mathematical formulation of phase synchronisation also supported our findings

The additional degree of freedom associated with the time evolution equation of the shape variable allowed us to pursue a richer dynamical systems analysis. By treating time as a periodic phase variable, we formed a 3-dimensional state space description. We showed that, for a range of driving parameters, the trajectories in this state space would necessarily converge onto one limit cycle, *i.e.* the trajectory whose period was synchronised with that of the external driving. The physical mechanism by which this occurred, and consequently the emergence of the Arnold tongues in the parameter space was linked to the ability of the particles to modulate their shape so as to change their period of oscillation. This manifested as a saddle-node bifurcation in the state space at the edges of the tongues.

The table below summarises the main results of the chapter and the physical intuition behind them. Mathematically, the physical mechanisms correspond to the non-linear terms in the governing equations.

	Rigid	Shape fluctuations	Deformable
Phase synch.	No	Yes	Yes
Physical mechanism	N/A	Period modulation	Shape-director coupling

Table 5.1: Summary of the three main cases discussed throughout the chapter. In each case, the non-linearities dictate whether the system will achieve phase synchronisation.

Finally, we briefly discussed two other cases; one where the amplitude of the oscillatory shear flow dominated over that of the steady, mean flow and that of precisely zero mean flow. Both cases resulted in phase synchronisation and therefore the emergence of global nematic order, but with qualitatively different dynamics.

Recalling that the results presented in this chapter hold for non-interacting particles, we have shown that nematic order may be established in systems without the need of thermodynamic interactions. Such situations may be relevant for active particles undergoing shape deformations [149–152] or in general when the active particles are undergoing periodic modulations in an internal state. Hence, the work in this chapter may open up new avenues to explore at the intersection of non-linear dynamics of synchronisation and soft, active matter and the emergent phenomena associated with large-scale nematic order.

6

Discussion

In this thesis, we introduced the theory of nemato-hydrodynamics which describes liquid crystals which display liquid-like positional disorder, but also show long-range orientational order. In these models, a symmetric, traceless tensorial order parameter describes the magnitude and direction of alignment of particles, which are assumed to be in a highly dense state. In a passive system, we illustrated how thermodynamic contributions associated with a free energy may induce long-range nematic order in the system. We then showed how this model may be extended in the case of active particles that consume energy from their surroundings in order to do mechanical work. This was modelled by adding a dipolar contribution to the stress tensor of the nematic fluid.

We then introduced a minimal extension to the traditional nemato-hydrodynamic models to account for the variations in shape of deformable particles, such as epithelial cells or soft colloids. By assuming that the constituent particles that make up a nematic have an elliptical shape, we defined a new dynamical variable, their aspect ratio to quantify the degree of their elongation. By considering physical arguments, we coupled the dynamics of the shape of particles to that of the orientational dynamics, described by the nematic tensor. We explored the various consequences of our model of deformable nematics in driven and active systems and contrasted the resulting dynamics to those of traditional models. Finally, we considered how a dilute suspension of deformable particles may form global nematic order when under oscillatory driving.

We summarise the main findings of each chapter in Sec. 6.1. Finally, we conclude by highlighting open questions and future directions in further understanding the effects of shape variations in a general framework in Sec. 6.2.

6.1 Summary

Chapter 3

In Chapter 3, we introduced a minimal extension to the nemato-hydrodynamic equations to incorporate large variations in the shape of the constituent nematic particles, as is typical in biological systems such as the MDCK cell line [8, 9], and in artificially created systems such as soft colloids and vesicles [5–7].

We achieved this by motivating a simple equation for the aspect ratio of particles, which we then coupled back to the orientational dynamics and, in turn, the flow field. Then, to illustrate and study the emergent dynamics that our model of deformable nematics shows, we considered the case of passive, deformable particles subjected to simple channel flows, namely Couette and Poiseuille flows. By using both analytics and numerical simulations, we found that the coupling between particle shape and orientation creates a re-orientation mechanism which in turn results in qualitatively striking dynamics compared to the theories of rigid particles.

The analysis of Couette flow showed how the system of deformable particles may settle into two different phases, depending on the applied shear rate. These are (i) a dynamical, periodic state of oscillating shape and tumbling orientational dynamics, and (ii) a flow-aligned, steady state at a constant value of the aspect ratio of particles and orientation angle. These phases were separated by a sequence of saddle-node and homoclinic bifurcations in the phase space of the parameters. Indeed, for a range of parameter values, we observed a bistable regime, where the initial conditions of the system determined which state the system would finally settle in.

We then investigated Poiseuille flow where the gradients in the flow field created spatial variations in both the shape and orientational dynamics of the particles.

Therefore, the nematic elasticity of the particles, associated with a free energy cost of variations in the director field, played a significant role in determining the final state of the system. For low values of the nematic elasticity, the system behaved similarly to a Couette flow, with a space dependent, effective shear rate which was larger near the walls of the channel, and smaller at the centre. Consequently, we found that particles near the walls would reach the flow-aligned steady state, whereas particles near the centre would exhibit shape oscillations and tumbling dynamics. Our results showed that intermediate values of the nematic elasticity led to dynamical multi-stable phases of regions where particles that would have otherwise flow aligned instead exhibit shape oscillations and vice versa. Finally, for large values, the entire system settles into a steady state of flow-alignment and elongation. With pressure-driven microfluidic experiments becoming increasingly popular for studying deformations of soft particles [154–156], our results in this chapter lend themselves to experimental verification which may serve as a check of the model we have introduced.

Chapter 4

In Chapter 4, motivated by biological systems such as the MDCK cell line, we extended the results of the previous chapter by considering the model of deformable nematics in a bulk active system with periodic boundary conditions. By considering the flows generated by an extensile active nematic, we first illustrated how the re-orientation mechanism, which is unique to deformable nematics alters their behaviour in extensional flows depending on the director field's orientation relative to the axis of the flow. When the orientation of elongated particles is close to the extensional axis, they will align with it while maintaining their anisotropic shape. On the other hand, if the particles are oriented close to the compressional axis, they will be compressed to a circular shape, and subsequently re-elongate along the extensional axis. While the result of both cases is the same, the mechanism is clearly distinct.

Then, by performing a linear stability analysis on a system of inherently isotropically shaped particles, we showed that there is an activity threshold required in order to maintain sufficient elongation and, in turn, drive nematic order and large-scale tissue flows. The key difference between our model and that of rigid active nematics [27] is that the shape dependence of the flow-aligning parameter makes its contributions to inducing nematic order a higher order effect. This means that the nematogens need to first be elongated sufficiently before flow-induced nematic order may be established. The resulting activity threshold is thus a result of a lower order effect where the active forcing that promotes elongation competes with the energy cost of deforming them from their circular shape. This result is physically motivated since only once particles become anisotropic in shape will they tend to flow-align.

We followed this up by considering the case when the activity is sufficiently large that the system transitions to fully developed active turbulence, characterised by chaotic flows and motile topological defects. Numerical simulations showed rich spatio-temporal behaviours, where domains of elongated particles with high nematic ordering and active forcing coexisted with quiescent regions of isotropically shaped particles. By sketching a mechanism of how the nematic domains of elongated particles eventually suppress gradients in their own orientational field, causing the active forces to dissipate, we argued that the particles would eventually contract to circular. Meanwhile, the chaotic nature of the flow field and its gradients caused previously isotropic regions to elongate, thus creating a dynamical steady state where these domains keep exchanging roles. We highlighted that this is a striking difference in the qualitative results of our model of active, deformable nematics when compared to that of rigid particles.

Finally, we studied how simulation parameters which correspond to measurable quantities such as the magnitude of activity or the elasticity of particles in the system affect its dynamical state and the associated length-scales. Our results showed that the typical spacing between topological defects in fully developed active turbulence displayed a dependence on both the active length-scale, but also a new, model dependent length-scale which controlled gradients in the elongation of particles. The scaling found here is once again in contrast to that of traditional active nematic theories, where the spacing between defects depends only on the active length-scale.

The predictions of our model presented in this chapter may be tested in large cell monolayers which exhibit extensile stresses at a coarse-grained level such as the MDCK cell line. By taking measurements of the cell shapes, qualitative phenomena such as the co-existence of regions of isotropically shaped and elongated particles, as well as quantitative results such as the distribution and evolution of the shape of the cells would be a major step in verifying the validity of the model.

In summary, the results of this chapter illustrated how our minimal extension of the traditional nemato-hydrodynamic models introduces qualitatively different dynamics with new physics that were not being taken into account previously. Furthermore, our model lends itself to verification through experimental measurements of the aspect ratio of cells in an extensile monolayer.

Chapter 5

Finally, in Chapter 5 we deviated from the continuum description of highly dense, deformable nematics, and instead considered a dilute regime of non-interacting particles. In particular, we studied systems subjected to time-dependent, oscillatory driving.

To this end, we first introduced the mathematical tools from the literature of phase synchronisation. For small amplitudes of an oscillatory driving, a dynamical system which naturally displays periodic motion in the form of a limit cycle may become “frequency locked” to the period of the driving. Furthermore, the dynamical variable may also “phase lock” with the phase variable of the driving. In this case, the two are considered phase synchronised [133]. Consequently, many dynamical variables that respond to the driving in the same way will inevitably also phase synchronise with each other, and, in the case of particles considered in this chapter, lead to a global nematic order.

This concept was made more concrete by considering some pedagogical examples such as elongated, rigid particles in an oscillatory shear flow, and ones in a steady shear flow but with an oscillating chiral activity. We found that phase synchronisation cannot occur under any conditions for the former, whereas for the latter it is possible, depending on the amplitude and frequency of the shape oscillations. The regions in the parameter space where phase synchronisation is achieved are referred to as Arnold tongues in the literature. The comparison of these systems suggested that the nature of the coupling between the periodic driving and the internal degrees of freedom of a system is an important ingredient in determining whether phase synchronisation is achievable.

To study whether the introduction of deformability was sufficient to cause phase synchronisation, we followed this up by considering a system of elongated particles in a steady shear flow which exhibited active shape oscillations around a mean value of their elongation. We found that this system did exhibit phase synchronisation, while also providing an understanding of the physical mechanism involved. The modulations of the shape of particles tend to slow down, or speed up the orientational dynamics through a non-linear coupling effect, such that the period of the natural (unperturbed) limit cycle of the system matches that of the external driving.

Finally, we considered the case of deformable nematic particles in an oscillatory shear flow. Our results showed that phase synchronisation between non-interacting particles was possible, leading to the emergence of a global nematic order. This was a direct consequence of the non-linear coupling between shape and orientational dynamics. Mathematically, a dynamical analysis of the system showed that the existence of the Arnold tongues was linked to a saddle-node bifurcation which was a consequence of the creation and annihilation of saddle/stable points in the space of limit cycles. Physically, this depended on the extent of the ability of the deformable particles to modulate their shape so as to drive the period of their natural limit cycle towards that of the oscillatory driving.

Our results in this chapter provided a different avenue for the emergence of nematic order, rooted in the nature of periodic variations of different degrees of freedom in a system, and not necessarily linked with thermodynamic interactions.

6.2 Outlook

In this thesis, we have introduced a model that incorporates deformability into the nematic equations and touched upon some of the implications of modelling biological tissues as deformable active nematics. We have also considered different cases where particles are subject to external driving, rather than active forcing. However, there are still many open questions which are yet to be answered. Some important examples include:

Can a tensorial model of shape provide a more complete description of the dynamics of cells?

There has been recent work on the development of a tensorial order parameter that quantifies the degree and orientation of elongation of cells [157], coupled to a nematic, **Q**-tensor model which describes the dynamics of the rigid active filaments within cells. An open question is the reconciliation between the qualitative dynamics observed between our model of deformable nematics which introduces a separate scalar variable to model the shape, and tensorial models where the shape is represented by the corresponding scalar order parameter. For instance, when considering a simple system such as an imposed shear flow, shape oscillations are not observed in such tensorial models. Mathematically, this is a consequence of the flow-aligning term diverging as the scalar order parameter, which represents the degree of elongation, approaches zero. This result is in contradiction with our expectation that more round particles should respond less strongly with the strain, bringing into question its physical significance. Therefore, while some progress has been made towards a more complete description of the shape dynamics, there are questions that are yet to be answered.

Can intercellular effects be incorporated directly into our model of deformable nematics?

A key characteristic of cellular models such as vertex and phase field models is the ability of cells to exchange neighbours through intercalations, or T1 transitions [122, 158, 159]. Simulations of the phase field model subjected to a shear flow, display oscillatory dynamics of both the shape and orientation of particles due to a series of periodic T1 transitions. These are a direct consequence of (repulsive) inter-particle interactions.

Motivated by these results, a currently ongoing project involves attempting to incorporate the process associated with T1 transitions into our model of deformable nematics by considering the ingredients required to match the qualitative dynamics seen in simulations. While results are preliminary and not included as part of this thesis, we have found that a coarse grained model of T1 transitions as an effective strain rate [160, 161] can lead to qualitatively, and perhaps quantitatively similar results between our continuum model of deformable particles and simulations of the phase field model. In turn, these results would allow us to create a phenomenological framework that reconciles models that resolve cell shape directly, and continuum level models.

Appendices

A

The hybrid Lattice-Boltzmann method

In this thesis we numerically solved the Navier-Stokes equations 2.11 and 2.12 for the flow field using a Lattice-Boltzmann (LB) algorithm. The equations of motion of all other fields are solved using a finite difference method. This approach has been coined [63, 162] as the hybrid Lattice-Boltzmann method.

A.1 From Navier Stokes to Lattice Boltzmann

The (LB) method utilises particle-based methods to numerically solve the Navier-Stokes equations. Instead of solving the equations of motion directly, this method instead solves a discretised version of the Boltzmann equation. The Boltzmann equation describes how momentum distributions of particles $f_{\boldsymbol{k}}(\boldsymbol{r})$ evolve over time due to advection and collisions with other particles. Here, $f_{\boldsymbol{k}}(\boldsymbol{r})$ represents the number of particles of momentum $\boldsymbol{k}$ at location $\boldsymbol{r}$. The Navier-Stokes equations arise as a special case of the Boltzmann equation under the following assumptions:

1. The distribution function is close to a local equilibrium function $f^0_{\boldsymbol{k}}$. Thus,

$$f_{\boldsymbol{k}}(\boldsymbol{r}) = f^0_{\boldsymbol{k}} + \delta f^1_{\boldsymbol{k}}(\boldsymbol{r}) \tag{A.1}$$

2. The collision term relaxes the distributions to the equilibrium function over a relaxation time τ. Thus,

$$\mathcal{I}_{\boldsymbol{k}}[\{f_{\boldsymbol{i}}\}] = -\frac{f_{\boldsymbol{k}}(\boldsymbol{r}) - f_{\boldsymbol{k}}^0}{\tau} \tag{A.2}$$

By using the Chapman-Enskog expansion [163], these two assumptions yield the Navier-Stokes equations. The LB method is computationally efficient, easily parallelised, and is accurate to second order for the weakly-compressible Navier-Stokes equation [62].

A.2 The Lattice-Boltzmann equation

In the LB algorithm, the distribution function $f_{\boldsymbol{k}}(\boldsymbol{r})$ is defined over discrete lattice sites $\boldsymbol{r}$ with spacing Δx . Moreover, momentum space is discretised into a fixed set of direction vectors $\boldsymbol{e}_i$, where index i labels specific lattice direction. In 3D, we use the 'D3Q15' velocity vector set. Each direction also has an associated weight, w_i. Thus, we arrive at the distribution function $f_i(\boldsymbol{x}, t)$, describing the number of particles at lattice site x at time t moving with velocity $\mathbf{e}_i$.

The fluid density ρ is related to the distribution function by

$$\rho(\mathbf{x}, t) = \sum_i f_i(\mathbf{x}, t) \,, \tag{A.3}$$

and the fluid momentum is given by

$$\rho\mathbf{u} = \sum_i f_i \mathbf{e}_i \,, \tag{A.4}$$

where $\mathbf{u}$ is the flow field.

The time evolution of the distribution function $f_i(\mathbf{x}, t)$ has two steps:

1. Collision step: Update the local distribution functions due to collisions

$$\tilde{f}_i(\mathbf{x}, t) = f_i(\mathbf{x}, t) + \Delta t \, C_f(\mathbf{x}, t) \,. \tag{A.5}$$

2. Streaming step: Move each particle to the next lattice site in the direction of motion

$$f_i(\mathbf{x} + \mathbf{e}_i \Delta t, t + \Delta t) = \tilde{f}_i(\mathbf{x}, t) \,. \tag{A.6}$$

In Eq.(A.5), C_f is a collision operator which captures the local relaxation to equilibrium, but also contains an additional source term $S_i(\mathbf{x}, t)$ to model body forces,

$$C_f(\mathbf{x}, t) = -\frac{1}{\tau}\left(f_i - f_i^0\right) + S_i(\mathbf{x}, t)\,. \tag{A.7}$$

Different forms of collision operators and schemes to model bofy fources as source terms exist. Here, we have used the Bhatnagar-Gross-Krook (BGK) collision operator (Eq. A.7), and a Guo forcing scheme [164]. Moreover, the equilibrium distributions f_i^0 must satisfy

$$\sum_i f_i^0 = \rho, \quad \sum_i \mathbf{e}_i f_i^0 = \rho\mathbf{u}, \quad \sum_i \mathbf{e}_i \mathbf{e}_i f_i^0 = -\boldsymbol{\sigma} + \rho\mathbf{u}\mathbf{u}\,, \tag{A.8}$$

where $\boldsymbol{\sigma}$ describes the symmetric terms of the stress tensor in thermodynamic equilibrium. We use the equilibrium function

$$f_i^0 = w_i \rho \left(1 + \frac{\mathbf{u}\cdot\mathbf{c}_i}{c_s^2} + \frac{(\mathbf{u}\cdot\mathbf{c}_i)^2}{c_s^4} - \frac{\mathbf{u}\cdot\mathbf{u}}{2c_s^2}\right) \tag{A.9}$$

where w_i are the ‘D3Q15’ weights and c_s is the speed of sound in LB units [62].

A.2.1 Boundary Conditions

Rigid walls with no-slip boundary conditions are treated in Lattice-Boltzmann by adding an additional layer of ghost nodes inside the boundary, where we are free to tune the distribution functions f_i. By carefully choosing these functions, the velocity field at a virtual boundary node in between the last fluid node and the ghost node can be controlled as desired. We implemented this method, called the bounce-back method, to study no-slip boundary conditions for the velocity field at walls. We refer the reader to Chapter 5 in [62] for a more detailed explanation of this method.

B

Channel flows of deformable nematics

In this appendix, we provide more mathematical and numerical detail on the assumptions and results of Chapter 2.

B.1 Particle dynamics in Poiseuille flow

B.1.1 Complete expressions for molecular potential arising from the functional derivatives of the free energy

In Chapter 3.4.1, only a minimal formulation arising from the free energy is retained in the expression for the to keep the analysis tractable. In this section, we present the full functional derivatives that contribute to Eqs. (3.20) and (3.21). These read as:

$$\delta\mathcal{F}/\delta r = A_r(r-r_0) + A_r^*(r-r_0)^3 + \frac{K'(r)}{2}(\partial_{y'}\theta)^2, \tag{B.1}$$

$$\delta\mathcal{F}/\delta\theta = -K(r)\partial_{y'}^2\theta - K'(r)(\partial_{y'}r)(\partial_{y'}\theta), \tag{B.2}$$

where $K'(r) \equiv \partial K(r)/\partial r$. In Chapter 3.4.1, the last terms in Eqs. B.1 - B.2 are omitted for simplicity. Including these terms does not change the results qualitatively. Fig. B.1 shows kymographs of $r(y',t')$ and $\theta(y',t')$ for $\alpha_p = 1.8, \beta = 0.05$ in a Poiseuille flow, with the additional terms included. Neumann boundary conditions are applied to both r and θ on the channel walls. These figures are to be compared with Fig. 3.13. The complex spatio-temporal dynamics predicted, namely the

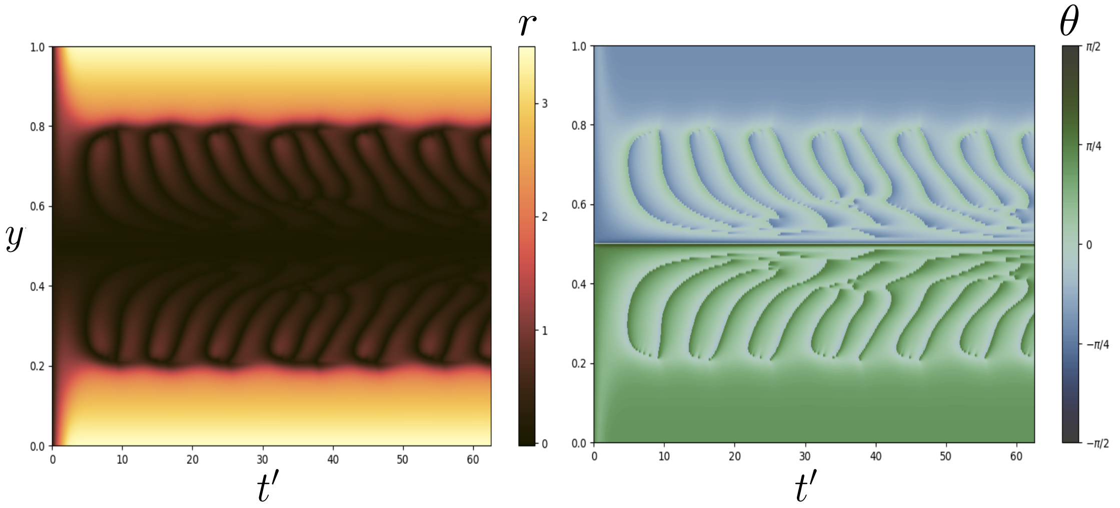

(a) (b)

Figure B.1: Kymographs of (a) $r(y', t')$ and (b) $\theta(y', t')$ of deformable nematics in a Poiseuille flow incorporating all terms described by Eq. B.1-B.2 into Eq. 5-6. Simulations are for $\alpha_p = 1.8, \beta = 0.05$.

wall-bound band of more elongated particles and the central band consisting of less elongated particles exhibiting patterns, are visible in both cases.

Bibliography

1. Hadjifrangiskou, I., Ruske, L. J. & Yeomans, J. M. Active nematics with deformable particles. *Soft Matter* **19,** 6664–6670 (2023).
2. Hadjifrangiskou, I., Thampi, S. P. & Valani, R. N. Nematic order from phase synchronization of shape oscillations. *Phys. Rev. Lett.* **135,** 068101 (Sept. 2025).
3. Hadjifrangiskou, I., Thampi, S. P. & Yeomans, J. M. Channel Flows of Deformable Nematics. *Phys. Rev. Lett.* **135,** 118202 (11 Sept. 2025).
4. Manning, M. L. Essay: Collections of deformable particles present exciting challenges for soft matter and biological physics. *Phys. Rev. Lett.* **130,** 130002 (2023).
5. Bagchi, P. & Kalluri, R. M. Dynamics of nonspherical capsules in shear flow. *Phys. Rev. E* **80,** 016307 (2009).
6. Mader, M. A., Vitkova, V., Abkarian, M., Viallat, A. & Podgorski, T. Dynamics of viscous vesicles in shear flow. *Eur. Phys. J. E* **19,** 389–397 (2006).
7. Beaucourt, J., Rioual, F., Séon, T., Biben, T. & Misbah, C. Steady to unsteady dynamics of a vesicle in a flow. *Phys. Rev. E* **69,** 011906 (2004).
8. Angelini, T. E. *et al.* Glass-like dynamics of collective cell migration. *Proc. Natl. Acad. Sci.*. **108,** 4714–4719 (2011).
9. Angelini, T. E., Hannezo, E., Trepat, X., Fredberg, J. J. & Weitz, D. A. Cell migration driven by cooperative substrate deformation patterns. *Phys. Rev. Lett.* **104,** 168104 (2010).
10. Lecuit, T. & Lenne, P.-F. Cell surface mechanics and the control of cell shape, tissue patterns and morphogenesis. *Nat. Rev. Mol. Cell Biol.* **8,** 633–644 (2007).
11. Heisenberg, C.-P. & Bellaiche, Y. Forces in tissue morphogenesis and patterning. *Cell* **153,** 948–962 (2013).
12. Merkel, M. & Manning, M. L. *Using cell deformation and motion to predict forces and collective behavior in morphogenesis* in *Semin. Cell. Dev. Bio.* **67** (2017), 161–169.
13. Blanchard, G. B. *et al.* Tissue tectonics: morphogenetic strain rates, cell shape change and intercalation. *Nat. Methods* **6,** 458–464 (2009).
14. Butler, L. C. *et al.* Cell shape changes indicate a role for extrinsic tensile forces in Drosophila germ-band extension. *Nat. Cell. Bio.* **11,** 859–864 (2009).
15. Van Engeland, N. C. *et al.* A biomimetic microfluidic model to study signalling between endothelial and vascular smooth muscle cells under hemodynamic conditions. *Lab Chip* **18,** 1607–1620 (2018).

16. Boularaoui, S., Al Hussein, G., Khan, K. A., Christoforou, N. & Stefanini, C. An overview of extrusion-based bioprinting with a focus on induced shear stress and its effect on cell viability. *Bioprinting* **20,** e00093 (2020).
17. Lee, J., Ishihara, A. & Jacobson, K. How do cells move along surfaces? *Trends Cell Biol.* **3,** 366–370 (1993).
18. Lazarides, E. & Revel, J. P. The molecular basis of cell movement. *Sci. Am.* **240,** 100–113 (1979).
19. Marchetti, M. C. *et al.* Hydrodynamics of soft active matter. *Rev. Mod. Phys.* **85,** 1143 (2013).
20. Doostmohammadi, A., Ignés-Mullol, J., Yeomans, J. M. & Sagués, F. Active nematics. *Nat. Commun.* **9,** 3246 (2018).
21. Jülicher, F., Grill, S. W. & Salbreux, G. Hydrodynamic theory of active matter. *Rep. Prog. Phys.* **81,** 076601 (2018).
22. Duclos, G., Erlenkamper, C., Joanny, J.-F. & Silberzan, P. Topological defects in confined populations of spindle-shaped cells. *Nat. Phys.* **13,** 58–62 (Jan. 2017).
23. Voituriez, R., Joanny, J.-F. & Prost, J. Spontaneous flow transition in active polar gels. *Europhys. Lett.* **70,** 404 (2005).
24. Saw, T. B. *et al.* Topological defects in epithelia govern cell death and extrusion. *Nature* **544,** 212–216 (Apr. 2017).
25. Wang, Z., Marchetti, M. C. & Brauns, F. Patterning of morphogenetic anisotropy fields. *Proc. Natl. Acad. Sci..* **120,** e2220167120 (2023).
26. Simha, R. A. & Ramaswamy, S. Hydrodynamic fluctuations and instabilities in ordered suspensions of self-propelled particles. *Phys. Rev. Lett.* **89,** 058101 (2002).
27. Santhosh, S., Nejad, M. R., Doostmohammadi, A., Yeomans, J. M. & Thampi, S. P. Activity induced nematic order in isotropic liquid crystals. *J. Stat. Phys.* **180,** 699–709 (2020).
28. Larsen, S. H., Adler, J., Gargus, J. J. & Hogg, R. W. Chemomechanical coupling without ATP: the source of energy for motility and chemotaxis in bacteria. *Proc. Natl. Acad. Sci.* **71,** 1239–1243 (1974).
29. Howse, J. R. *et al.* Self-motile colloidal particles: from directed propulsion to random walk. *Phys. Rev. Lett.* **99,** 048102 (2007).
30. Ladoux, B. & Mège, R.-M. Mechanobiology of collective cell behaviours. *Nat. Rev. Mol. Cell Biol.* **18,** 743–757 (2017).
31. Schoetz, E.-M., Lanio, M., Talbot, J. A. & Manning, M. L. Glassy dynamics in three-dimensional embryonic tissues. *J. R. Soc. Interface* **10,** 20130726 (2013).
32. Giavazzi, F. *et al.* Flocking transitions in confluent tissues. *Soft Matter* **14,** 3471–3477 (2018).
33. Alert, R., Casademunt, J. & Joanny, J.-F. Active turbulence. *Annu. Rev. Condens. Matter Phys.* **13,** 143–170 (2022).
34. Alert, R., Joanny, J.-F. & Casademunt, J. Universal scaling of active nematic turbulence. *Nat. Phys.* **16,** 682–688 (2020).

35. Ranft, J. *et al.* Fluidization of tissues by cell division and apoptosis. *Proc. Natl. Acad. Sci.* **107,** 20863–20868 (2010).

36. Blanch-Mercader, C. & Casademunt, J. Hydrodynamic instabilities, waves and turbulence in spreading epithelia. *Soft Matter* **13,** 6913–6928 (2017).

37. Blanch-Mercader, C. *et al.* Turbulent dynamics of epithelial cell cultures. *Phys. Rev. Lett.* **120,** 208101 (2018).

38. Saw, T. B., Xi, W., Ladoux, B. & Lim, C. T. Biological tissues as active nematic liquid crystals. *Adv. Mater.* **30,** 1802579 (2018).

39. Yaman, Y. I., Demir, E., Vetter, R. & Kocabas, A. Emergence of active nematics in chaining bacterial biofilms. *Nat. Commun.* **10,** 2285 (2019).

40. Pearce, P. *et al.* Flow-induced symmetry breaking in growing bacterial biofilms. *Phys. Rev. Lett.* **123,** 258101 (2019).

41. Duclos, G., Erlenkämper, C., Joanny, J.-F. & Silberzan, P. Topological defects in confined populations of spindle-shaped cells. *Nat. Phys.* **13,** 58–62 (2017).

42. Pearce, D., Nambisan, J., Ellis, P., Fernandez-Nieves, A. & Giomi, L. Orientational correlations in active and passive nematic defects. *Phys. Rev. Lett.* **127,** 197801 (2021).

43. Saw, T. B. *et al.* Topological defects in epithelia govern cell death and extrusion. *Nature* **544,** 212–216 (2017).

44. Copenhagen, K., Alert, R., Wingreen, N. S. & Shaevitz, J. W. Topological defects promote layer formation in Myxococcus xanthus colonies. *Nat. Phys.* **17,** 211–215 (2021).

45. Ardaševa, A. & Doostmohammadi, A. Topological defects in biological matter. *Nat. Rev. Phys.* **4,** 354–356 (2022).

46. Mueller, R., Yeomans, J. M. & Doostmohammadi, A. Emergence of active nematic behavior in monolayers of isotropic cells. *Phys. Rev. Lett.* **122,** 048004 (2019).

47. Thampi, S. P. & Yeomans, J. M. Active turbulence in active nematics. *Eur. Phys. J. ST* **225,** 651–662 (2016).

48. Doostmohammadi, A., Thampi, S. P. & Yeomans, J. M. Defect-mediated morphologies in growing cell colonies. *Phys. Rev. Lett.* **117,** 048102 (2016).

49. DeCamp, S. J., Redner, G. S., Baskaran, A., Hagan, M. F. & Dogic, Z. Orientational order of motile defects in active nematics. *Nat. Mat.* **14,** 1110–1115 (2015).

50. Martínez-Prat, B., Ignés-Mullol, J., Casademunt, J. & Sagués, F. Selection mechanism at the onset of active turbulence. *Nature physics* **15,** 362–366 (2019).

51. De Gennes, P.-G. & Prost, J. *The Physics of Liquid Crystals* (Oxford University Press, 1993).

52. Onsager, L. The effects of shape on the interaction of colloidal particles. *Ann. N. Y. Acad. Sci.* **51,** 627–659 (1949).

53. Mermin, N. D. & Wagner, H. Absence of ferromagnetism or antiferromagnetism in one-or two-dimensional isotropic Heisenberg models. *Phys. Rev. Lett.* **17,** 1133 (1966).

54. Frenkel, D. & Eppenga, R. Evidence for algebraic order in a two-dimensional hard-core nematic. *Phys. Rev. A* **31,** 1776–1787 (1985).

55. Beris, A. N. & Edwards, B. J. *Thermodynamics of flowing systems: with internal microstructure* **36** (Oxford University Press on Demand, 1994).

56. Vink, R. L. Crossover from a Kosterlitz-Thouless phase transition to a discontinuous phase transition in two-dimensional liquid crystals. *Phys. Rev. E* **90,** 062132 (2014).

57. Vafa, F., Bowick, M. J., Shraiman, B. I. & Marchetti, M. C. Fluctuations can induce local nematic order and extensile stress in monolayers of motile cells. *Soft Matter* **17,** 3068–3073 (2021).

58. Frank, F. C. I. Liquid crystals. On the theory of liquid crystals. *Faraday Discuss.* **25,** 19–28 (1958).

59. Zhang, R., Kumar, N., Ross, J. L., Gardel, M. L. & De Pablo, J. J. Interplay of structure, elasticity, and dynamics in actin-based nematic materials. *Proc. Natl. Acad. Sci.* **115,** E124–E133 (2018).

60. Toulouse, G. & Kléman, M. Principles of a classification of defects in ordered media. *J. Phys. (Paris), Lett.* **37,** 149–151 (1976).

61. Mermin, N. D. The topological theory of defects in ordered media. *Red. Mod. Phys.* **51,** 591 (1979).

62. Krueger, T. *et al. The Lattice Boltzmann Method: Principles and Practice* (Springer, 2016).

63. Marenduzzo, D., Orlandini, E., Cates, M. & Yeomans, J. Steady-state hydrodynamic instabilities of active liquid crystals: Hybrid lattice Boltzmann simulations. *Phys. Rev. E* **76,** 031921 (2007).

64. Bischofs, I. B. & Schwarz, U. S. Cell organization in soft media due to active mechanosensing. *Proc. Natl. Acad. Sci.* **100,** 9274–9279 (2003).

65. Kurpinski, K., Chu, J., Hashi, C. & Li, S. Anisotropic mechanosensing by mesenchymal stem cells. *Proc. Natl. Acad. Sci.* **103,** 16095–16100 (2006).

66. Giomi, L., Bowick, M. J., Mishra, P., Sknepnek, R. & Cristina Marchetti, M. Defect dynamics in active nematics. *Philos. Trans. R. Soc. A* **372,** 20130365 (2014).

67. Vafa, F., Bowick, M. J., Marchetti, M. C. & Shraiman, B. I. *Multi-defect Dynamics in Active Nematics* 2020. arXiv: `2007.02947 [cond-mat.soft]`.

68. Maroudas-Sacks, Y. *et al.* Topological defects in the nematic order of actin fibers as organization centers of Hydra morphogenesis. *bioRxiv* (2020).

69. Vafa, F. & Mahadevan, L. Active Nematic Defects and Epithelial Morphogenesis. *Phys. Rev. Lett.* **129,** 098102 (9 Aug. 2022).

70. Frank, J. R. & Kardar, M. Defects in nematic membranes can buckle into pseudospheres. *Phys. Rev. E* **77,** 041705 (4 Apr. 2008).

71. Thampi, S. P., Golestanian, R. & Yeomans, J. M. Vorticity, defects and correlations in active turbulence. *Philos. Trans. R. Soc. A* **372,** 20130366 (2014).

72. Ramaswamy, S. & Rao, M. Active-filament hydrodynamics: instabilities, boundary conditions and rheology. *New J. Phys.* **9,** 423–423 (Nov. 2007).
73. Hemingway, E. J., Mishra, P., Marchetti, M. C. & Fielding, S. M. Correlation lengths in hydrodynamic models of active nematics. *Soft Matter* **12,** 7943–7952 (2016).
74. Marenduzzo, D., Orlandini, E. & Yeomans, J. M. Hydrodynamics and Rheology of Active Liquid Crystals: A Numerical Investigation. *Phys. Rev. Lett.* **98,** 118102 (11 Mar. 2007).
75. Dubois, F., Lallemand, P., Obrecht, C. & Mahdi Tekitek, M. Lattice Boltzmann model approximated with finite difference expressions. *Comput. Fluids* **155.** ICMMES2015, 3–8 (2017).
76. Li, Z., Qiao, Z. & Tang, T. *Numerical solution of differential equations: introduction to finite difference and finite element methods* (Cambridge University Press, 2017).
77. Orszag, S. A. Numerical methods for the simulation of turbulence. *Phys. Fluids* **12,** II–250 (1969).
78. Kusumaatmaja, H. & Yeomans, J. M. in *Simulating Complex Systems by Cellular Automata* 241–274 (Springer, 2010).
79. Tarama, M., Itino, Y., Menzel, A. & Ohta, T. Individual and collective dynamics of self-propelled soft particles. *Eur. Phys. J-Spec. Top.* **223,** 121–139 (2014).
80. Hernandez, A. & Marchetti, M. C. Poisson-bracket formulation of the dynamics of fluids of deformable particles. *Phys. Rev. E* **103,** 032612 (3 Mar. 2021).
81. Czajkowski, M., Bi, D., Manning, M. L. & Marchetti, M. C. Hydrodynamics of shape-driven rigidity transitions in motile tissues. *Soft Matter* **14,** 5628–5642 (2018).
82. Boromand, A., Signoriello, A., Ye, F., O'Hern, C. S. & Shattuck, M. D. Jamming of deformable polygons. *Phys. Rev. Lett.* **121,** 248003 (2018).
83. Wang, D. *et al.* The structural, vibrational, and mechanical properties of jammed packings of deformable particles in three dimensions. *Soft Matter* **17,** 9901–9915 (2021).
84. Kim, S., Pochitaloff, M., Stooke-Vaughan, G. A. & Campàs, O. Embryonic tissues as active foams. *Nat. Phys.* **17,** 859–866 (2021).
85. Tarama, M. Dynamics of deformable active particles under external flow field. *J. Phys. Soc. Jpn.* **86,** 101011 (2017).
86. Tanjeem, N., Minnis, M. B., Hayward, R. C. & Shields IV, C. W. Shape-Changing Particles: From Materials Design and Mechanisms to Implementation. *Adv. Mat.* **34,** 2105758 (2022).
87. Ahmmed, S. M. *et al.* Multi-sample deformability cytometry of cancer cells. *APL Bioeng.* **2,** 032002 (2018).
88. Suresh, S. Biomechanics and biophysics of cancer cells. *Acta Biomater.* **3,** 413–438 (2007).

89. Wirtz, D., Konstantopoulos, K. & Searson, P. C. The physics of cancer: the role of physical interactions and mechanical forces in metastasis. *Nat. Rev. Cancer* **11,** 512–522 (2011).

90. Comba, A. *et al.* Spatiotemporal analysis of glioma heterogeneity reveals COL1A1 as an actionable target to disrupt tumor progression. *Nat. Commun.* **13,** 3606 (2022).

91. Larson, R. G. The structure and rheology of complex fluids. *(No Title)* (1999).

92. Bilby, B. A. & Kolbuszewski, M. The finite deformation of an inhomogeneity in two-dimensional slow viscous incompressible flow. *P. Roy. Soc. Lond. A Mat.* **355,** 335–353 (1977).

93. Gao, T., Hu, H. H. & Castañeda, P. P. Rheology of a suspension of elastic particles in a viscous shear flow. *J. Fluid Mech.* **687,** 209–237 (2011).

94. Gao, T., Hu, H. H. & Castañeda, P. P. Dynamics and rheology of elastic particles in an extensional flow. *J. Fluid Mech.* **715,** 573–596 (2013).

95. Kuzuu, N. & Doi, M. Constitutive equation for nematic liquid crystals under weak velocity gradient derived from a molecular kinetic equation. *J. Phys. Soc. Jpn.* **52,** 3486–3494 (1983).

96. Ternet, D. J., Larson, R. G. & Leal, L. G. Flow-aligning and tumbling in small-molecule liquid crystals: pure components and mixtures. *Rheologica Acta* **38,** 183–197 (1999).

97. Cohen, I. M. & Kundu, P. K. *Fluid Mechanics* (Elsevier, 2004).

98. Batchelor, G. K. *An introduction to fluid dynamics* (Cambridge university press, 2000).

99. Koch, D. *et al.* Ghost channels and ghost cycles guiding long transients in dynamical systems. *Phys. Rev. Lett.* **133,** 047202 (2024).

100. Tjipto-Margo, B., Evans, G. T., Allen, M. P. & Frenkel, D. Elastic constants of hard and soft nematic liquid crystals. *J. Phys. Chem.-US* **96,** 3942–3948 (1992).

101. Chono, S., Tsuji, T. & Denn, M. M. Spatial development of director orientation of tumbling nematic liquid crystals in pressure-driven channel flow. *J. Non-Newton. Fluids* **79,** 515–527 (1998).

102. Thampi, S. P., Golestanian, R. & Yeomans, J. M. Driven active and passive nematics. *Mol. Phys.* **113,** 2656–2665 (2015).

103. Dell'Arciprete, D. *et al.* A growing bacterial colony in two dimensions as an active nematic. *Nat. Commun.* **9,** 1–9 (2018).

104. Vlassopoulos, D. & Cloitre, M. Tunable rheology of dense soft deformable colloids. *Curr. Opin. Colloid Interface Sci.* **19,** 561–574 (2014).

105. Balasubramaniam, L. *et al.* Investigating the nature of active forces in tissues reveals how contractile cells can form extensile monolayers. *Nature materials* **20,** 1156–1166 (2021).

106. Giomi, L. Geometry and topology of turbulence in active nematics. *Phys. Rev. X* **5,** 031003 (2015).

107. Blow, M. L., Thampi, S. P. & Yeomans, J. M. Biphasic, lyotropic, active nematics. *Phys. Rev. Lett.* **113,** 248303 (2014).

108. Vromans, A. J. & Giomi, L. Orientational properties of nematic disclinations. *Soft Matter* **12,** 6490–6495 (2016).

109. Li, X. *et al.* On the mechanism of long-range orientational order of fibroblasts. *Proc. Natl. Acad. Sci.* **114,** 8974–8979 (2017).

110. Ron, J. E. *et al.* Polarization and motility of one-dimensional multi-cellular trains. *bioRxiv,* 547405 (2023).

111. Fletcher, A. G., Osterfield, M., Baker, R. E. & Shvartsman, S. Y. Vertex models of epithelial morphogenesis. *Biophys. J.* **106,** 2291–2304 (2014).

112. Alt, S., Ganguly, P. & Salbreux, G. Vertex models: from cell mechanics to tissue morphogenesis. *Philos. Trans. R. Soc. B* **372,** 20150520 (2017).

113. Bi, D., Yang, X., Marchetti, M. C. & Manning, M. L. Motility-driven glass and jamming transitions in biological tissues. *Phys. Rev. X* **6,** 021011 (2016).

114. Barton, D. L., Henkes, S., Weijer, C. J. & Sknepnek, R. Active vertex model for cell-resolution description of epithelial tissue mechanics. *PLOS Comput. Biol.* **13,** e1005569 (2017).

115. Merkel, M. & Manning, M. L. A geometrically controlled rigidity transition in a model for confluent 3D tissues. *New J. Phys.* **20,** 022002 (2018).

116. Rozman, J., Yeomans, J. M. & Sknepnek, R. Shape-Tension Coupling Produces Nematic Order in an Epithelium Vertex Model. *Phys. Rev. Lett.* **131,** 228301 (22 Nov. 2023).

117. Duclut, C., Paijmans, J., Inamdar, M. M., Modes, C. D. & Jülicher, F. Active T1 transitions in cellular networks. *The European Physical Journal E* **45,** 29 (2022).

118. Rozman, J., Chaithanya, K., Yeomans, J. M. & Sknepnek, R. Vertex model with internal dissipation enables sustained flows. en. *Nat. Commun.* **16,** 530 (Jan. 2025).

119. Zhang, G. & Yeomans, J. M. Active forces in confluent cell monolayers. *Phys. Rev. Lett.* **130,** 038202 (2023).

120. Zhang, G., Mueller, R., Doostmohammadi, A. & Yeomans, J. M. Active inter-cellular forces in collective cell motility. *J. R. Soc. Interface* **17,** 20200312 (2020).

121. Graham, J. N., Zhang, G. & Yeomans, J. M. Cell sorting by active forces in a phase-field model of cell monolayers. *Soft Matter* **20,** 2955–2960 (13 2024).

122. Pinto, D. E. P., Rozman, J. & Yeomans, J. M. *Spontaneous Hole Formation in Cell Monolayers Emerges from Collective Cell Motion* 2025. arXiv: `2508.06461 [cond-mat.soft]`.

123. Sadhukhan, S. & Nandi, S. On the origin of universal cell shape variability in a confluent epithelial monolayer. *Elife* **11,** e76406 (2022).

124. Maier, W. & Saupe, A. Eine einfache molekulare Theorie des nematischen kristallinflüssigen Zustandes. *Zeitschrift für Naturforschung A* **13,** 564–566 (1958).

125. Stephen, M. J. & Straley, J. P. Physics of liquid crystals. *Red. Mod. Phys.* **46,** 617 (1974).

126. Lelidis, I. & Durand, G. Electric-field-induced isotropic-nematic phase transition. *Phys. Rev. E* **48,** 3822 (1993).

127. Olmsted, P. D. & Goldbart, P. Theory of the nonequilibrium phase transition for nematic liquid crystals under shear flow. *Phys. Rev. A* **41,** 4578 (1990).

128. Ostapenko, T., Wiant, D., Sprunt, S. N., Jákli, A. & Gleeson, J. T. Magnetic-field induced isotropic to nematic liquid crystal phase transition. *Phys. Rev. Lett.* **101,** 247801 (2008).

129. Pearce, D. Activity driven orientational order in active nematic liquid crystals on an anisotropic substrate. *Phys. Rev. Lett.* **122,** 227801 (2019).

130. Barrat, J.-L. *et al.* Soft matter roadmap. *J. Phys. Mat.* **7,** 012501 (2023).

131. Kuramoto, Y. *Self-entrainment of a population of coupled non-linear oscillators* in *International Symposium on Mathematical Problems in Theoretical Physics: January 23–29, 1975, Kyoto University, Kyoto/Japan* (1975), 420–422.

132. Pikovsky, A., Rosenblum, M. & Kurths, J. Phase synchronization in regular and chaotic systems. *Int. J. Bifurc. Chaos Appl. Sci. Eng.* **10,** 2291–2305 (2000).

133. Pikovsky, A., Rosenblum, M. & Kurths, J. *Synchronization: A Universal Concept in Nonlinear Sciences* (Cambridge University Press, 2001).

134. Buck, J. Synchronous rhythmic flashing of fireflies. II. *Q. Rev. Biol.* **63,** 265–289 (1988).

135. Rosenblum, M. & Pikovsky, A. Synchronization: from pendulum clocks to chaotic lasers and chemical oscillators. *Contemp. Phys.* **44,** 401–416 (2003).

136. Davis, P. K., Ho, A. & Dowdy, S. F. Biological methods for cell-cycle synchronization of mammalian cells. *Biotechniques* **30,** 1322–1331 (2001).

137. Uchida, N., Golestanian, R. & Bennett, R. R. Synchronization and collective dynamics of flagella and cilia as hydrodynamically coupled oscillators. *Journal of the Physical Society of Japan* **86,** 101007 (2017).

138. Golestanian, R., Yeomans, J. M. & Uchida, N. Hydrodynamic synchronization at low Reynolds number. *Soft Matter* **7,** 3074–3082 (7 2011).

139. Heinrich, G., Ludwig, M., Qian, J., Kubala, B. & Marquardt, F. Collective Dynamics in Optomechanical Arrays. *Phys. Rev. Lett.* **107,** 043603 (4 July 2011).

140. Holmes, C. A., Meaney, C. P. & Milburn, G. J. Synchronization of many nanomechanical resonators coupled via a common cavity field. *Phys. Rev. E* **85,** 066203 (6 June 2012).

141. Fredrickson-Hemsing, L., Ji, S., Bruinsma, R. & Bozovic, D. Mode-locking dynamics of hair cells of the inner ear. *Phys. Rev. E* **86,** 021915 (2 Aug. 2012).

142. Levy, M. *et al.* High-order synchronization of hair cell bundles. *Sci. Rep.* **6,** 39116 (Dec. 2016).

143. Likharev, K. K. *Dynamics of Josephson junctions and circuits* (CRC Press, London, England, Feb. 2022).

144. Gandhi, P., Knobloch, E. & Beaume, C. Dynamics of phase slips in systems with time-periodic modulation. *Phys. Rev. E* **92,** 062914 (6 Dec. 2015).
145. Juniper, M. P., Straube, A. V., Besseling, R., Aarts, D. G. & Dullens, R. P. Microscopic dynamics of synchronization in driven colloids. *Nat. Commun.* **6,** 7187 (May 2015).
146. Juniper, M. P. N. *et al.* Dynamic mode locking in a driven colloidal system: experiments and theory. *New J. Phys.* **19,** 013010 (Jan. 2017).
147. Jackson, E. A. in *Perspectives of Nonlinear Dynamics* 142–225 (Cambridge University Press, 1989).
148. Jeffery, G. B. The motion of ellipsoidal particles immersed in a viscous fluid. *Proc. R. Soc. Lond. A* **102,** 161–179 (1922).
149. Ma, R., Klindt, G. S., Riedel-Kruse, I. H., Jülicher, F. & Friedrich, B. M. Active Phase and Amplitude Fluctuations of Flagellar Beating. *Phys. Rev. Lett.* **113,** 048101 (4 July 2014).
150. Taloni, A. *et al.* Volume Changes During Active Shape Fluctuations in Cells. *Phys. Rev. Lett.* **114,** 208101 (20 May 2015).
151. Piñeros, W. D. & Fodor, É. Biased Ensembles of Pulsating Active Matter. *Phys. Rev. Lett.* **134,** 038301 (3 Jan. 2025).
152. Rizvi, M. S. *et al.* Rheological signature of microswimmer phase-locking under flow. *Phys. Rev. Fluids* **4,** 103302 (10 Oct. 2019).
153. Strogatz, S. H. *Nonlinear dynamics and Chaos* 2nd ed. (Westview Press, 2015).
154. An, L., Ji, F., Zhao, E., Liu, Y. & Liu, Y. Measuring cell deformation by microfluidics. *Front. Bioeng. Biotech.* **11,** 1214544 (2023).
155. Dahl, J. B., Lin, J.-M. G., Muller, S. J. & Kumar, S. Microfluidic strategies for understanding the mechanics of cells and cell-mimetic systems. *Annu. Rev. Chem. Biomol. Eng.* **6,** 293–317 (2015).
156. McWhirter, J. L., Noguchi, H. & Gompper, G. Flow-induced clustering and alignment of vesicles and red blood cells in microcapillaries. *Proc. Natl. Acad. Sci.* **106,** 6039–6043 (2009).
157. Nejad, M. R., Yeomans, J. M. & Thampi, S. P. *Cellular dynamics emerging from turbulent flows steered by active filaments* 2025. arXiv: `2501.05971 [cond-mat.soft]`.
158. Rozman, J., Krajnc, M. & Ziherl, P. Collective cell mechanics of epithelial shells with organoid-like morphologies. *Nat. Commun.* **11,** 1–9 (2020).
159. Jain, H. P., Voigt, A. & Angheluta, L. Robust statistical properties of T1 transitions in a multi-phase field model of cell monolayers. *Sci. Rep.* **13,** 10096 (2023).
160. Tlili, S. *et al.* Colloquium: Mechanical formalisms for tissue dynamics. *The European Physical Journal E* **38,** 33 (2015).
161. Puggioni, L., Krommydas, D. & Giomi, L. *Collective migration and topological phase transitions in confluent epithelia* 2025. arXiv: `2502.09554 [cond-mat.soft]`.

162. Thampi, S. P., Golestanian, R. & Yeomans, J. M. Vorticity, defects and correlations in active turbulence. *Philos. Trans. R. Soc. A* **372,** 20130366 (2014).

163. Chapman, S. & Cowling, T. G. *The mathematical theory of non-uniform gases: an account of the kinetic theory of viscosity, thermal conduction and diffusion in gases* (Cambridge University Press, 1990).

164. Guo, Z., Zheng, C. & Shi, B. Discrete lattice effects on the forcing term in the lattice Boltzmann method. *Phys. Rev. E* **65,** 046308 (Apr. 2002).